Electromagnetic Propagation in Tunnels

Author:
Benjamín Izquierdo

Thesis Advisor:
Jordi Romeu Robert

AntennaLab
Universitat Politècnica de Catalunya
Departament de Teoria del Senyal i Comunicacions

Tesis presentada per obtenir el títol de Doctor
per la Universitat Politècnica de Catalunya

May 2, 2011

a Benjamín, mi padre

un buen hombre

a totes les Maries

Acknowledgements

Voldria començar agraint el meu tutor, el Jordi Romeu, l'ajut dispensat durant tota l'elaboració d'aquesta tesi doctoral. En moments difícils o quan no hi veia sortida, els seus ànims i consells han permès tirar endavant el projecte, encara que em semblés que no s'avançava. Per tot això moltes gràcies i un plaer haver pogut compartir aquests anys plegats.

En segon lloc voldria agrair a Ifercat i l'Albert Alcarraz l'haver obert la porta d'aquest projecte, un projecte ambiciós del qual ja se n'estan veient els fruits. Sense ells tot això no hagués ni tan sols començat.

També tota la gent que forma part del departament de Teoria del Senyal i Comunicacions, en especial del grup Antenna Lab, com el Sebastià Blanch, el Lluís Jofre, l'Ángel Cardama, l'Albert Aguasca, l'Adriano Camps, així com la Teresa Pons i l'Aynie Khoe per preocupar-se per nosaltres i compartir riures administratius.

Per suposat, els amics de tota la vida, en especial el Jordi, el primer doctor del grup, qui ens ho anava a dir al parvulari. El Ferran, per demostrar que una altra vida és possible. Els companys del bàsquet també es mereixen un bon record aquí, tants anys lluitant per jugar bé, m'heu fet moltes més assistències fora del camp. Gràcies Chema per tantes lliçons i saber estar. Y a Roberto, por esa capacidad de sacrificio y buen humor. Eva, moltes gràcies per les flors i les fades. Mica en mica anem pel bon camí. A la gente del sur, Sole y Maru, por aportar sencillez y felicidad en cada momento. Qué suerte cruzarme con vosotras. La gent de teatre: tot un món nou, tantes relacions i tan properes, tanta sinceritat! Miqui, Manoel, Clàudia y Marina, un placer encontrarnos cada vez. Andrea, la de la pell més viva. Maria, una de les noies més fascinants que he conegut, espero aconsegueixis els teus somnis. Gràcies per inspirar tantes històries. Durant aquests anys he seguit compartint experiències, peripècies i grans estones amb companys de la universitat. Alberto i Dídac, sobre tot al viatge a Txèquia i Polònia. La Neus i la Sandra, el Jordi Díaz i la Maria, el Jose Molina, el Jordi Morata i sobre tot la Laura, el millor somriure de la ciutat, gràcies per tots aquests anys i els que ens queden per compartir.

Shambhu, also a great, great pleasure being able to meet someone like you. May your spirit and your family help those in Nepal who need an opportunity to rise your country. I will never forget our sincere talks and the visit to your village. One of the greatest honours of my life was meeting your family and the blessings your elders offered Javier and me. I hope you, Ambika and Anuska become one of the happiest families, there are no words to describe the joy that I feel when we share our time together.

Y toda la gente del laboratorio, la lista es larga pero no se puede dejar de lado. El día a día y la amistad de estos años harán que eche de menos seguir con vosotros: Xavi, Isaac, Enric, René, José Miguel y

Neri, Juanfer, Miguel Ángel, Sandra, Zabdiel, Aline, Enrique, Jordi, Cristian, Cristina, María, David, Sergi. Hugo, un casanova de los que no quedan. De Pablo y Luca sólo decir cosas buenas, así como de Raquel por su aguante y gran sonrisa, de Roberto por su estilo y familiaridad y ese viaje de despedida. Gràcies també a la Bea, pel bon humor, el millor somriure del Vallès Oriental. A l'equip de D3N3 - Òscar, Pere, Edu, Jordi Balcells -, amb qui vam disfrutar dels migdies entre cistelles. Als del viatge a Califòrnia (Edu, Santi, Gemma, Pere i Txema), va ser una experiència fantàstica, dels millors dies que recordo. El Xavi Banqué, amb els sopars a 3 bandes amb el Marco. A Juanma, tan tímido como buena gente, cásate ya!

Al Dr. Talone, Marco para los amigos, quería agradecerle especialmente todos los ratos juntos. Tanta clase parece que no puede ser cierta, pero es y la pude gozar con plenitud estos últimos años, compartiendo tantas mesas y cervezas que no se pueden contar. No conseguiste bailar, pero no se puede ser perfecto, aunque te acercas mucho.

Al estepario, Javi, decirte que eres la leche. Gracias por el viaje a Salamanca, los disfraces y el viaje a Nepal, es inolvidable con varios de los mejores momentos de mi vida. Gracias por ofrecer tu ayuda cuando se necesitaba. Me alegro de cómo te han salido las cosas, hay que currárselo como tú. Compartir polvorientas campañas sembradas de trenes inesperados, llaves dentro del maletero y cortes de luz da para mucho. Gran corazón, mejor tío.

Y acabo el laboratorio con Txema. Compartir mesa contigo y tus amigos y tus mensajes ha sido un delicioso viaje más allá de la ciencia. Qué bien hemos aprovechado el tiempo y la amistad. A ti y Laura agradeceros vuestra hospitalidad, sois una gran pareja de la que espero poder disfrutar mucho más. Que sigas contagiando tu risa natural por doquier. Te deseo mucha felicidad, tanta como me has entregado.

A dues persones molt especials, el Lluís i la Maria, que ja formen part de la meva família, agrair-los-hi les fabuloses estones compartides a tres bandes, molt especialment Cap sa Sal i Formentera. Més que amistat, estones inoblidables i entranyables. Una sort haver pogut trobar dues ànimes tant properes i amb tant bon cor, i desitjar-vos que les noves famílies que esteu fent créixer us facin tant feliços com hem estat junts.

A la familia agradecerle el ánimo y el cariño dispensado todos estos aos. A Pepe y Juli por ser una de las parejas más graciosas que conozco. Gracias por los buenos momentos, así como a Carlos, Mónica y Sebastián, Marichu y Clotilde.

Mi tieta Ofelia, una de las personas más agradecidas y cariñosas. Un placer visitarte y pasar un rato contigo cada fin de semana. A Lela, la mejor abuela y la más testaruda. Muchísimas gracias por ser tan gruñona y preocuparte tanto. Y mi tía favorita, Ofelia, esa sonrisa permanente y alegría sincera de vernos en tu casa no se olvida, gracias por ser tan acogedora y buena persona. A mi prima Ofe, por estar ahí cuando se la necesita, y a Rubén. A los dos gracias por darnos una alegría tan grande con Jorge. Y mi primo Jorge, mi ídolo, cómo te lo has currado, me alegro que las cosas te vayan tan bien, te lo mereces, así como una esposa tan maja como María.

M^{a}Ángeles, la última en llegar y la más lista! Quizá incluso la más loca. Te pasé la nocturnidad y ya no la sueltas, y cada día te veo mejor. Gracias por estos añitos, nos queda mucho por compartir.

Cristina, la mejor hermana que uno podría tener. Qué suerte tener una sonrisa tan preciosa y tan cerca! Ser tan buena gente tendrá su recompensa. Nos quedan muchas cosas por compartir y las viviremos juntos,

no dejaré que te escapes. La vida que tenemos por delante será fantástica.

Y mi madre, no sé como expresar la gratitud que siento hacia ti por todos estos años de buenos momentos. Qué suerte tener alguien que te quiere tanto, poco puedo pedir de ti que no me hayas dado. Tenemos muchos momentos por compartir, tan buenos como los pasados o más. La familia sin ti no sería lo que es y seguiremos juntos muchos años.

Y por último a mi padre, que se fue por el camino, pero nos dejó los valores con los que afrontar la vida. La disfrutaremos, y tú con nosotros.

x

Contents

List of Figures

List of Tables

Acronyms

ADI	Alternating Direction Implicit method
APWS	Angular Plane Wave Spectrum
APWS$_x$	Horizontal polarisation component of APWS
APWS$_y$	Vertical polarisation component of APWS
ATC	Automatic Train Control
BC	Boundary Conditions
ECDF	Empirical Cumulative Distribution Function
EM	ElectroMagnetic
FFT	Fast Fourier Transform
FT	Fourier Transform
GF	Green's Function
GSM	Global System for Mobile Communications
Hpol	Horizontal polarisation
IFFT	Inverse Fast Fourier Transform
IFT	Inverse Fourier Transform
ISM	Industrial, Scientific and Medical
L9	Línia 9
LCT	Lower Curved Tunnel
LoS	Line of Sight
LST	Lower Straight Tunnel
MIMO	Multiple Input, Multiple Output
P-R	Peaceman and Rachford
PCC	Central Control Point
PE	Parabolic Equation
PEC	Perfect Electric Conductor
PMC	Perfect Magnetic Conditions
QoS	Quality of Service
RMS	Root Mean Square
SIA	Spectral Iterative Algorithm

SIP	Spectral Incremental Propagation
SISO	Single Input, Single Output
SIT	Spectral Iterative Technique
SNR	Signal to Noise Ratio
SPE	Spectral components complying the Parabolic Equation regimen
TE	Transverse Electric mode
TETRA	TErrestrial Trunked RAdio
TM	Transverse Magnetic mode
TSC	Signal Theory and Communications
UMTS	Universal Mobile Telecommunications System
UPC	Technical University of Catalonia
UST	Upper Straight Tunnel
Vpol	Vertical polarisation
VPE	Vector Parabolic Equation

Chapter 1

Introduction

Development of communication technologies has quickly advanced over the last two decades. One of the most important changes has been the spreading of wireless communications systems and their introduction on our day-to-day routine.

The scope of this thesis is to assess the behaviour of wireless systems in closed environments, particularly in train tunnels. The opportunity arises during the construction of a new Metro line in Barcelona: Línia 9 (L9). Ifercat - Infraestructures Ferroviàries de Catalunya - is the entity leading the development of L9. The Signal Theory and Communications Department (TSC) of the Technical University of Catalonia (UPC) collaborates with Ifercat on the assessment of advanced communications systems for L9. This line is one of the longest ever built, connecting 5 urban nucleus along 48Km with 52 stations, and it offers interconnection between Barcelona airport El Prat, high-speed trains between Spain and France at La Sagrera Station, Barcelona exposition centre Barcelona Fira and Barcelona maritime Port among other services of interest.

Emphasis is put on using the latest technologies in all aspects of its development in order to obtain a premium quality transportation system with the following points:

1. Safety of train service users is the first priority.
2. The service must be on-time and fast.
3. It must be able to respond to user's demands.

To this end, several aspects of its operative characteristics are defined:

1. The operative control has to be centralised.
2. Processes and systems must be automatised.
3. Execution and exploitation costs must be minimised.

It has been proven that, in railway environments, most of the accidents are attributed to human mistakes. As a consequence L9 proposes a *driver-less* exploitation model: management of the transport system is automatic, with no personnel on board but transport users. The control of trains is executed from a Central

Control Point (PCC) who monitors the management of the whole L9. Hence, it is necessary to precisely know the real-time position and state of all trains circulating through L9 tunnels, as well as awareness of any event occurring at any point of the exploitation that may have an impact on the transport service. Because of the *driver-less* model, it is of paramount importance offering to the passengers the possibility of communicating with L9 authorities in emergency situations. It is equally important for the authorities to be able to gather information on the real state of the situation and to respond quickly if necessary. Several communications systems are thus used to meet these demands:

1. Two TETRA communications systems, one for L9 personnel and the other for emergency authorities such as Police and Fire Services.
2. The Automatic Train Control system (ATC), used for train control.
3. An on board surveillance video system, to provide the PCC visual real-time information of the facts taking place on the train carriages.

On top of the previous systems, the GSM and UMTS systems are also deployed. The International Telecommunications Union regulates TETRA services to be working at two bands: 380-400MHz and 410-430MHz. The GSM and UMTS systems use the well-known bands of GSM900 - 890-915MHz, 935-960MHz -, GSM1800 - 1.710-1.785GHz, 1.805-1.880GHz - and UMTS - 1.900-1.980 GHz and 2.110-2.170 GHz -. The ATC is a proprietary solution, working on a Wi-Fi system at the ISM band of 2.45GHz. The video surveillance system is chosen to operate at the ISM band of 5.8GHz because of its larger bandwidth. Summarising, Table 1.1 lists the services and frequency bands used in L9 facilities.

System	Description	Frequency band
TETRA Rescat	Used by Emergency services	380-400MHz
TETRA L9	Used by L9 personnel	410-430 MHz
GSM and UMTS	Users mobile devices	900MHz and 1800MHz
ATC	Train control	2.45GHz
Video	On board surveillance	5.8GHz

Table 1.1: Communications systems operating at L9.

The variety of systems originates a complex scenario from an ElectroMagnetic (EM) point of view. However, the solutions chosen to implement such systems are matured standards that should be able to work without interfering with each other. The most demanding system for operating reasons is the video surveillance system. It was chosen to operate at the 5.8GHz ISM band due to its larger bandwidth and less popularity among users. The idea is to be able to transmit 6 cameras simultaneously, placed at different points of the train carriages. The requirement in terms of bandwidth is set to 20MHz.

A possible solution would be the installation of radiating cable along the 48Km of tunnels and the rest of L9 facilities. This option was discarded by economical reasons: it would be very expensive not only completing the installation on the whole L9, but also the maintenance would be high due to the harsh conditions - humidity, rodents - present in tunnels.

A wireless system solves the issues presented by the radiating cable solution while providing a much more flexible option. A system of antennas conveniently deployed will be able to cover the whole L9 service at a much reasonable cost. Diversity techniques and Multiple Input Multiple Output antenna systems have been developed for the last few years in an attempt of increasing bandwidth between transmitting and receiving antennas. Even if space in tunnels is limited, the wavelength at such frequencies - on the order of a few centimetres - allows the introduction of MIMO systems in such scenarios to study their performance.

Although work has been done in the 5.8GHz band at indoor environments, tunnels present some particularities that have to be taken into consideration: propagation takes place predominantly in one direction, train circulation must be taken into account, bended tunnels reduce the Line of Sight distance, L9 tunnels have two separate cavities. The scope of this thesis is, thus, the study of the 5.8GHz ISM band and to assess the performance of MIMO systems in such scenarios. In order to do so the document is structured as follows: Chapter 2 introduces the concept of spectral propagation and gives a few tips on previous work with this technique. Chapter 3 particularises the theory detailed in the previous chapter and explains how it is used to implement an EM simulator. This tool allows predict EM propagation throughout the tunnel, and the validity of its results is discussed in Chapter 4. The following two chapters are devoted to the parabolic method, used to overcome some issues that could not be solved with spectral techniques: Chapter 5 describes the fundamentals of the parabolic equation while Chapter 6 addresses the results obtained with this tool. Finally, Chapter 7 shows the results of the measurement campaigns carried over during the development of this thesis at several Barcelona Metro facilities and the comparison with simulation predictions. The last chapter is devoted to the conclusions of the thesis.

Chapter 2

Fundamentals of Spectral Propagation

2.1 Electromagnetic Theory

2.1.1 Maxwell's Equations and Wave Equations

Maxwell's equations [1],[2] rule the relation between electric and magnetic fields according to the observable physical laws. Here are briefly introduced to put in context the EM propagation phenomena and the laws that govern it. On its differential representation they are specially suited for the study and characterisation of electromagnetic (EM) fields and/or sources placed in bounded media. The differential form of Maxwell's equations is expressed as:

$$\nabla \times \underline{E} = -\underline{M} - j\omega\underline{B} \tag{2.1}$$

$$\nabla \times \underline{H} = \underline{J} + j\omega\underline{D} \tag{2.2}$$

$$\nabla \cdot \underline{D} = \rho \tag{2.3}$$

$$\nabla \cdot \underline{B} = \tau \tag{2.4}$$

where:

$\underline{E}, \underline{H}$: electric and magnetic field intensities,

$\underline{D}, \underline{B}$: electric and magnetic flux densities,

$\underline{J}, \underline{M}$: electric and magnetic current densities,

ρ, τ: electric and magnetic charge densities.

A time-harmonic dependance with the corresponding instantaneous values of the form $e^{j\omega t}$ is assumed for all the variables involved.

The previous equations, however, can be further simplified by stating the relation between flux and intensity variables as:

$$\underline{D} = \epsilon\underline{E} \tag{2.5}$$

$$\underline{B} = \mu\underline{H} \tag{2.6}$$

where ϵ and μ account for the electric permittivity and magnetic permeability. In a lineal, homogeneous and isotropic medium these parameters are scalars whose value is constant. Maxwell's equations can therefore be written as:

$$\nabla \times \underline{E} = -\underline{M} - j\omega\mu\underline{H} \tag{2.7}$$

$$\nabla \times \underline{H} = \underline{J} + j\omega\epsilon\underline{E} \tag{2.8}$$

$$\nabla \cdot \underline{E} = \frac{\rho}{\epsilon} \tag{2.9}$$

$$\nabla \cdot \underline{H} = \frac{\tau}{\mu} \tag{2.10}$$

in a homogeneous non-dispersive medium. It is difficult, though, dealing with the previous expressions in order to find solutions to boundary value problems, as both curl equations are coupled partial differential equations of first order, involving two variables each. The wave equation represents a starting point better suited to work with such problems. By taking the curl on both sides of the first two Maxwell's equations:

$$\nabla \times \nabla \times \underline{E} = -\nabla \times \underline{M} - j\omega\mu\nabla \times \underline{H} \tag{2.11}$$

$$\nabla \times \nabla \times \underline{H} = \nabla \times \underline{J} + j\omega\epsilon\nabla \times \underline{E} \tag{2.12}$$

and using the vector identity

$$\nabla \times \nabla \times \underline{A} = \nabla(\nabla \cdot \underline{A}) - \nabla^2\underline{A} \tag{2.13}$$

Eqs.2.7 and 2.8 can be rewritten as

$$\nabla(\nabla \cdot \underline{E}) - \nabla^2\underline{E} = -\nabla \times \underline{M} - j\omega\mu\nabla \times \underline{H} \tag{2.14}$$

$$\nabla(\nabla \cdot \underline{H}) - \nabla^2\underline{H} = \nabla \times \underline{J} + j\omega\epsilon\nabla \times \underline{E} \tag{2.15}$$

Substituting the third and fourth Maxwell equations and regrouping terms a preliminar form for the wave equations is derived:

$$\nabla^2\underline{E} = \nabla \times \underline{M} + j\omega\mu\nabla \times \underline{H} + \nabla\left(\frac{\rho}{\epsilon}\right) \tag{2.16}$$

$$\nabla^2\underline{H} = -\nabla \times \underline{J} - j\omega\epsilon\nabla \times \underline{E} + \nabla\left(\frac{\tau}{\mu}\right) \tag{2.17}$$

Finally, considering a source-free region and recalling the first and second Maxwell equations again, expressions for the wave equations arise:

$$\nabla^2\underline{E} = -\omega^2\mu\epsilon\underline{E} \tag{2.18}$$

$$\nabla^2\underline{H} = -\omega^2\mu\epsilon\underline{H} \tag{2.19}$$

2.1.2 Equivalence Theorem

The Equivalence Theorem is widely used in problems involving aperture antennas: fields radiated by the antenna can be computed from the knowledge of field distribution at the antenna aperture. Radiation in

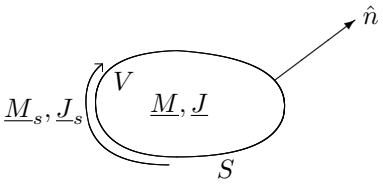

Figure 2.1: Enclosed volume containing electric and magnetic sources.

tunnels presents some similarities: it consists of an unknown field distribution radiated by sources in a closed bounded domain, so this tool can be used to help predicting field distribution in tunnels.

Suppose that a set of electric and magnetic sources $\underline{J}$ and $\underline{M}$ are enclosed inside a certain volume V and that S is the volume's limiting surface as that of Fig.2.1. Let $\hat{n}$ be the outward normal vector to S and $\underline{E}$ and $\underline{H}$ the fields radiated by the sources.

The equivalence principle states that the same radiated fields can be obtained from the tangential surface currents on S, $\underline{J}_s$ and $\underline{M}_s$, computed as:

$$\underline{J}_s = \hat{n} \times \underline{H} \tag{2.20}$$

$$\underline{M}_s = -\hat{n} \times \underline{E} \tag{2.21}$$

The surface currents satisfy the Boundary Conditions (BC) over the volume surface S and cancel the fields on the inner part of the volume V. If the tunnel cavity is chosen as the closed surface, knowledge of the radiating sources plus the tangential field over the tunnel boundary determines uniquely the radiated fields in the source-free region outside the surface. Initially, fields at the source plane are unknown, only the source currents will be specified by the transmitter. The use of the Equivalence Theorem allows to obtain the initial field distribution necessary for the spectral technique to start the propagation.

2.1.3 Image Theory

Source radiation can be substantially modified in the presence of bodies. It is not unusual in tunnels placing transmitting antennas close to the boundary walls, as the centre of the tunnel is usually preserved for train circulation. Even though tunnel walls are made of concrete, complex structures such as Barcelona L9 Metro require for the walls to be steel reinforced and/or to be build with large concrete blocks with a dense coarse metallic grid at their inner part. Train carriages themselves may have attached a transmitter close to their metallic surface to send onboard information to network control points. When placing a source - electric or magnetic - near a conductor, the outcome can be greatly enhanced or diminished. Fig.2.2 shows the relation existing between the source and its image.

The presence of a conductor in the vicinity of the source, whether it is a Perfect Electric Conductor (PEC) or Perfect Magnetic Conductor (PMC), is equivalent to place an imaginary source at a mirrored position once the conductor has been removed. The image has the same intensity and its sign is set according to the figure. Hence, the radiation of the source can either be cancelled or doubled. It seems therefore relevant to be very conscious of metallic bodies in enclosed areas with such less empty spaces, as tunnels with trains

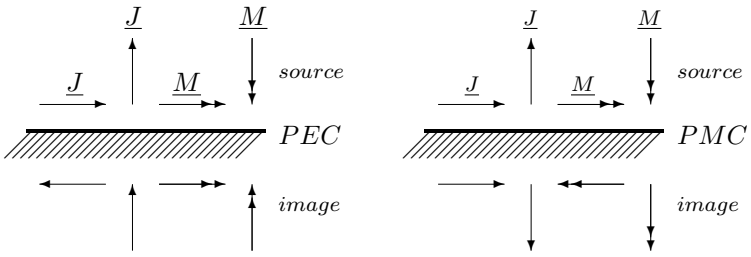

Figure 2.2: Images of electric and magnetic fonts.

or other metallic obstacles. The existence of such bodies can greatly modify the radiation pattern of the transmitting antennas and consequently the field distribution along the tunnel.

2.2 Fundamental Theory on Spectral Propagation

2.2.1 Introduction to Spectral Propagation

Spectral theory is based on the fact that a given field can be decomposed as the addition of multiple plane waves propagating in every direction of the space. The theory was originally developed by Bojarski [3],[4] in the early 70's, although applications did not arise until the following decade. By sampling a known field distribution on a given surface and applying the Fourier Transform (FT), the Angular Plane Wave Spectrum (APWS) is obtained. APWS contains the amplitude and phase information of each plane wave composing the sampled field. Propagation in the spectral domain between two parallel planes separated a distance Δz is easily achieved by multiplying the APWS by a phasor depending on Δz. Spectral methods take their advantage mainly from Fourier Transform symmetry properties and efficiency of current Fast Fourier Transform (FFT) and Inverse Fast Fourier Transform (IFFT) algorithms.

2.2.2 The Angular Plane Wave Spectrum

In communications, the Fourier Transform establishes a duality between time and frequency. The temporal characteristics of a signal are innerly-related to its time-frequency spectrum. Similarly, when dealing with spatial signal distributions, the application of the FT leads to the obtention of the angular information of such signals. That is the reason why it is called Angular Plane Wave Spectrum.

Signal domain	Transformed domain
t	f
x, y, z	k_x, k_y, k_z

Table 2.1: Equivalence of variables between domains.

Imagine a set of electric ($\underline{J}$) and magnetic ($\underline{M}$) sources in a certain region, and that the medium this

sources are placed at is free space. The following magnitudes can thus be computed:

$$\underline{B}_J(k_x,k_y) = (B_{Jx}, B_{Jy}, B_{Jz}) = FT\{\underline{J}(x,y,z)\} \tag{2.22}$$

$$\underline{B}_M(k_x,k_y) = (B_{Mx}, B_{My}, B_{Mz}) = FT\{\underline{M}(x,y,z)\} \tag{2.23}$$

Using the previous expressions, electric $\underline{A}_E$ and magnetic $\underline{A}_H$ APWS are obtained as [5]:

$$\underline{A}_E = \eta_0 \underline{\underline{X}}_1 \underline{B}_J(k_x,k_y) - \underline{\underline{X}}_2 \underline{B}_M(k_x,k_y) \tag{2.24}$$

$$\underline{A}_H = \frac{1}{\eta_0} \underline{\underline{X}}_1 \underline{B}_M(k_x,k_y) - \underline{\underline{X}}_2 \underline{B}_J(k_x,k_y) \tag{2.25}$$

where η_0 is the free space intrinsic impedance and $\underline{\underline{X}}_1$ and $\underline{\underline{X}}_2$ are known as the spectral tensors that can be expressed as:

$$\underline{\underline{X}}_1 = \frac{-k_0}{2k_z} \begin{pmatrix} 1-\frac{k_x^2}{k_0^2} & -\frac{k_x k_y}{k_0^2} & -\frac{k_x k_z}{k_0^2} \\ -\frac{k_x k_y}{k_0^2} & 1-\frac{k_y^2}{k_0^2} & -\frac{k_y k_z}{k_0^2} \\ -\frac{k_x k_z}{k_0^2} & -\frac{k_y k_z}{k_0^2} & 1-\frac{k_z^2}{k_0^2} \end{pmatrix} \tag{2.26}$$

$$\underline{\underline{X}}_2 = \frac{-k_0}{2k_z} \begin{pmatrix} 0 & -\frac{k_z}{k_0} & -\frac{k_y}{k_0} \\ -\frac{k_z}{k_0} & 0 & -\frac{k_x}{k_0} \\ -\frac{k_y}{k_0} & -\frac{k_x}{k_0} & 0 \end{pmatrix} \tag{2.27}$$

Spectral tensors $\underline{\underline{X}}_1$ and $\underline{\underline{X}}_2$ account for possible interactions between the different components of the current densities in the spectral domain. Once the APWS has been found, deriving the respective field distributions is straightforward by means of the Inverse Fourier Transform (IFT):

$$\underline{E}(x,y,z) = IFT\{\underline{A}_E(k_x,k_y)\} \tag{2.28}$$

$$\underline{H}(x,y,z) = IFT\{\underline{A}_H(k_x,k_y)\} \tag{2.29}$$

Hence, as it has been shown, radiated fields can be found from the source current distributions using the spectral tensors. This is not, however, the only way to do so: from the integral formulation of Maxwell equations, fields can be found by the convolution between Green's Function (GF) $\underline{G}$ and source currents:

$$\underline{E} = \underline{G} * \underline{J} \tag{2.30}$$

This operation can be much more efficiently computed in the spectral domain as the algebraic multiplication between respective FT's:

$$\underline{A}_E = FT\{\underline{G}\} \cdot \underline{B}_J \tag{2.31}$$

while $\underline{E}(x,y,z)$ can be recovered using Eq.2.28.

2.3 Previous Work with Spectral Techniques

2.3.1 The Spectral Iterative Technique (SIT)

This algorithm was initially developed in [6] for 2D planar surfaces and later extended for the 3D case. The algorithm finds the currents over PEC or dielectric lossy scatterers and iterates the process until the solution converges. The scheme of the two-dimensional procedure follows:

1. The scatterer is sampled in parallel planes along the z-axis as in Fig.2.3, and the initial value for its surface current distribution $\underline{J}^{(0)}$ along the planes is guessed.

2. The scattered field can be found following the steps defined in Section 2.2.2:

$$B_J^{(0)}(k_x, z) = FFT\left\{J^{(0)}(x, z)\right\} \tag{2.32}$$

$$A_E(k_x, z) = FFT\left\{\underline{G}(k_x)\right\} \cdot B_J^{(0)}(k_x, z) = \tag{2.33}$$

$$\tilde{\underline{G}}(k_x) \cdot B_J^{(0)}(k_x, z) \tag{2.34}$$

3. Field in the spatial domain is obtained via IFFT. Afterwards it is forced to satisfy the BC and medium constitutive relationships:

$$E(x, z) = IFFT\{A_E(k_x, z)\} \tag{2.35}$$

$$E_{BC}(x, z) = M_{BC}\left\{E(x, z)\right\} \tag{2.36}$$

   with $M_{BC}\{\cdot\}$ an operator defined as a function of the appropriate BC.

4. An updated value of the current surface distribution, $\underline{J}^{(1)}$, is found following the next steps:

$$A_E(k_x, z) = FFT\{E_{BC}(x, z)\} \tag{2.37}$$

$$B_J^{(1)}(k_x, z) = \tilde{G}(k_x)^{-1} \cdot A_E(k_x, z) \tag{2.38}$$

$$J^{(1)}(x, z) = IFFT\left\{B_J^{(1)}(k_x, z)\right\} \tag{2.39}$$

Convergence of the solution is checked at this point and further iterations are performed if needed. The main drawbacks of the algorithm are:

- The initial values chosen for $\underline{J}^{(0)}$ determine whether convergence may be reached.
- Computational burden, as two FFT-IFFT transforms must be computed for each iteration. The algorithm is based on the surface currents and uses the FFT-IFFT conversion once to relate currents $\underline{J}$ with scattered fields $\underline{E}$. A second FFT-IFFT conversion is performed to update the currents on the scatterer surface.

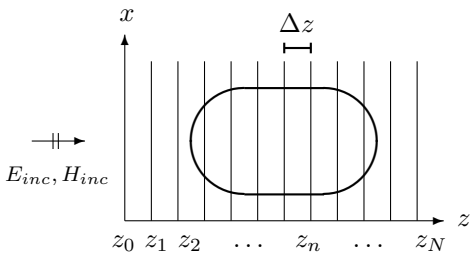

Figure 2.3: The SIT problem scheme.

2.3.2 The Spectral Incremental Propagation (SIP)

This procedure is described in [7] and [8], and it is similar to the previous one with the advantage of dealing directly with scattered fields instead of current distributions, so the computational cost is reduced significantly. The scheme of the three-dimensional version is:

1. The incident field $\underline{E}(x, y, z = z_0)$ is specified and the scatterer is sampled in parallel planes.

2. The APWS at $z = z_0$ is found:

$$\underline{A}_E(k_x, k_y, z = z_0) = FFT\left\{\underline{E}(x, y, z = z_0)\right\} \tag{2.40}$$

3. Propagation to the next plane $z = z_1$ is computed multiplying the APWS with a phasor:

$$\underline{A}_E(k_x, k_y, z = z_1) = \underline{A}_E(k_x, k_y, z = z_0)e^{jk_z\Delta z} \tag{2.41}$$

   where $\Delta z = z_1 - z_0$ and $k_z = \sqrt{k^2 - k_x^2 - k_y^2}$.

4. Field distribution $\underline{E}(x, y, z = z_1)$ is obtained from $\underline{A}_E(k_x, k_y, z = z_1)$ via IFFT. Finally, the corresponding BC are forced in the spatial domain:

$$\underline{E}(x, y, z = z_1) = IFFT\left\{\underline{A}_E(k_x, k_y, z = z_1)\right\} \tag{2.42}$$

$$\underline{E}_{BC}(x, y, z = z_1) = M_{BC}\left\{\underline{E}(x, y, z = z_1)\right\} \tag{2.43}$$

The previous steps are repeated until the final plane $z = z_N$ is reached. This method uses the equivalence theorem at each transversal plane, computing the equivalent currents at z_n and determining the radiated fields by these currents at $z = z_{n+1}$. When applying the BC, fields are truncated, i.e. forced to 0, inside PEC bodies. The truncation function is equivalent to convolute the APWS with a GF whose wavenumber k is complex and so it is guaranteed that fields will not propagate through metallic surfaces as attenuation will be high.

SIP presents several advantages respect to SIT:

- Only one FFT-IFFT conversion per step is needed, as SIP works with fields instead of currents.
- Convergence problems in SIT are avoided, as there is no need of guessing the initial current over the scatterer.
- Just a single pass through all the planes must be done. As results presented in [8] show, this method provides accurate near zone predictions for scattered fields. An end-to-beginning propagation may be needed if the backward-scattered radiation is worth of being considered.

However, SIP still presents some issues that must be addressed:

- The algorithm deals only with PEC scatterers, so dielectric structures cannot be included for analysis.

- Propagation of truncated fields is equivalent to propagate the surface magnetic currents, but also the field radiated by non-existent interior currents. The error introduced by this factor can be minimised by using small propagation steps Δz. To correctly propagate the truncated field, the scattered field should be computed from the convolution of the incident field with a GF that takes into account the presence of the conductor. The inaccuracies are due the use of the GF in free space.

- Computational cost increases if Δz is small, as uniform sections cannot be analysed in a single step.

- Interaction between scatterers contained in the same plane does not occur, as the effect of the respective equivalent currents takes place when propagation to the next plane has been computed. Several forward-backward iterations may be needed to take into account this higher-order interactions.

2.3.3 The Spectral Iterative Algorithm (SIA)

Some drawbacks of the SIP algorithm were solved in the version that Broquetas [9], Lozano [10] and Rius [11],[12] implemented at UPC, although the core of the algorithm was essentially the same as in SIP. To summarize the main differences:

- Fields are not truncated inside PEC bodies, the field is forced to 0 only in the conductor's surface. Currents on its inside are set according to image theory. The equivalence between the original and the new problem is ensured by the Huygens principle.

- As a consequence, the algorithm is allowed to use large Δz steps, taking advantage of the transversal cross-section homogeneity and reducing the computational cost. Hence, this parameter depends only on the structure's complexity and not on its electrical dimensions.

- On the other hand, the use of image theory limits the structures to be analyzed to PEC or PMC surfaces. Therefore this version of SIA is not suited to model EM propagation in tunnels.

Chapter 3

Spectral Propagation in Bounded Media

The scope of this thesis is EM characterisation in tunnel environments. Thus, BC cannot be applied by means of image theory, as tunnel walls are not metallic conductors but rather dielectric materials, and their dielectric properties have a notorious impact on propagation. This leads to the use of small incremental steps and to increase the complexity of simulations in order to avoid large inaccuracies on the predicted field distribution. Hence complexity does not solely depend on the structure under analysis anymore, but also on the electrical dimensions of the simulated scenario.

The algorithm described in this section is based on the fundamental spectral theory described in Section 2.2 and particularised for tunnels, overcoming some limitations of the stressed techniques.

3.1 Spectral Propagation

Spectral propagation is an iterative process that finds the solution of a given EM problem as the wavefront radiated by a source or an illuminating field advances through a defined scenario. The scenario, for instance that of Fig.2.3, is sampled in parallel planes that are orthogonal to the direction of propagation. An initial current or field distribution is specified and, from there, field distribution throughout the tunnel can be predicted. Fig.3.1 offers an example of propagation with a given field distribution at $z = 0$ and the predicted field at $z = 20m$. See how the radiated field expands spherically from the punctual source, unbounded through space.

The basic mechanism of propagation is detailed as follows:

- Field distribution in the spatial domain, $\underline{\underline{E}}(x, y, z = z_0)$, is defined at $z = z_0$.
- The corresponding APWS in the spectral domain, $\underline{\underline{A}}_E(k_x, k_y, z = z_0)$, is found by means of the FFT.
- The APWS at $z = z_1$, $\underline{\underline{A}}_E^{(k+1)}$, is computed with a simple multiplication between $\underline{\underline{A}}(x, y, z = z_0)$ and phasor $e^{-jk_z(z_1-z_0)}$.

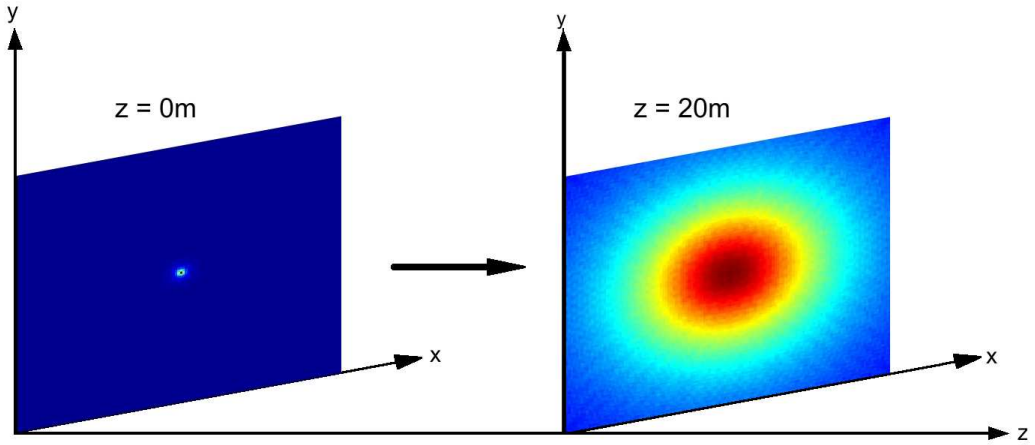

Figure 3.1: Reference coordinate axis in the spatial domain.

- Field distribution in the spatial domain at $z = z_1$, $\underline{\underline{E}}(x, y, z = z_1)$, is obtained via IFFT from $\underline{\underline{A}}_E(k_x, k_y, z = z_1)$.

- BC are enforced over $\underline{\underline{E}}(x, y, z = z_1)$ along the boundary.

This process is iterated as the wavefront progresses and reaches the end of the tunnel. The propagation scheme is summarised in Fig.3.1.

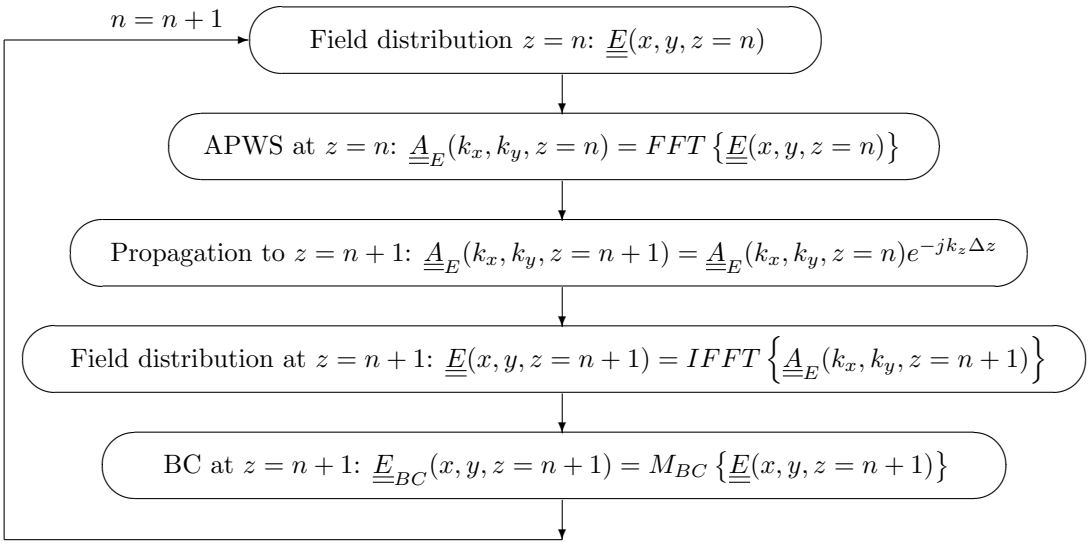

Figure 3.2: Spectral Propagation Iterative Scheme.

$M_{BC}\{\cdot\}$ is an operator that applies the BC on $\underline{\underline{E}}$ depending on the tunnel geometry and electrical properties.

3.1.1 Spatial Domain

The coordinate axis must be first oriented in the spatial domain. The z-axis is chosen as the longitudinal axis, while the x- and y-axis define the transversal plane with x corresponding to the horizontal direction and y to the vertical one, as in Fig.3.1. Because simulations are run with finite precision, domains must be discretised. Axis discretisation is reflected in the following expressions:

$$x = l\Delta x \tag{3.1}$$

$$y = m\Delta y \tag{3.2}$$

$$z = n\Delta z \tag{3.3}$$

with Δx, Δy and Δz the distance between consecutive points along the respective axis and indices l, m and n being natural numbers:

$$l = 1, 2, \cdots, i, \cdots, L$$

$$m = 1, 2, \cdots, j, \cdots, M$$

$$n = 1, 2, \cdots, k, \cdots, N$$

The working frequency determines how the geometric space is sampled and the number of points L, M and N needed for simulations. Nyquist criteria must be fulfilled to ensure that no information is lost during FFT-IFFT conversions. Let F_s the sampling frequency and λ_s the corresponding wavelength. Nyquist condition can be stated as:

$$(\Delta x, \Delta y) \leq \lambda_s/2 \tag{3.4}$$

Sampling distances Δx and Δy are defined as a function of λ_s. Once this parameters have been set and the tunnel cross-section dimensions are known, the number of points L and M can be found. Due to the geometrical characteristics of tunnels, the algorithm works with transversal square matrices and, to optimise the performance of FFT methods the number of points is chosen to be equal to a power of 2. Thus $L = M = 2^p$.

If resolution in the transversal dimensions x and y is bounded by the Nyquist criteria to avoid aliasing, resolution in the longitudinal direction is limited by the inaccuracies due to the use of the free space GF: the larger the Δz step, the more the fields will spread outside of the tunnel cavity, causing larger losses of the energy contained inside and less contributions caused by reflections. To assess the importance of this parameter see Fig.3.3, where a circular tunnel has been simulated for different values of Δz. As it can be seen, traces differ significantly not just on the periodicity of fadings, but also on the overall behaviour. Table 3.1 shows the attenuation in the 100m-500m range for each case. Again, differences are remarkable, thus making the election of this parameter crucial to obtain accurate predictions of the field strength along the tunnel.

3.1.2 Spectral domain

The spatial domain gives information on the field distribution over the whole tunnel geometry, whereas the spectral domain provides information on how plane waves composing the progressing wavefront propagate.

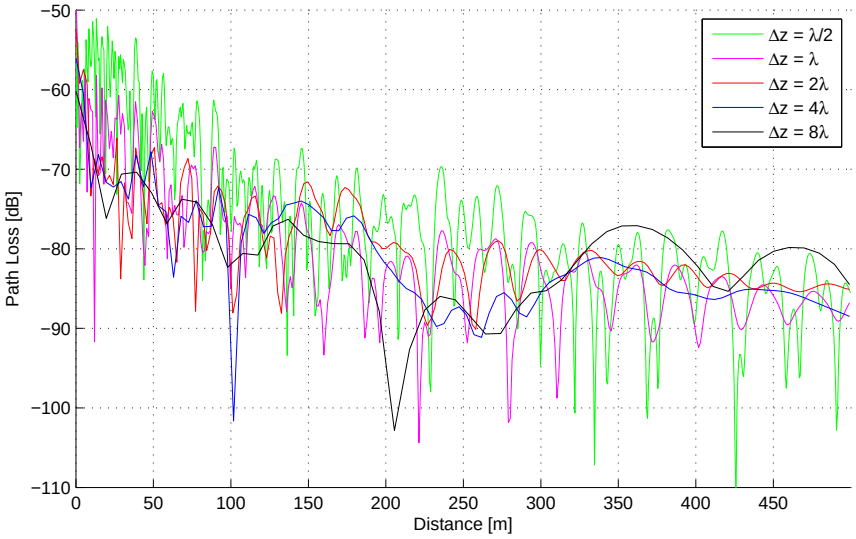

Figure 3.3: Simulation comparison for different Δz values.

Δz	Att (dB/100m)
$\lambda_s/2$	3.60
λ_s	2.07
$2\lambda_s$	2.02
$4\lambda_s$	1.99
$8\lambda_s$	0.53

Table 3.1: Attenuation for the different Δz cases in Fig.3.3.

The variables used in this domain are k_x, k_y and k_z. The former two are related to the spatial domain as follows:

$$k_x = \left[\frac{-\pi}{\Delta x}, \frac{\pi}{\Delta x}\right]; \tag{3.5}$$

$$k_y = \left[\frac{-\pi}{\Delta y}, \frac{\pi}{\Delta y}\right]; \tag{3.6}$$

In a discrete spatial domain with L and M points in the x and y axis respectively, resolution in the spectral domain is:

$$\Delta k_x = \frac{2\pi}{L\Delta x} \tag{3.7}$$

$$\Delta k_y = \frac{2\pi}{M\Delta y} \tag{3.8}$$

Δk_x and Δk_y represent the angular distance allowing to discriminate between two plane waves propagating in different directions. The third variable, k_z, is related to the former two by:

$$k_z = \sqrt{k_0^2 - k_x^2 - k_y^2} \tag{3.9}$$

with k_0 the free-space wavenumber. Typically, k_z is of the form presented in Fig.3.4, where its Real ($\Re$) and Imaginary ($\Im$) parts are shown. The points in the bell-shaped central part belong to the $\Re$ domain

and correspond to plane wave components that propagate all over the free space without being attenuated. This region of the spectrum is called *Visible*. On the other hand, points outside the bell belong to the $\Im$ domain, whose components suffer of severe attenuation and thus do not contribute to propagation in the long term. That is why it is called the *Evanescent* part of the spectrum. The angular range comprised beneath *Visible* borders corresponds to plane waves propagating within an angular range up to 90° respect to z-axis, i.e.: only components propagating in *forward* direction are being considered with the spectral technique. In certain situations backscattering - see Section 3.2.4 - must be taken into account and a *backward* pass must be added to the simulation process. In a more rigorous way, *Visible* and *Evanescent* regions are defined in Eqs.3.10 and 3.11 as a function of k_x and k_y:

$$k_x^2 + k_y^2 \leq k_0^2 \quad , \quad k_z \in \Re,\ Visible \tag{3.10}$$

$$k_x^2 + k_y^2 > k_0^2 \quad , \quad k_z \in \Im,\ Evanescent \tag{3.11}$$

From the previous expressions, the *Visible* region is a circumference of radius k_0 centred in the middle of the spectrum, while the area outside of the circumference belongs to the *Evanescent*.

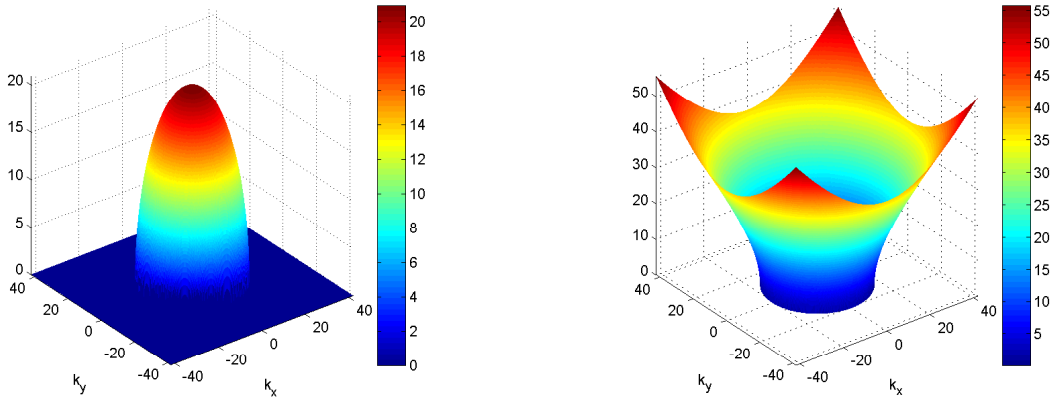

(a) Visible ($\Re(k_z)$) part of the spectrum

(b) Imaginary ($\Im(k_z)$) part of the spectrum

Figure 3.4: k_z Real and Imaginary parts.

The APWS provides the phase and magnitude values for all the plane waves that propagate along the tunnel. The FT of a plane wave is a Delta function whose position in the spectrum is set according to its propagation direction. Consider an angle of propagation θ_i being measured from the z-axis as in Fig.3.5: a plane wave with $\theta_1 = 0°$ would be placed at the centre of the spectrum, whereas another with $\theta_2 = 90°$ would be placed over the border between the *Visible* and *Evanescent* regions. The relation between the propagation angle and the corresponding displacement from the centre of the spectrum is shown in Section 3.2.3.

3.1.3 Green's Function

Spectral techniques take advantage of working between two domains: spatial and angular. As it has been seen, propagation starts once the initial field distribution is found. Two methods have been outlined in

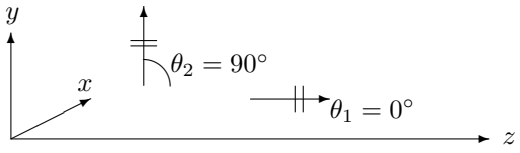

Figure 3.5: Plane waves propagating in the tunnel.

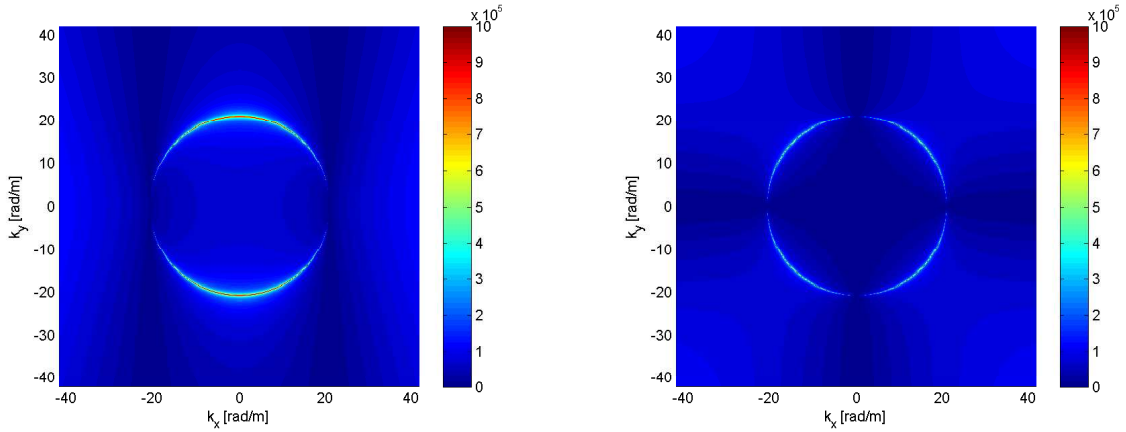

(a) Co-polar component. Magnitude

(b) Cross-polar component. Magnitude

Figure 3.6: APWS obtained via spectral tensors.

Section 2.2.2 to do so: application of spectral tensors of Eqs.2.26 and 2.27 on source currents or by means of the Green's Function (GF). Theoretically, both methods yield the same results but, when tried to derive the initial APWS via $\underline{\underline{X}}_1$ and $\underline{\underline{X}}_2$ some problems arise: strong peaks appear along the border between *Visible* and *Evanescent* regions. These peaks have to be filtered in order to obtain reasonable field distributions. The origin of the peaks is associated to the singularities of the quotient $-k_0/2k_z$ in Eqs3.10,3.11. On top of that, the width and position of the peaks vary depending on the simulation parameters. The anomalies are shown in Fig.3.6, where the APWS is shown with its co-polar and cross-polar components. There are small peaks with high values that distort fields when the IFFT is applied. Obtaining the APWS via the GF fixes the mentioned disadvantages while providing valid results in a more natural way, so this option is chosen to be implemented in the simulator.

The spectral technique presented here assumes that propagation takes place in free space even when propagation in bounded environments is being considered. When small incremental steps Δz are used, the inaccuracies are reduced and the previous assumption holds.

In electromagnetics, the solution to Helmholtz's equation [1] when a point source is driven as the system excitation is called Green's Function. It is therefore equivalent to the impulse response of circuit analysis theory. For a source placed at the origin in free space, the solution has the following analytical expression in spherical coordinates:

$$G(r) = \frac{e^{\pm jkr}}{4\pi r} \tag{3.12}$$

that corresponds to a spherical wavefront propagating in every direction of space. Suppose that an

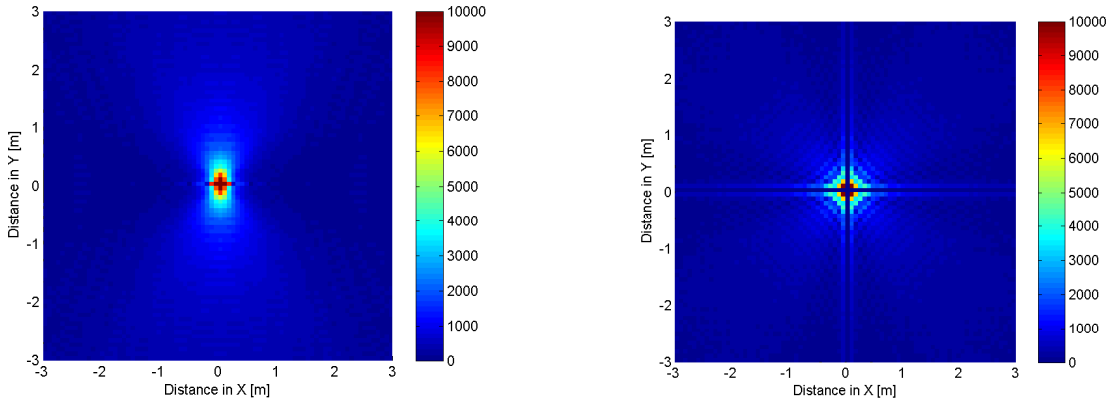

(a) Co-polar component. Magnitude

(b) Cross-polar component. Magnitude

Figure 3.7: Field distribution at the source plane obtained via spectral tensors.

elemental dipole of length $L_{dip} << \lambda$ is placed at the origin. Radiation in the far field region of the antenna can be obtained according to [13]:

$$E_\theta(\theta,\phi,r) = E_0 \cos(\theta)\sin(\phi)\frac{e^{-jkr}}{r} \tag{3.13}$$

$$E_\phi(\theta,\phi,r) = E_0 \cos(\phi)\frac{e^{-jkr}}{r} \tag{3.14}$$

Variable ϕ is azimuth in the XY-plane, θ is elevation from the z-axis and r is the distance between field points and the origin. Field components E_θ and E_ϕ are converted to cartesian coordinates, resulting in transversal field components E_x and E_y at $z = z_d$:

$$E_x(x,y,z=z_d) = \cos(\theta)\cos(\phi)E_\theta - \sin(\phi)E_\phi \tag{3.15}$$

$$E_y(x,y,z=z_d) = \cos(\theta)\sin(\phi)E_\theta - \cos(\phi)E_\phi \tag{3.16}$$

Afterwards, the FT of the cartesian components is computed and backpropagation to the source plane is performed in a single step. Field distribution at $z = 0$ is recovered with the IFFT:

$$\underline{A}_E(k_x,k_y,z=z_d) = FFT\left\{\underline{E}(x,y,z=z_d)\right\} \tag{3.17}$$

$$\underline{A}_E(k_x,k_y,z=0) = \underline{A}_E(k_x,k_y,z=z_d)e^{+jk_0z_d} \tag{3.18}$$

$$\underline{E}(x,y,z=0) = IFFT\left\{\underline{A}_E(k_x,k_y,z=0)\right\} \tag{3.19}$$

What has been obtained is the system GF: using the radiated far-field analytical expressions for an elemental dipole, the excitation at the source plane has been found. The impulse response is convoluted with the initial current distribution in the spectral domain (Eq.2.31). To obtain the field distribution at $z = 0$ Eq.2.28 is used. As has been said in Section 2.2.2, this process must only be used for the first iteration, as for subsequent transversal planes the simulator does not deal with currents but with field distributions instead. At that point, conversions between spatial and spectral domain is done with FFT and IFFT.

It is worth analysing the results obtained with both the spectral tensors and the GF. First of all compare the APWS obtained via the GF in Fig.3.8 and that of Fig.3.6, obtained via spectral tensors. See how the

modulus amplitude is much more reasonable for the former. This is also reflected for the co-polar and cross-polar components of the field distributions when comparing Figs.3.7 and 3.9. Although both cases offer similar results in terms of radiation pattern - the point source radiating a 2D-*sinc* function for the co-polar component and a 4-lobe diagonal pattern for the cross-polar component - the amplitude levels are certainly better for the GF case, so this one is chosen as the method used to obtain the field distribution at the source plane.

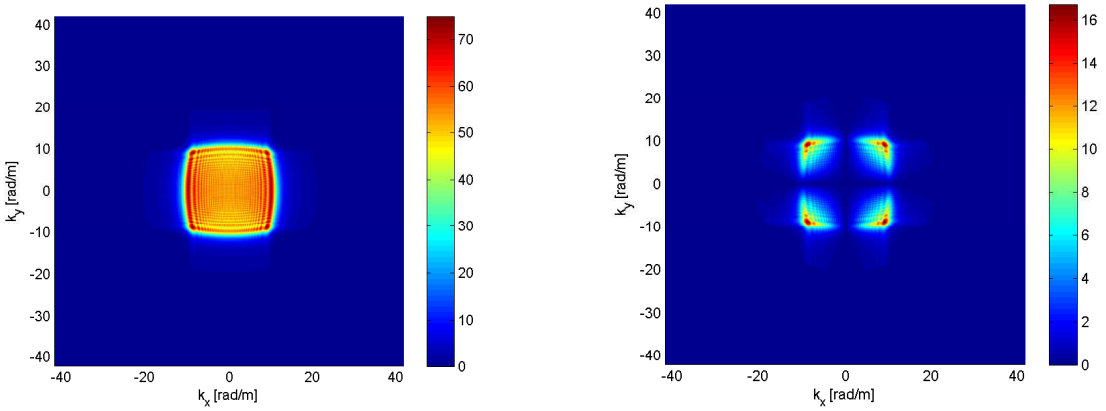

(a) Co-polar Component. Magnitude

(b) Cross-polar Component. Magnitude

Figure 3.8: APWS obtained with the simulator's Green Function.

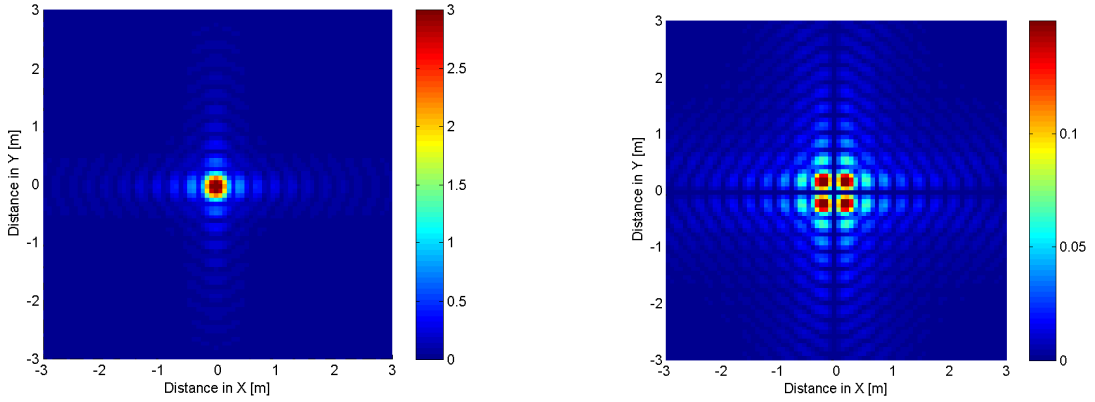

(a) Co-polar Component. Magnitude

(b) Cross-polar Component. Magnitude

Figure 3.9: Field distribution at the source plane obtained with the simulator's Green Function.

3.2 Propagation in Tunnel Environments

Tunnels are complex cylindrical structures used to ease or shorten the transport between emplacements. Radiowave tunnel propagation has long been discussed for several years. It is generally admitted that the structure acts as a waveguide, with the signal strength decreasing as a function of distance while fields are

confined on its inside. Boundary conditions, as detailed Section 3.3, have a definitive impact on propagation, but there are several other elements that can have an impact too. This section is devoted to the description of such elements as well as giving an overview of the field distribution in tunnels.

3.2.1 Tunnel Cross-Section

The cylindrical profile is the first thing to look at when working with tunnels. The geometry of the tunnel determines the characteristics of propagation. The impact of the cross-section can be observed in Fig.3.10, where a straight $500m$-long tunnel has been simulated with two different tunnel profiles: circular and rectangular. Note how the attenuation differs as a function of the profile. On subsequent chapters, though, a couple of techniques will be outlined describing the use of equivalent rectangular instead of more complex profiles. The reason after those equivalences is that the rectangular profile eases the EM analysis of propagation because modal expressions of the propagating modes in rectangular tunnels are way simpler than for other cross-sections. In this particular case, theoretical attenuations corresponding to the circular and rectangular simulated tunnels - the former with $2m$ radius, the latter with $4m$ x $3m$ side sizes, thus similar cross-sectional areas - are $-50.8dB/100m$ [14] and $-58.4dB/100m$ [15]. The attenuations provided by the spectral technique are $-24.6dB/100m$ and $-30.1dB/100m$ respectively. Though predicted values obtained do not match with theoretical results - the reason after these differences is due to application of boundary conditions, as it will be discussed later - it can be seen how the behaviour is correctly predicted by the simulator: larger attenuation corresponds to the rectangular case.

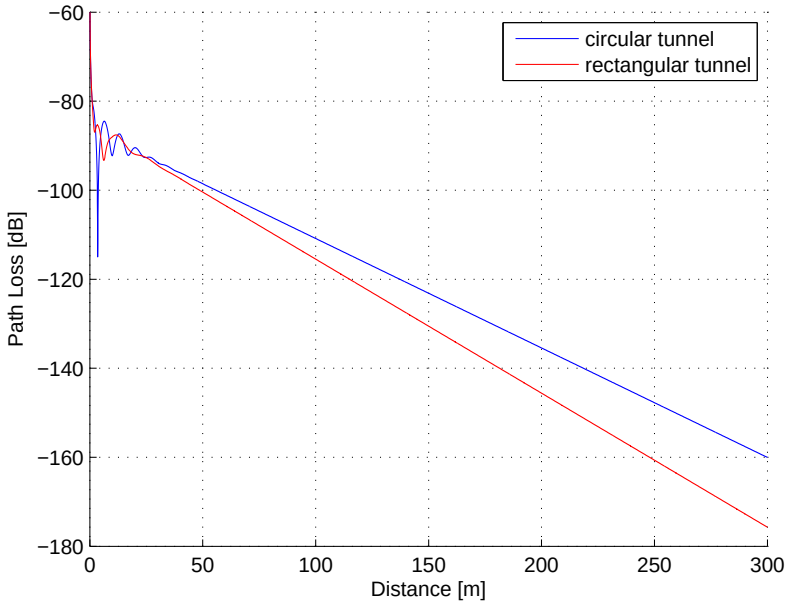

Figure 3.10: Propagation comparison with different tunnel cross-section.

The case attaining this thesis presents some particularities, as the tunnel of Metro Línia 9 (L9) in Barcelona has the split-circular shape of Fig.3.11. Trains circulate in opposite directions on the lower and

upper halves of the tunnel. There are notorious differences between them: an arched profile for the upper half and a quasi-rectangular for the lower one.

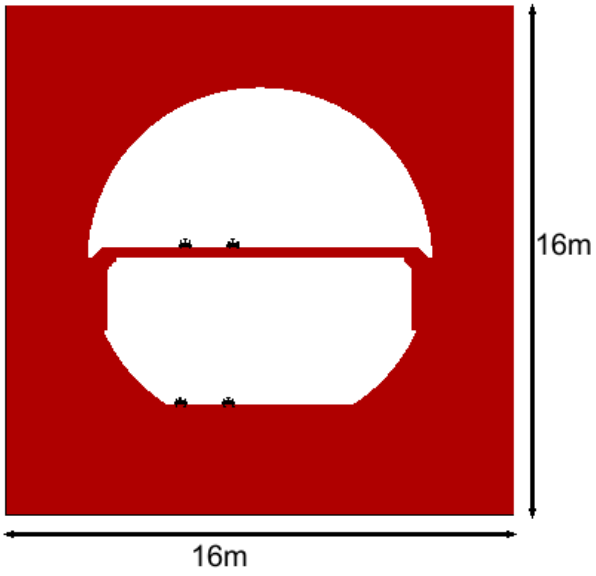

Figure 3.11: L9 Tunnel cross-section.

One of the featured characteristics of L9 is the use of wireless technologies for train control and communications systems. Trains are controlled automatically while circulating in opposite directions in the upper and lower halves. Hence, two simultaneous radio links are needed. Imagine the tunnel at, for instance, 10 meters before a station: the upper train accelerating to go to the next station with the other one slowing down while arriving to the station. Interference between both systems is dangerous and unacceptable. For this purpose, the deployment of a cell network is needed. In tunnels with a singular cavity, only two frequencies are needed, as adjacent cells use alternate carriers. In L9 tunnels, though, frequency planning may become more complex: each train will obey different orders and send its own information. As a consequence, they must use different carriers to avoid interfere with each other. Depending on the isolation degree provided by the intermediate platform, the frequency planning may need more carriers for the system to work interference-free. Because there is interest on studying how much the coupling between both parts is and how wireless systems work on the opposite cavities, the tunnel geometry was considered as a whole.

3.2.2 Variations in the Tunnel Cross-section

The performance of railway transport systems needs of several elements that may modify the tunnel profile for considerable stretches. Circumstances leading to these changes are: presence of trains, stations and other exploitation-related rooms - emergency corridors, communications and power supply areas - and tunnel ramps. The latter case is special relevance for the radio network planning, as the presence of the ramp increase the coupling between the upper and lower halves.

Two examples are presented next to illustrate how variations in the tunnel profile have an effect on

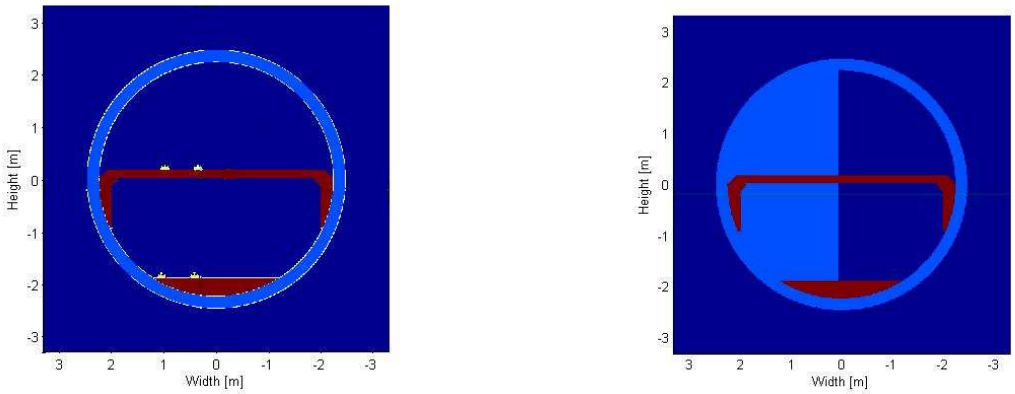

(a) Empty tunnel

(b) Blocked tunnel

Figure 3.12: Simulated L9 cross-sections.

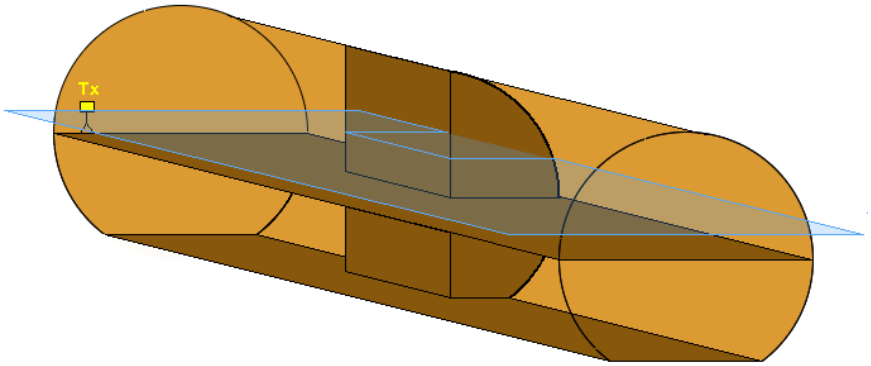

Figure 3.13: Half-blocked tunnel. In blue, the horizontal cut corresponding to Fig.3.14.

propagation. The first consists of the L9 tunnel, horizontally split in two halves as in Fig.3.12a, is used in this example for the first $20m$, followed by $20m$ of the partially blocked section of Fig.3.12b and finally a $20m$ stretch with the initial cross-section. The antenna is placed close to the lateral wall in the upper half of the tunnel. See Fig.3.13 for clearer details of the situation. The horizontal cut of the distribution inside the straight tunnel is depicted in Fig.3.14. The shadowed area corresponds to the concrete structure. See how fields are reflected at the tunnel walls and diffracted at the corners, while the blocking structure is followed with a shadow area and a noticeable signal drop-off. The latter effect is specially relevant in curved tunnels where, on top of the reduced Line of Sight (LoS) range, partially blocked sections will produce a drastic increase on losses.

Results are coherent respect to what is expected: ripple due to reflections, diffracted paths, fadings and shadowing areas. The spectral simulator is able to model correctly sharp changes in the tunnel.

For the second example, a ramp is chosen: in this case the cross-section will be modified gradually. The scenario is that of Fig.3.15 with the transmitting antenna placed in the upper half and the receiver in the lower half.

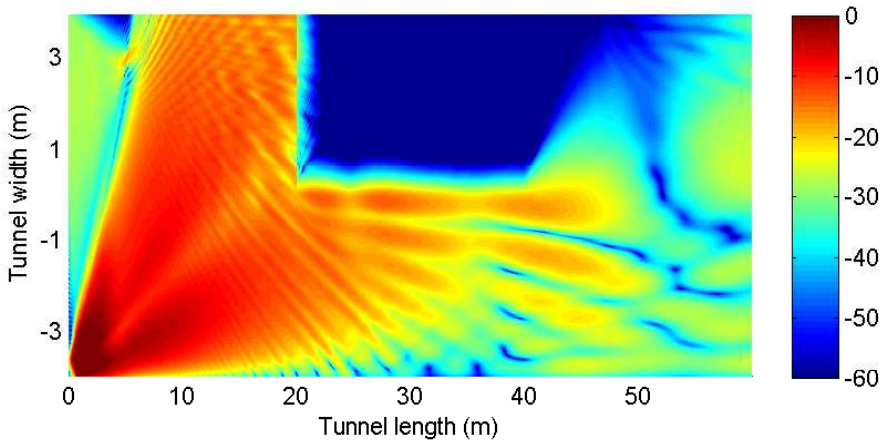

Figure 3.14: Partially blocked tunnel. Horizontal cut path losses.

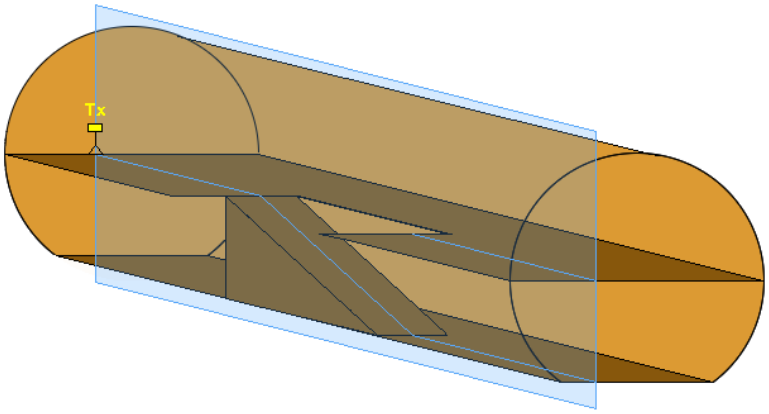

Figure 3.15: Tunnel with ramp. In blue, the vertical cut corresponding to Fig.3.16.

The ramp begins around $5m$ and ends at $26m$. Afterwards the cross-section of Fig.3.12a is restored. The vertical cut of Fig.3.16 shows the field distribution. It is interesting to note that the platform splitting the tunnel does not provide complete isolation between the upper and lower halves. The signal level in the lower cavity is very low for the first $5m$, although there is small coupling. Once the ramp begins, though, see how fields in the lower half fade when fail to penetrate the ramp structure. Values used in this case were the same both for tunnels walls and platform: $\epsilon_r = 5$ and $\sigma = 0.02[S/m]$. Empty space in the lower half starts to open, fields spread throughout due to the overture in the platform. Fig.3.17 shows the axial path losses for transmitter - in the upper half - and receiver - in the lower half - for two cases: with and without ramp. Note that when the ramp is present, from the 15m mark to almost the tunnel end the difference between upper and lower cavities is less than 10dB. Path loss curves in the upper half are almost identical for both cases, with and without ramp, while in the lower half curves differ 20dB approximately.

Hence, it can be concluded that the ramp is an element to be strongly considered for wireless network deployment in tunnels, as distance between isofrequency cells should be increased to avoid interference

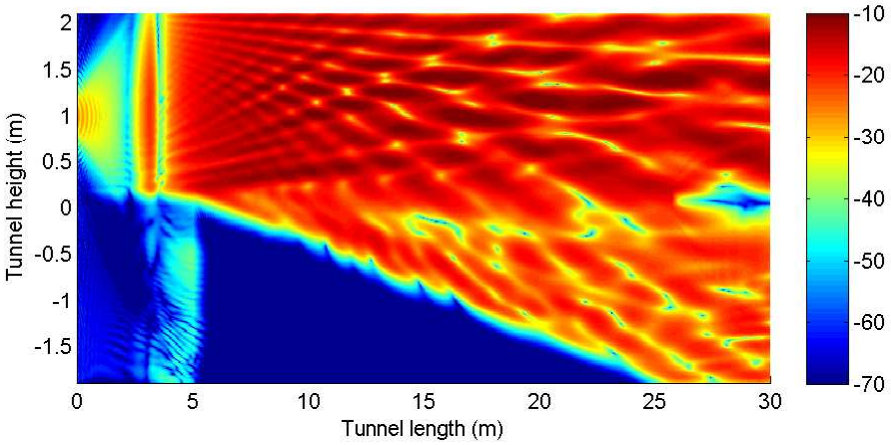

Figure 3.16: Tunnel with ramp. Vertical cut path losses.

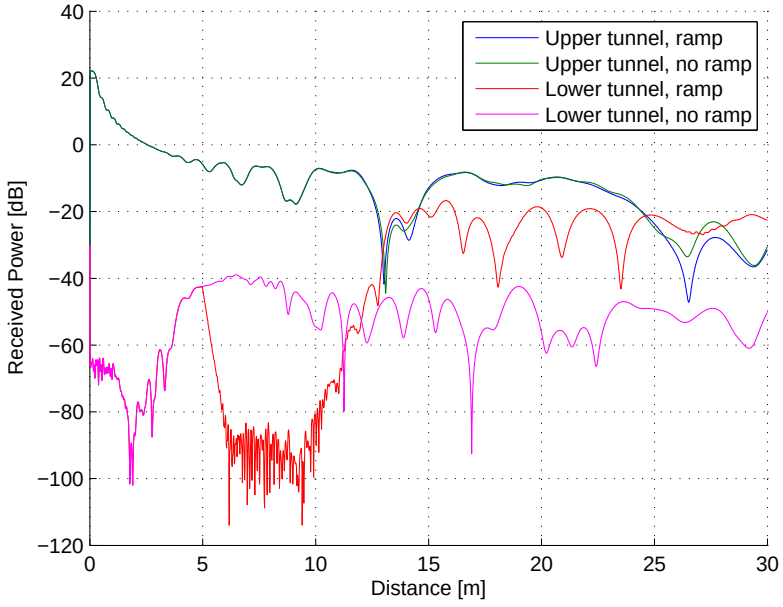

Figure 3.17: Tunnel with and without ramp. Axial received power.

between upper and lower nearby cells, forcing to expand the number of carrier frequencies needed.

3.2.3 Bended Tunnels

Bended tunnels prompt a change in the dynamics of propagation. In straight tunnels, waves propagating close to the tunnel axial direction dominate at long distances, whereas curves suppose an enrichment of the multipath characteristics and reduce the operating range of wireless systems due to a decrease of the Line of Sight (LoS) distance between transmitter and receiver. In such situations attenuation increases respect to straight tunnels, as waves suffer stronger attenuation due to reflections occurred at the tunnel boundaries when the curve begins. There are two approaches when modelling curved tunnels:

- Stick to the propagation axis z while modifying the tunnel cross-section as the wavefront advances (Fig.3.18).

- Reorientate progressively the coordinate axis in such a way that the z-axis coincides with the tunnel longitudinal axis after the curve, keeping the tunnel cross-section intact (Fig.3.19).

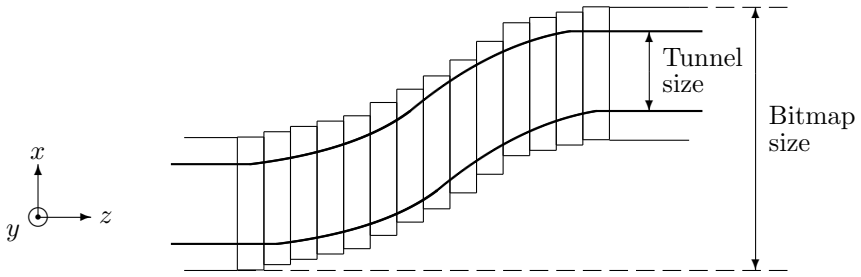

Figure 3.18: Curve discretisation shifting the cross section.

The first option implies changes in the cross section: as the wavefront progresses through the curve, the boundaries of the cross-section must be just shifted towards the side in small steps. This approach is discarded for two reasons: the first one is that it is not suited for large curvature radius because the number of points of the transversal matrices would be prohibitive as the cross-section is shifted towards the bounds of the matrices. The second reason is that tunnel paths not always zigzag, but just change the direction in which trains circulate, as in Fig.3.19. In this case there would be no advantage in using spectral propagation as done in this thesis: the z-axis would not longer be the longitudinal axis and fields in the transversal plane would not be known.

In the second approach, curves imply a change in the direction for which the progression of the wavefront must be computed. Waves whose angle of propagation is equal to the angle of rotation θ_i have then to be placed at the centre of the spectrum, that corresponds to the z direction or $\theta_i = 0°$. Basically, the spectrum must be shifted towards the appropriate direction. As a consequence the *Visible* will be partially shifted towards the *Evanescent*: the larger the θ_i angle, the larger the shifting and the losses. For a rotation such

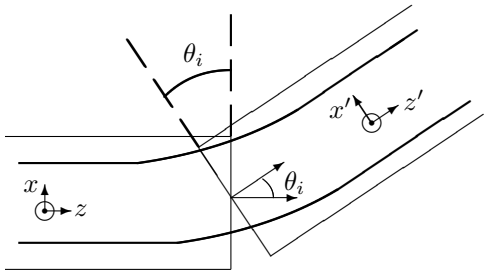

Figure 3.19: Curve discretisation with axis rotation.

as the one illustrated in Fig.3.19, axis in the spectral domain would be modified as:

$$k'_x = k_0 \sin\theta \cos\phi|_{\theta=\theta_i,\phi=0} = k_0 \sin\theta_i \tag{3.20}$$

$$k'_y = k_0 \sin\theta \sin\phi|_{\theta=\theta_i,\phi=0} = 0 \tag{3.21}$$

This means that the y-axis would remain the same while the x-axis would be modified due to a spectrum displacement of the k_x-axis of v samples, N being given by:

$$v = \frac{k'_x}{\Delta k_x} = \frac{k_0 \sin\theta_i}{\frac{2\pi}{L\Delta x}} = \frac{L\Delta x}{\lambda} \sin\theta_i \tag{3.22}$$

Isolating θ_i from the previous expression, the angle of propagation for a determined position in the spectrum can be known:

$$\theta_i = \arcsin\left(\frac{v\lambda}{L\Delta x}\right) \tag{3.23}$$

The drawback of this approach is that rotation of the axis - Fig.3.19 - leads to a loss of the energy contained in the *Visible* part of the spectrum. This effect can be minimised by applying several small rotations instead of trying to model the curve with a large single rotation. Suppose a 20m-long curved tunnel stretch. The curve is right-bended, and three cases are going to be analysed:

1. Case A: a single 15° rotation of the axis at the 10m mark.
2. Case B: a single 3° rotation of the axis at the 10m mark.
3. Case C: five consecutive 3° axis rotations to complete a 15° right rotation, starting at the 5m mark.

The electric field distribution at the 10m mark for cases A and B is presented at Fig.3.21. The transmitter is a point source slightly shifted to the left of the tunnel in order to increase the LOS distance. Figs.3.22a and 3.22b show the APWS modulus before and after rotation to illustrate how the spectral content is displaced away from the centre of the spectrum while preserving exactly the same spectral content. Fig. 3.23 shows the phase of the field distribution for the 15° and 3° rotations. The field modulus remains identical to that of Fig.3.21a.

On the other hand, comparing the phase of Fig.3.21b - previous rotation - with those in Fig.3.23, field distribution's phase suffers a significant change when the 15° rotation is applied in a single step -see Fig.3.23(a) - whereas a 3° rotation leads to smoother variations (Fig.3.23(b)). The difference can be explained as follows:

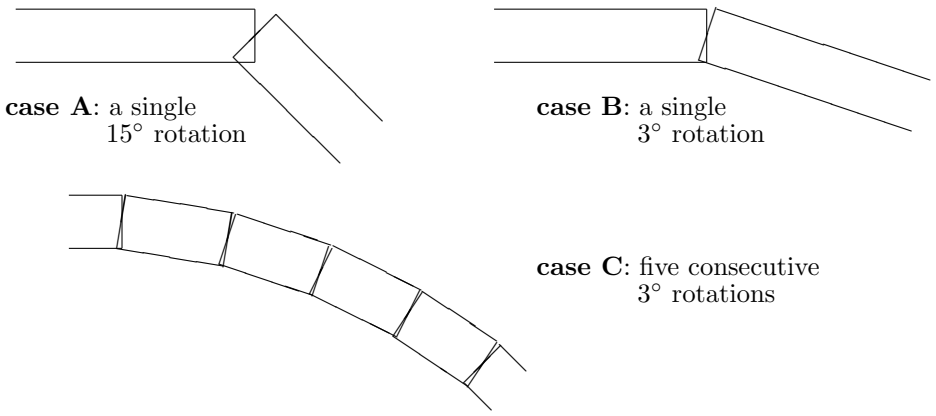

Figure 3.20: Curve segmentation for the three examples of tunnel curve

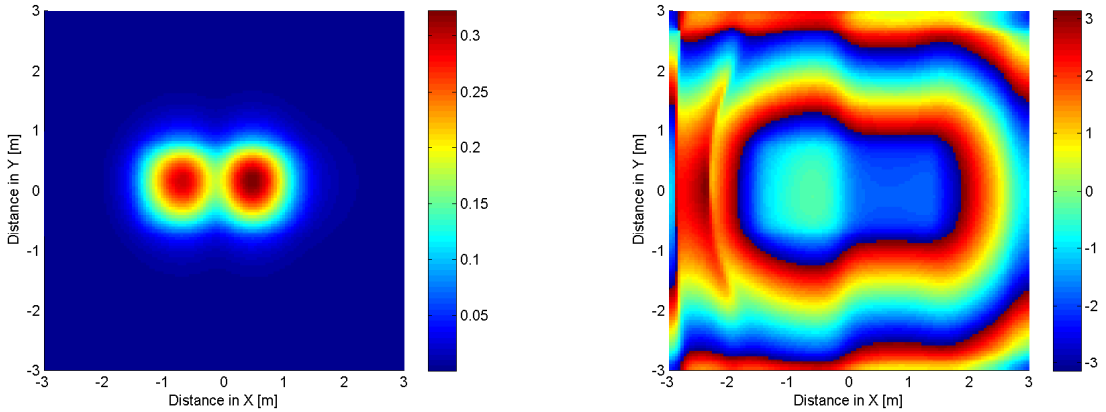

(a) Modulus of the field distribution

(b) Phase of the field distribution

Figure 3.21: Field distribution previous rotation.

the centre of the spectrum and nearby components are related to slow-variating fields that propagate along the z-axis, while the border of the *Visible* represent the components that bounce back-and-forth between the tunnel walls and thus suffer faster variations. The larger the applied rotation, the farthest the central spectral components will be shifted from the spectrum centre and the fastest the variations in the phase will be. This is the reason why the phase of the 15° rotated field presents such rapid alternances respect to the 3° rotated field, while the latter has a similar variation pattern as that of Fig.3.21b.

Finally the propagation curves for cases A,B and C are displayed in Fig.3.24. The largest path loss drop-off corresponds to case A - the 15° rotation - as expected. On the other hand, path loss curve in case B - a single 3° rotation - presents more similarities to case C - five successive 3° rotations. Note the different behaviour between cases A and C, where the curve has been modelled differently. Summarising, in case A a significant part of the spectral content has been placed in the *Evanescent* region, thus reducing the amount of contributing terms to the propagation and originating a significant drop-off in the signal strength, while in case C the wavefront has been guided through the tunnel more successfully.

These results are consistent with the modal analysis made by Mahmoud [15] and Dudley et al. [16]: the smaller the tunnel curvature radius, the larger the losses affecting propagation. Measurements carried over

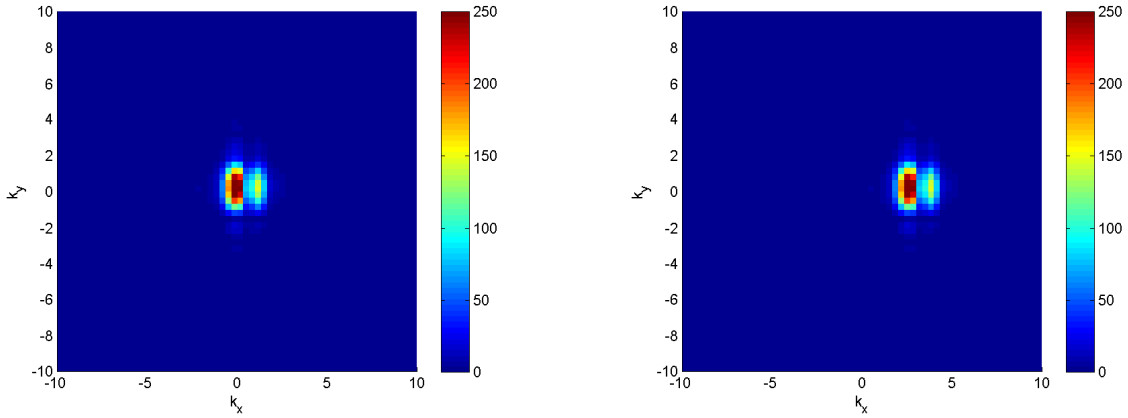

(a) $|APWS|$ for $\theta = 0°$ (b) $|APWS|$ for $\theta = 15°$

Figure 3.22: APWS modulus before and after rotation. Case A.

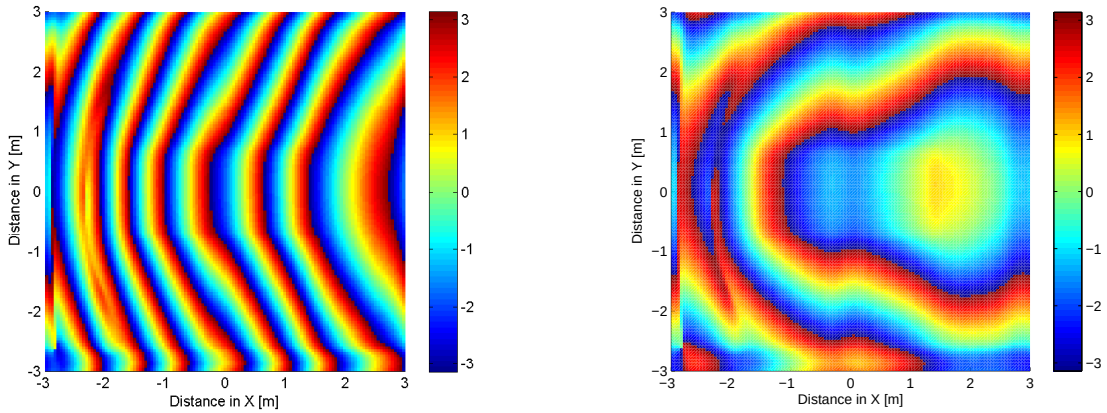

(a) case A: 15° rotation (b) case B: 3° rotation

Figure 3.23: Phase of the field distribution after rotation.

by Choi [17], as well as ray-tracing based studies conducted by Wang and Yang [18] confirms this point: Choi [17] found a larger path loss exponent factor for its regression curve model when the radius of curvature was $r = 245m$ than for the $r = 500m$ case, whereas Wang and Yang [18] showed that the level of received power along a curved tunnel decreased as the radius of curvature increased for $r = \infty, 150, 300m$. In our case, instead of curvature radius, the used parameters for tunnel bending are the axis rotation angle, number of sections and length of this sections. The results of Fig.3.24 are encouraging: larger rotation angles - associated to small curvature radius - leads to larger losses/higher attenuation.

Another aspect of propagation in curved tunnels that has been contrasted with the spectral technique is the so called *whispering gallery effect* discussed by Wait [19]: Wait states that the energy of the modes propagating along a curved tunnel tends to be distributed mainly on the outer curve walls. This point was verified by Didascalou et al. [20] in their ray-tracing based simulations. The spectral technique is also used in this case: a 200m long curve is simulated, its curvature radius being $r = 201.4m$. An elemental dipole is

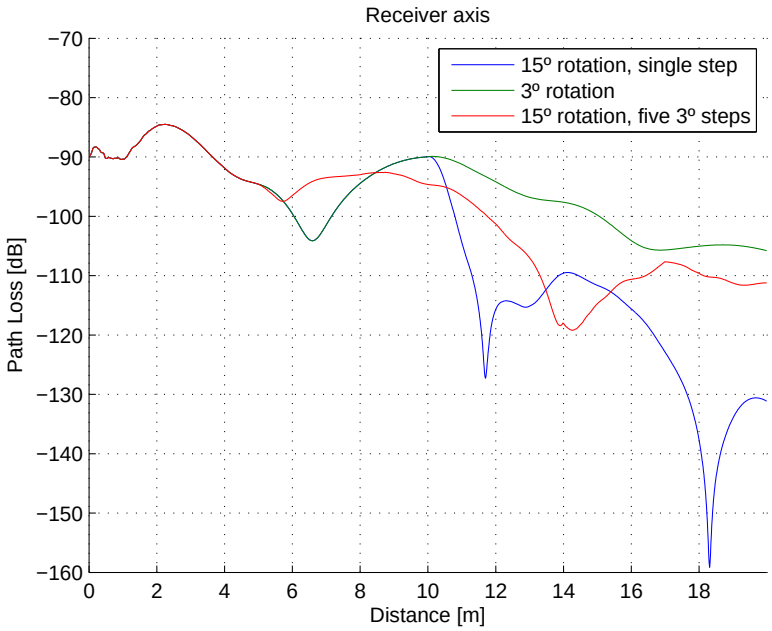

Figure 3.24: Axial path loss comparison for differently bended tunnels.

selected as a source centred in the tunnel because of its omnidirectional radiation pattern.

The effect can be appreciated in Fig.3.25, where the horizontal cut of the path loss distribution has been depicted: fields are more intense on the outer side of the curve whereas field strength is weaker on the inner side. To provide a more rigorous appreciation on this effect the tunnel is split in two halves: left, corresponding to the inner part of the curve, and right, corresponding to the outer one. The mean of the absolute field value for each part is computed longitudinally and the results are presented in Fig.3.26. See how the path losses are higher for the inner half along the curve but for the last few meters, were fields have almost extinguished. Differences between both halves would be more significant for wider tunnels and/or curves with smaller curvature radius.

3.2.4 Backscattering

There are certain situations in which changes in the tunnel cross-section implies the backscattering to be considered. As it has been noted in Section 3.2.3, the algorithm here described, due to limitations of spectral theory, can only propagate waves within an angular range of $\pm 90°$ respect to the z-axis, thus they can be considered to belong to a wavefront propagating in a *forward* direction ($+z$). For the backscattered waves to be taken into account, fields on blocking surfaces - such as the train front end - must be stored as the iterative process advances. Depending on the body electrical properties, the incident field suffers from total reflection - for PEC surfaces - or partial reflection - for any other material -, with a certain amount of the incident wave energy being transmitted through the wall.

When the wavefront reaches the tunnel end, the algorithm repeats the whole process in a *backward* direction, inverting the direction of propagation, beginning at the tunnel end back to the source plane ($-z$).

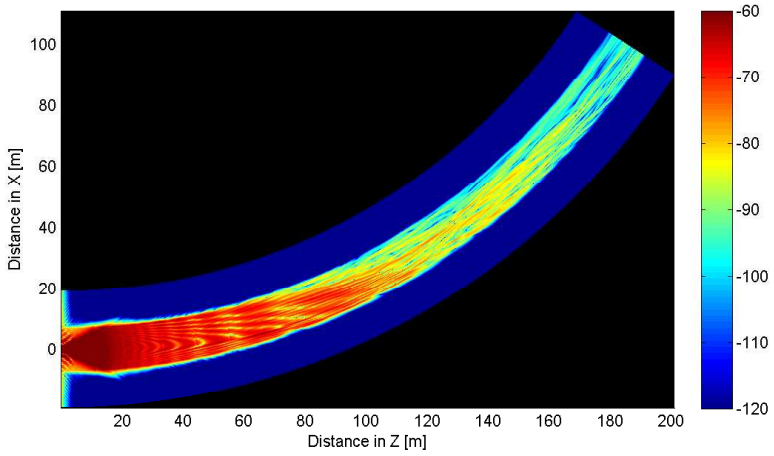

Figure 3.25: Curve simulated with the spectral technique. Horizontal cut.

Fields stored during the first pass are propagated and added to the *forward* field distribution. This process can be iterated until convergence is reached in case a complex scenario demands so, thus ensuring a correct modelling of its EM behaviour, although generally a single *forward+backward* pass is enough. As an example consider a 20m-long rectangular tunnel and two cases:

1. A partially blocked section with a 10m-long metallic carriage placed at the 4m mark on the tunnel left half, analysed only with a *forward* pass.

2. The same as above with backscattering - *forward+backward* - being taken into account.

The transmitter height is 2m in the middle right half of the tunnel, while the receiver is placed slightly above the train roof, on the inner side of the tunnel. The transversal simulation scheme can be observed in Fig.3.27, while in Figs.3.28a and 3.28b the horizontal and vertical path loss cuts at the receiver position are presented. The cuts show the field distribution only inside the tunnel. Note that the carriage structure cannot be appreciated in the horizontal cut as the receiver is placed a few centimetres over its roof, although the horizontal field distribution suggests the presence of an obstacle by diffraction at the train edges.

The main lobe is directed along the propagation axis, the wavefront is diffracted at the carriage's edges and fields are funnelled towards the empty regions of the tunnel. A shadow area appears just after the back end of the train, similarly to the results presented in Section 3.2.2. When the backscattering is added, results are those of Figs.3.29. Because there is just one obstacle, no other fields were stored in the *forward* pass and the shadow area is unmodified. Differences are noticeable between the source plane and the train front end. A comparison between both vertical cuts helps to assess the importance of the backscattering: instead of the smooth distribution corresponding to the first case, one can expect an EM behaviour similar to the second one in a more realistic scenario, where the signal may suffer of deep fading depending on the receiver's position.

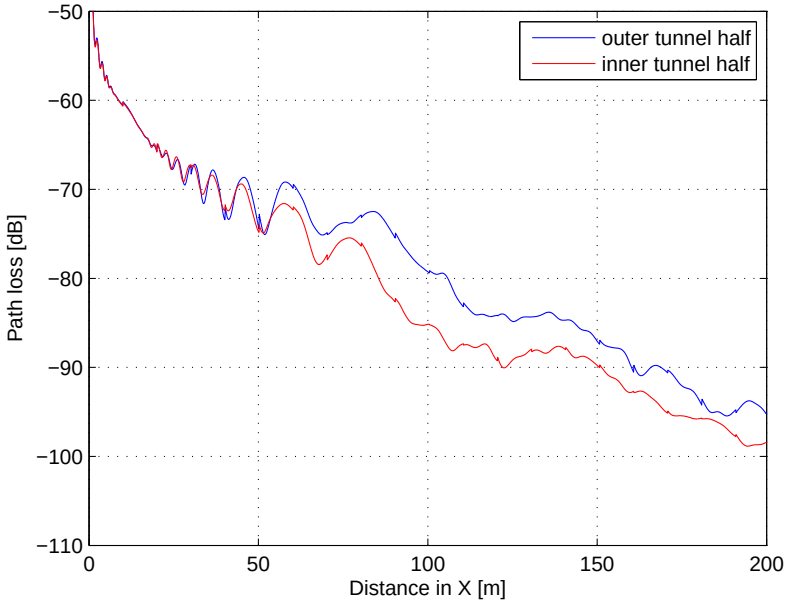

Figure 3.26: Mean axial path loss values for the inner and outer halves of the tunnel.

3.3 Boundary Conditions in Spectral Propagation

3.3.1 Scalar Approach

It has previously been seen that this version of spectral propagation is based on the use of the free space GF when computing the field distribution between consecutive longitudinal points. The use of such GF, however, is incorrect as long as propagation in bounded regions is studied: fields at the boundary and outside the tunnel cavity must be appropriately modified. A first approach is adjusting the propagation constant at the points where fields propagate in a different medium. At those points, fields should extinguish faster. The scalar profile of this Boundary Condition (BC) lies on the fact that orientation of fields is not considered, so

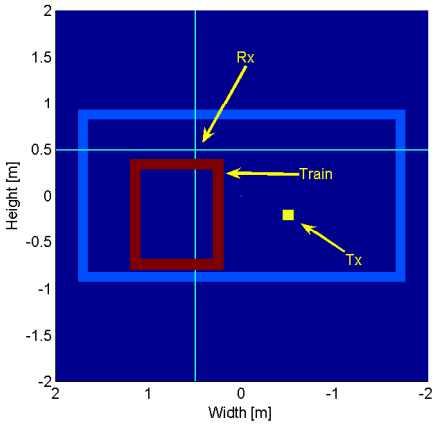

Figure 3.27: Transversal cross-section for the backscattering example.

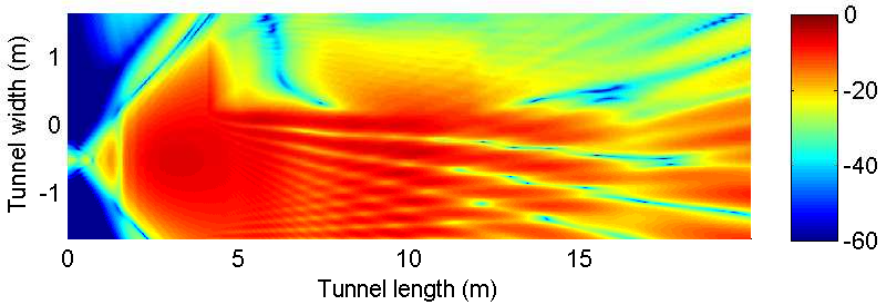

(a) Horizontal cut

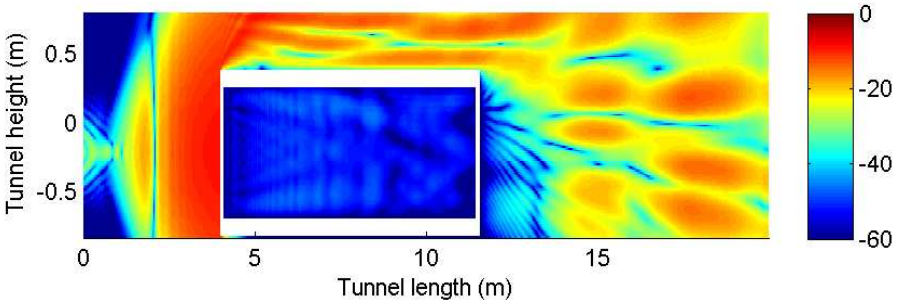

(b) Vertical cut

Figure 3.28: Path loss distribution without backscattering.

no discrimination is done: whether the field impinges parallel or orthogonally to the medium interface, the field amplitude must be reduced.

Given the dielectric constant ϵ_r and conductivity σ of the medium bounding the tunnel, the widely known expressions for the complex dielectric constant ϵ_{rc}, loss tangent $\tan\delta$ and attenuation α can be used:

$$\epsilon_{rc} = \epsilon' - j\epsilon'' = \epsilon_r - j\frac{\sigma}{\omega\epsilon_0} \tag{3.24}$$

$$\tan\delta = \frac{\Im(\epsilon_{rc})}{\Re(\epsilon_{rc})} = \frac{\epsilon''}{\epsilon'} \tag{3.25}$$

$$\alpha = \omega\sqrt{\frac{1}{2}\frac{\mu\epsilon'}{\sqrt{1+\tan^2\delta}-1}} \tag{3.26}$$

with ω being the angular frequency. This approach induces discontinuities in the field distribution at the boundaries, not complying Maxwell's equations, because the field solution is not continuous. In the long term, however, the enforced solution converges quite smoothly at the boundaries except for curves or changes in the cross-section.

This approach relies on the knowledge of the exact values of the tunnel wall parameters, which may vary as a function of humidity for instance. Fig.3.30 offers a comparison between the longitudinal path losses of the same scenario with several values for the dielectric constant and conductivity. A free space behaviour is expected for path losses in the area near the transmitter, as the wavefront initially expands in an unbounded medium. When reaching the tunnel walls, reflections occur and part of the energy is redirected towards the tunnel inside inducing interferences on the field distribution. At that point, the free space assumption

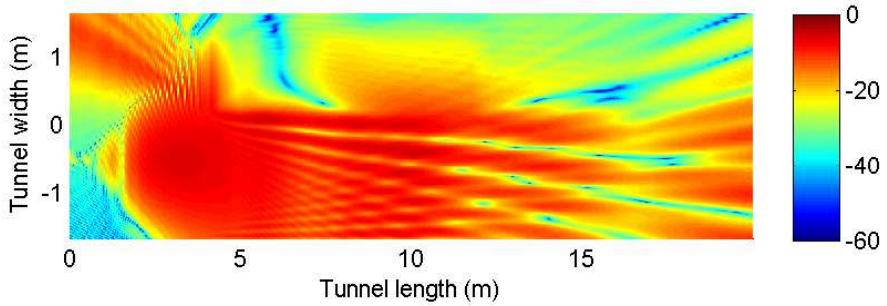

(a) Horizontal cut

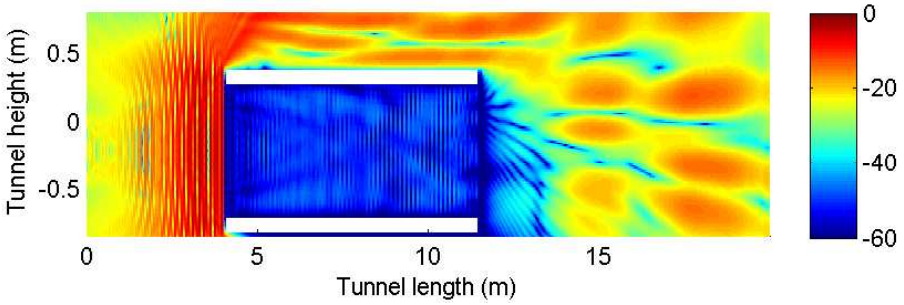

(b) Vertical cut

Figure 3.29: Path loss distribution with backscattering.

is no longer valid and the tunnel becomes a multipath environment. See an example of such in the first 20-30 meters of Fig.3.30: curves clearly follow the behaviour of the free-space path loss, but are altered by successive peaks and valleys. In this figure the same rectangular tunnel has been simulated varying the values of the material properties. Differences are small for the different ϵ_r proposed values while the impact of σ is significant. As Glaser and Emslie found in their works [21],[22], the contribution of the conductivity to the propagation loss was small. In this case it can be seen how the increase on the σ value leads to weaker bouncing but not to significant larger losses. Here, the real part of the dielectric constant dominates the attenuation, while the imaginary part - governed by the conductivity - has much less influence on it. As a conclusion, it can be said that the impact of tunnel electrical parameters variability is small in narrowband analysis carried out throughout this work.

The first results obtained with the scalar approach showed that losses inside the tunnel were not properly predicted. Zhang [23] proposed a model to calculate losses corresponding to a rectangular tunnel as a function of frequency, electrical properties of the walls, tunnel dimensions and antenna coupling. A first solution was adding this losses to the iterative propagation. Results improved significantly and made sense but, in our case, a different approach was taken. The idea is to apply different attenuation values as a function of the number of reflections that a given spectral component suffers every incremental step Δz. Hence, this attenuation mask must be applied in the spectral domain.

Equivalent tunnels have been used in similar contexts [23],[16],[24] to study EM propagation before. Here

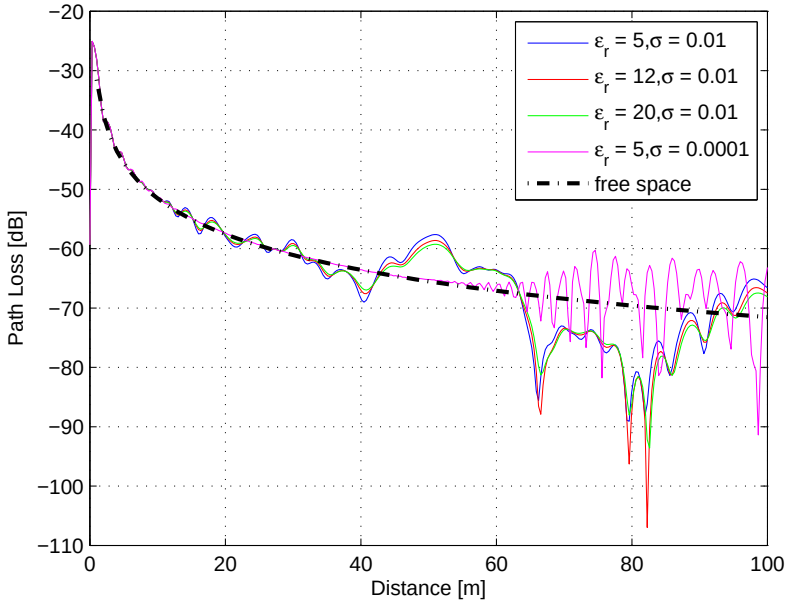

Figure 3.30: Path loss comparison for different tunnel materials.

an equivalent circular tunnel with cross-sectional area equal to the tunnel being analyzed is first computed and its radius r_{eq} derived. As it can be deduced from Fig.3.31, the distance between consecutive reflections L_i for a given plane wave i is:

$$L_i = \frac{2r_{eq}}{\tan\theta_i} \tag{3.27}$$

The number of reflections suffered by that same plane wave every incremental step Δz is:

$$n_i = n(k_x, k_y) = \frac{\Delta z}{L_i} \tag{3.28}$$

Because Δz is defined as a fraction of wavelength $n_i \ll 1$. The attenuation ρ suffered by a plane wave impinging at the tunnel walls is distributed along the $\frac{1}{n_i}$ propagation steps that same plane wave needs to reach the next reflection point. The attenuation mask can thus be expressed as:

$$\Gamma(kx, ky) = \rho^{n_i} = \rho^{\frac{\Delta z}{L_i}} = \rho^{\frac{\tan\theta_i}{2r_{eq}}\Delta z} \tag{3.29}$$

with ρ the value of the reflection coefficient. This value can be empirically measured and its electrical properties derived as detailed by Roqueta in [25]. In a simplified approach, ρ is assumed constant for all incidence angles. Fig.3.32a shows a 3D view of the attenuation mask and Fig.3.32b a cut at $k_y = 0$, centred around the visible region, for different ρ values.

As it can be seen, the smaller the value of ρ, the more selective the mask is. This can be interpreted considering that low values of the reflection coefficient imply larger amount of energy transmitted through the medium interface, where the attenuation constant is higher. Waves propagating with large θ_i angles are more attenuated inside the tunnel than those who propagate parallel to the tunnel axis because of reflections. This behaviour agrees with the fact that, at large distances, main contributions to tunnel propagation come from the direct components.

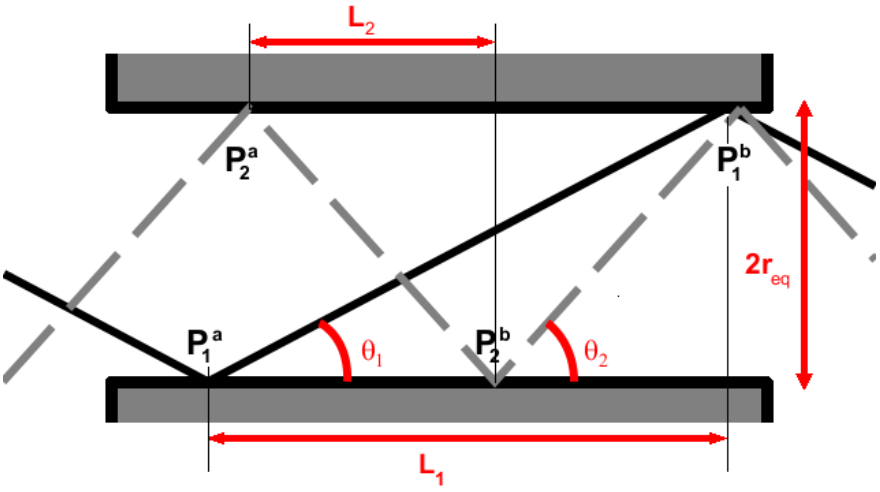

Figure 3.31: Example of the paths followed by two plane waves propagating with different angles.

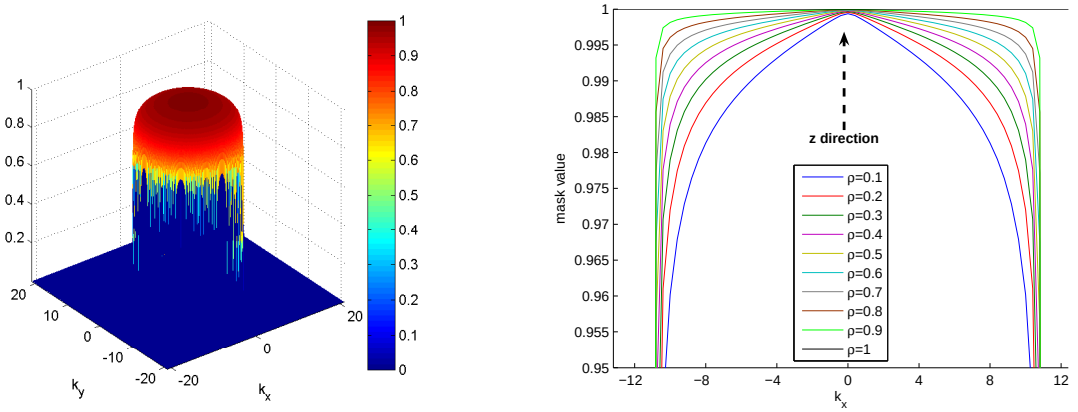

(a) 3D view of the attenuation mask

(b) Cut of the attenuation mask as a function of ρ

Figure 3.32: Attenuation mask Γ in the spectral domain.

In Fig. 3.33 the same tunnel has been simulated for three different ρ values. The aforementioned behaviour can be appreciated: the larger the ρ the more the fields are confined inside the tunnel and larger the signal level far from the transmitter. This allows for the simulator to be adjusted to experimental data in real scenarios.

3.3.2 Vector Approach

This approach was developed to undertake a more complete analysis of EM propagation. It is well-known the different behaviour of fields as a function of polarisation. Another reason that led to the implementation of a fully-polarised simulator was the need to examine the advantages of diversity and Multiple Input Multiple Output (MIMO) schemes. This techniques permit increasing the signal bandwidth.

The vectorial case implies computing the field distribution for both transversal components of the field, E_x and E_y, that are directed along the x and y axis. The number of performed operations doubles that of

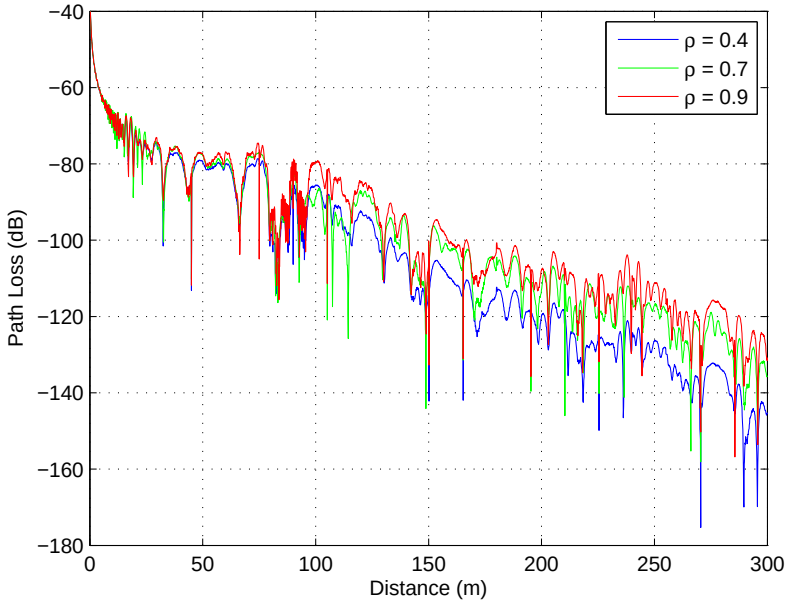

Figure 3.33: Path Loss as a function of the reflection coefficient ρ.

the scalar approach at each longitudinal step. The main difference, though, is the application of Boundary Conditions (BC), that becomes way more complex to implement due to the cross-polarisation effects between E_x and E_y field components. In a polarised scenario with medium interface, reflected and transmitted fields depend on incidence angle - which is a function of the wave propagation angle θ, the surface normal vector direction $\hat{n}$ - and wave polarisation. In the scalar approach, fields transmitted to the second medium were just attenuated according to the second medium propagation constant. In the vectorial approach, however, a more sophisticated course must be adopted.

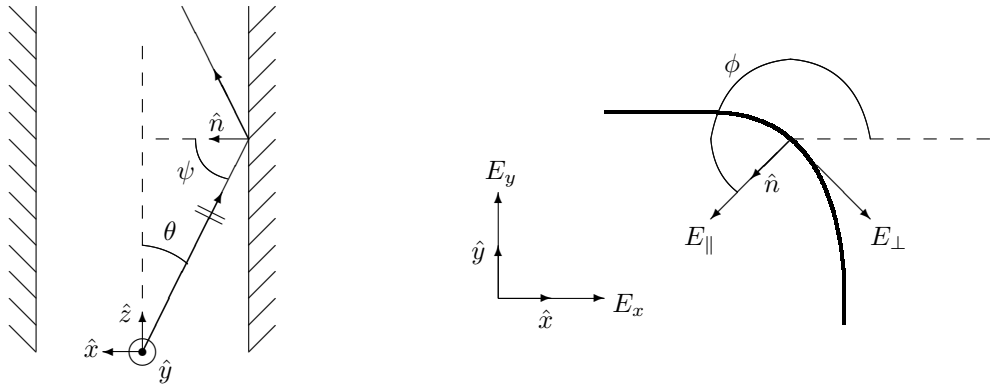

(a) Tunnel longitudinal view.

(b) Tunnel transversal view.

Figure 3.34: Angular description in vectorial approach.

A logical solution would be applying the parallel $\Gamma_\parallel$ and perpendicular $\Gamma_\perp$ reflection coefficients along the boundary but, although the APWS provides angular information on the progressing wavefront, it does not facilitate the angle of incidence locally, which is needed to compute $\Gamma_\parallel$ and $\Gamma_\perp$. Plane waves do not

impinge at a single point, but rather at every point belonging to the boundary. A set of waves with different propagation angles impinge at each one of these points. Application of $\Gamma_{\parallel}$ and $\Gamma_{\perp}$ for each plane wave composing the wavefront is not possible at every boundary point. A different solution is chosen and the following assumption is made: the angle of incidence ψ is set to $\psi = \pi/2$. It is widely accepted that the leading components in tunnel propagation are those whose propagation angles θ are small - so $\theta \approx 0$ - because they do not suffer attenuation due to reflections at the tunnel walls. Because of the relation between incidence and propagation angles - $\psi + \theta = \pi/2$ for tunnels with smooth walls as Fig.3.34 shows - the value of ψ at large distances is found to be the abovementioned $\psi = \pi/2$. It can be argued that this does not hold in multipath environments, where several reflections occur due to the different paths existing between two points - each associated with a θ angle - causing fadings and other phenomena. Hence, inaccuracies are to be expected in the region close to the transmitter, where strong multipath happens. Nevertheless, this assumption should be valid to determine whether the spectral technique is able to accurately predict path losses in the far field region. The parabolic approach described in Chapter 5 is based in a similar assumption.

To see how this approach worked suppose a tunnel whose cross-section is constant along the propagation axis, so the normal surface vectors are found along the interface. The wavefront passes down the tunnel and fields are decomposed into $E_{\parallel}$ and $E_{\perp}$ components from the known E_x and E_y distributions. The corresponding $\Gamma_{\parallel}$ and $\Gamma_{\perp}$ reflection coefficients are applied and finally the change of base is undone to retrieve the E_x and E_y values at the boundary. Thus, starting with the widely known expressions for reflection coefficients $\Gamma_{\parallel}$ and $\Gamma_{\perp}$ [2]:

$$\Gamma_{\parallel} = \frac{-n_2^2 \cos\psi + n_1\sqrt{n_2^2 - n_1^2 \sin^2\psi}}{n_2^2 \cos\psi + n_1\sqrt{n_2^2 - n_1^2 \sin^2\psi}} \tag{3.30}$$

$$\Gamma_{\perp} = \frac{n_1 \cos\psi - \sqrt{n_2^2 - n_1^2 \sin^2\psi}}{n_1 \cos\psi + \sqrt{n_2^2 - n_1^2 \sin^2\psi}} \tag{3.31}$$

If the $\psi = 0$ value is substituted, the previous equations can be rewritten as:

$$\Gamma_{\parallel}\big|_{\psi=0} = 1 \tag{3.32}$$

$$\Gamma_{\perp}\big|_{\psi=0} = -1 \tag{3.33}$$

where the angular dependency has been eliminated, nor does the wall material have an impact over the propagation outcome due to the grazing incidence of waves. A straight rectangular tunnel was simulated - its width doubling its height - with a source polarised horizontally (Hpol) or vertically (Vpol). The attenuation corresponding to the dominant mode for both polarisations was first found by Emslie et al. [22], but more recently Mahmoud [15] offered a simplified expression. These values are compared to those obtained from simulations at large distances from the source, where almost all contributions from higher order modes vanish. The numerical values are presented in Table 3.2, while Fig.3.35 shows the different behaviour for both polarisation cases.

Simulations results agree quite well with theoretical values in the horizontal case. The worst case difference is around $1dB/100m$ for the vertical polarisation, which is something to be taken into account.

	$H_{pol}[dB/100m]$	$V_{pol}[dB/100m]$
Modal Theory	1.5974	7.7472
Simulations	1.53	8.7037

Table 3.2: Attenuation values for rectangular tunnel.

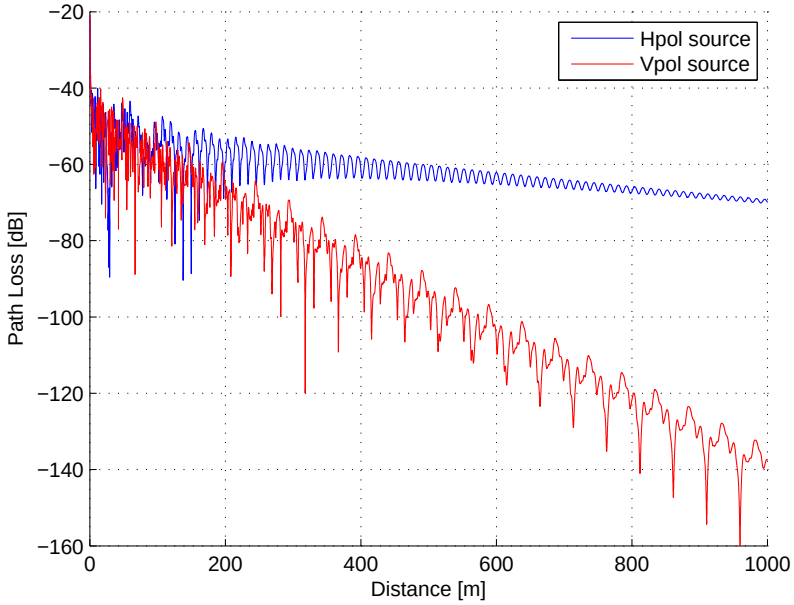

Figure 3.35: Rectangular tunnel simulated with different source polarisation.

However, considering that real cases will be limited to distances up to $1km$, and that attenuation masks can be adjusted to better fit experimental results, this difference will be expected to diminish. Therefore, the case can be made that this technique is suited to model EM propagation in tunnels. This chapter has been devoted to give a qualitative insight on the different situations that can be presented in such scenario. Several examples have been used to illustrate the cases, although results have been discussed mainly from a conceptual point of view. Next chapter is focused on the comparison between experimental data and simulation results for validation purposes.

Chapter 4

Simulation Results and Validation: Spectral Approach

The previous chapter was devoted to give a general overview on the possibilities of spectral propagation. Several aspects of this technique were discussed using examples but no results in real tunnel environments were provided yet. The aim of this chapter is, thus, offering a clear understanding of the spectral-based simulator performance and its limitations. For this purpose, several published results have been used as a reference.

One of the most spread techniques for EM prediction in tunnels is the ray optical approach, that has been used with good results lately [26],[27],[18], [20],[28],[29], although it was already being used in the mid-70's [30],[22]. The advantage of ray-tracing methods is their straightforward implementation and that they provide results, particularly in some cases [20], with excellent accuracy. They are specially suited for complex scenarios because scatterers and variations in the tunnel cross-section can be modelled with a high degree of precision. Results for the multipath region close to the transmitter are usually in very good agreement with experimental data.

However, taking into account such details is not an easy task and is subject to modelling errors, causing inaccuracies. For this reason it is of major interest contrasting results in the far-field region of the antenna, where only main contributions remain in the propagation terms and the impact of boundary surface irregularities is negligible. From a geometrical optics point of view, only rays propagating parallel to the tunnel axis survive in this region, as they have not suffered attenuation due to reflections at the tunnel walls. The same can be said when working with plane waves instead. Modal theory, first developed in [31],[32],[33],[22],[34] is a better choice to model EM issues at this stage of the propagation. There have recently been more contributions dealing with this approach in rectangular, arched and circular tunnels [15],[24],[35],[14].

Simulations with the spectral technique were conducted trying to reproduce with the maximum fidelity the scenarios depicted in the different publications. The references in this section were chosen so that all the needed parameters were specified.

4.1 Rectangular Tunnels

A set of measurements were carried out in the Berlin subway by Didascalou et al. [20] at both GSM bands - $f_1 = 945MHz$ and $f_2 = 1853MHz$ - in a straight rectangular tunnel, and their results were compared with ray-tracing based simulations [36]. The set of measurement parameters are displayed in Table 4.1. The scalar spectral approach was here used first to see how the simulator behave.

Frequency		$f_1 = 945MHz$	$f_2 = 1853MHz$
Tunnel dimensions	Width	$W = 3.8m$	
	Height	$H = 4.3m$	
	Length	$L = 110m$	
Electrical parameters	Dielectric constant	$\epsilon_r = 5$	
	Conductivity	$\sigma = 0.0053S/m$	$\sigma = 0.0103S/m$
Transmitter(Tx)	Polarisation	Vertical	
	Horizontal position	$x_{Tx1} = 0.88m$ left	$x_{Tx2} = 0.04m$ right
	Vertical position	$y_{Tx1} = 2.82m$	$y_{Tx2} = 2.2m$
Receiver(Rx)	Antenna	$\lambda/4$ monopoles	
	Polarisation	Vertical	
	Horizontal position	aligned with Tx	
	Vertical position	$y_{Rx} = 1.47m$	

Table 4.1: Measurement parameters in Berlin subway by Didascalou [20].

Didascalou presented the curves of Fig.4.1a, while results from spectral simulations are displayed in Fig.4.1b,c,d. Vertical axis correspond to path losses that, in simulations, have been adjusted to match free space losses at $f_1 = 945MHz$ close to the transmitter. This criteria will be used from now on using the corresponding frequency when displaying path loss values. Didascalou uses another criteria to adjust the vertical axis, that is the reason why their range of values along this dimension differ. Notwithstanding, the vertical span is the same.

The comparison with the scalar BC approach of Fig.4.1b shows that the spectral technique, after an initial larger fall-off close to the transmitter, obtains a similar behaviour from that point on, and that is closer to measurements than to ray-tracing simulations. If vector BC Figs.4.1c,4.1d are applied, results change substantially. Two uniform meshes with $\Delta = \lambda/4$ and $\Delta = \lambda/10$ are used. For the former, the simulator output does not resemble the reference path loss. There are more similarities when the latter mesh - Fig.4.1c - is used, and convergence is practically reached when trying with finer meshes, so $\Delta = \lambda/10$ is set in order to avoid excessive simulation time and memory resources.

Note how multipath is more significant for the vectorial approach than for the scalar approach. There are many reflections in small enclosed areas close to the source, so a lot of interferences between the different propagation paths occur. From a modal point of view, high order modes have still not been severely attenuated, so there are many of them interacting with each other and causing fast fading. Comparing

Figs.4.1a and c, measurements have smaller losses in the $30m - 80m$ interval. Remember that spectral simulations are run with the propagation angle $theta = 0°$, as seen in Section 3.3.2, even if tunnel walls are not smooth. The immediate consequence of having a certain roughness at tunnel wall surface is that the incidence angle ψ varies locally. This is equivalent to allow the propagation angle to take different values depending on the surface impinging point. If a small random propagation angle is chosen, which physically has some sense, the behaviour improves. Results for this variation, with $\theta = [0° - 25°]$, are shown in Fig.4.1d, where losses in the central interval have decreased respect to the $\theta = 0°$ case.

Even if simulation predictions disagree locally at certain points, mainly on the apparition and position of certain peaks and valleys, path loss have similar levels along the tunnel. Comparing measurements in Fig.4.1a and simulations in Fig.4.1d, the first $40m$ are quite alike. From that point on, spectral simulations keep a closer behaviour to ray-tracing simulations in terms of bouncing and positions of peaks and valleys.

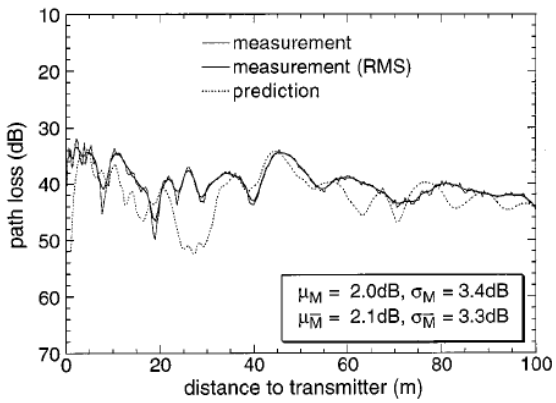

(a) Measurement results taken from [20], Fig.4a.

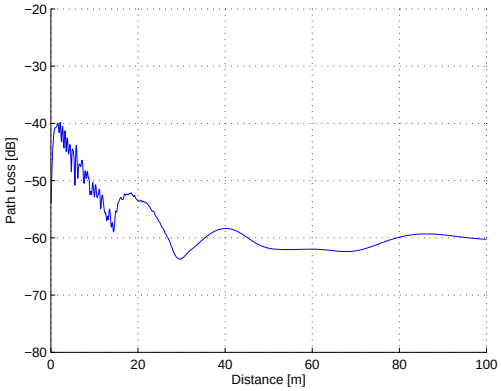

(b) Simulation results. Scalar approach.

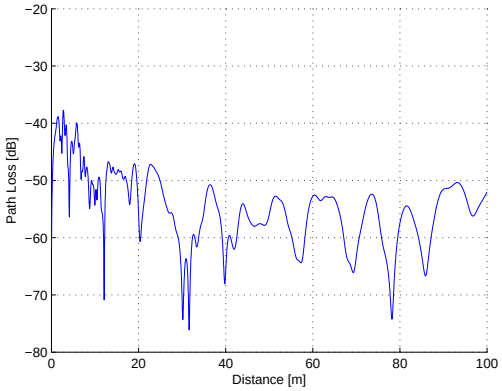

(c) Simulation results. Vector approach. $\Delta = \lambda/10$, $\theta = 0°$.

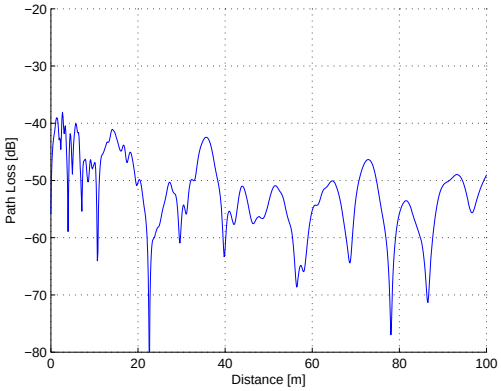

(d) Simulation results. Vector approach. $\Delta = \lambda/10$, $\theta = (0° - 25°)$.

Figure 4.1: Path loss comparison at $f_1 = 945MHz$ in Berlin subway.

As for the $f_2 = 1853MHz$ experiment, larger losses were obtained as expected. Measurements can be found in Fig.4.2a and scalar simulations in Fig.4.2b. Even if fall-off close to transmitter is larger in simulations and position of significant fadings is not equal, both have similarities. When the vector BC are

applied, multipath is quite stronger. Figs.4.2c and 4.2d show the predictions for $\Delta = \lambda/10$ with $\theta = 0°$ and $\theta = [0° - 25°]$ respectively. As before, finer meshes did not modify substantially the results so the $\Delta = \lambda/10$ value is selected again. In this case, though, it is clear that the scalar approach offers better matching with measurements, and that the vector approach fails notoriously.

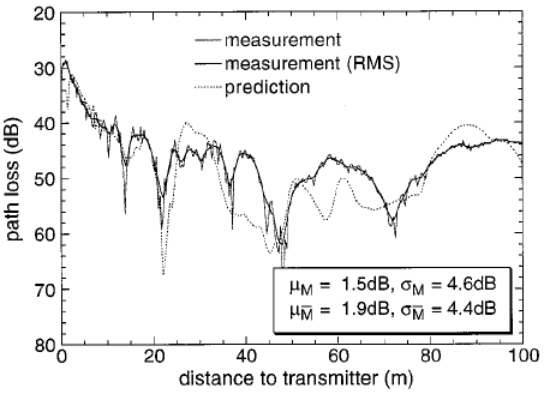

(a) Measurement results taken from [20], Fig.4b.

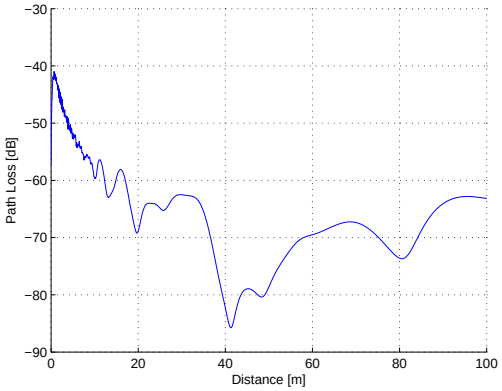

(b) Simulation results. Scalar approach.

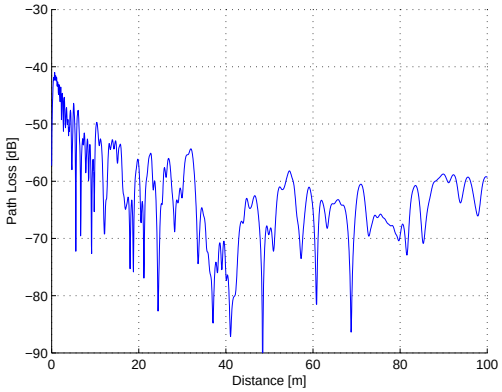

(c) Simulation results. Vector approach. $\Delta = \lambda/10$, $\theta = 0°$.

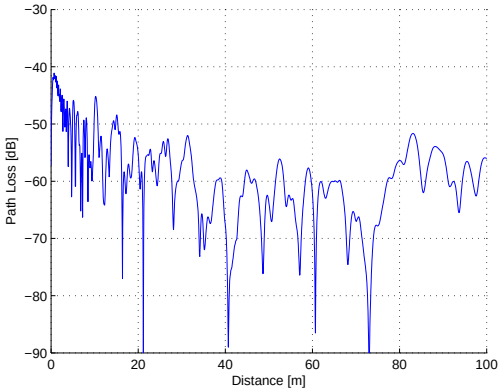

(d) Simulation results. Vector approach. $\Delta = \lambda/10$, $\theta = (0° - 25°)$.

Figure 4.2: Simulations at $f_2 = 1853MHz$ in Berlin subway. Vector approach.

The underlying reason may be that Didascalou measurements were taken every $18cm$ [20], that corresponds approximately to a full wavelength for f_2. Simulations of Figs.4.1,4.2 used a longitudinal step ten and twenty times smaller. If the longitudinal sampling is set to $\Delta z = \lambda$ the results improve significantly, as shown in Figs.4.3,4.4. The original data is plotted again to ease the comparison.

To conclude this first set of experiments, it seems that the spectral technique is a good fit to predict path losses in rectangular tunnels at short distances from the source. Although simulations and measurements do not match exactly, the reason can be attributed in both cases to imprecisions in the scenario modelling and to the inexact nature of the chosen propagation technique. Hereafter, the results from spectral propagation are obtained using the vector BC approach.

Other measurements conducted by Lienard [16] are also used as a reference to complete the study of

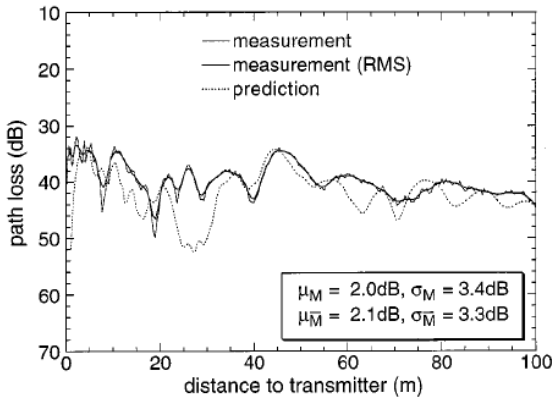

(a) Measurement results taken from [20], Fig.4a

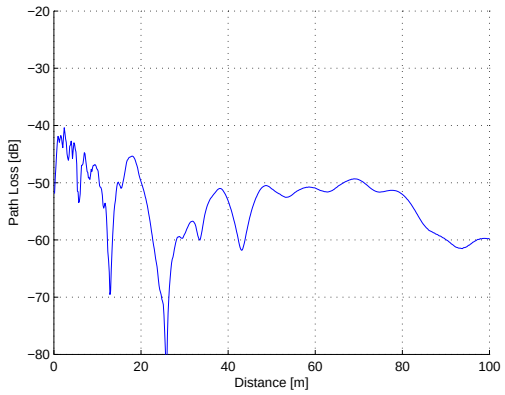

(b) Simulation results. Vector approach. $\Delta_x = \Delta_y = \lambda/10$, $\Delta_z = \lambda$, $\theta = (0° - 25°)$.

Figure 4.3: Simulation at $f_1 = 945MHz$ in Berlin subway. Vector approach, non-uniform mesh.

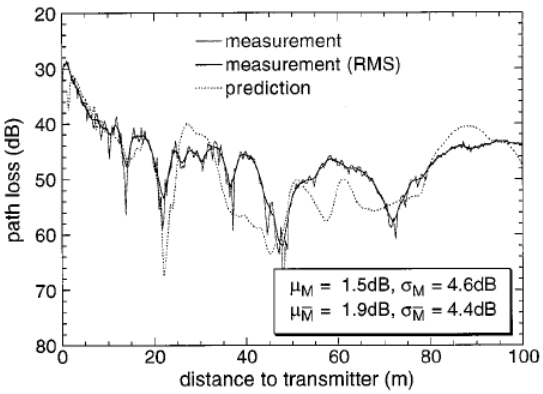

(a) Measurement results taken from [20], Fig.4b

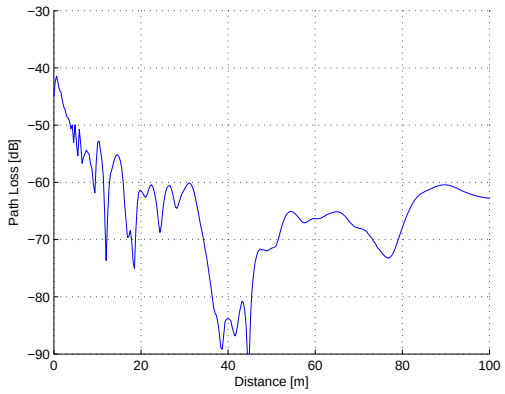

(b) Simulation results. Vector approach. $\Delta_x = \Delta_y = \lambda/10$, $\Delta_z = \lambda$, $\theta = (0° - 25°)$.

Figure 4.4: Simulation at $f_2 = 1853MHz$ in Berlin subway. Vector approach, non-uniform mesh.

propagation in rectangular tunnels. In this case the focus lies at large distances from the transmitter, in the order of a few kilometres. Even though the tunnel cross-section is semi-arched, in [37] Sun and Cheng describe a procedure allowing the use of an equivalent rectangular tunnel when studying the propagation characteristics in arched tunnels. This procedure is adopted by Lienard to develop a modal analysis with excellent results. Experiments were carried out in a straight 2500m-long tunnel at $f_1 = 450MHz$ and $f_2 = 900MHz$. The length of the stretch allows a modal analysis of the propagation because at such long distances only the lower modes, that are the less attenuated, survive and contribute to propagation, thus permitting a better comprehension of the EM phenomena in the tunnel. The parameters to setup the simulations - taken from [16] - are summarised in Table 4.2.

The experimental data from Lienard is showed in Fig.4.5a, while results from spectral simulations are presented in Fig.4.5b. In her paper, Lienard identifies the measured pattern at both frequencies with the interference between the first two vertically-polarised hybrid modes, HE_{11}^y and HE_{21}^y. When comparing

Frequency		$f_1 = 450MHz$ | $f_2 = 900MHz$
Tunnel dimensions	Width	$W = 7.8m$
	Height	$H = 5.3m$
	Length	$L = 2500m$
Electrical parameters	Dielectric constant	$\epsilon_r = 5$
	Conductivity	$\sigma = 0.01S/m$
Transmitter(Tx) and Receiver(Rx)	Polarisation	Vertical (VV)
	Horizontal position	$x_0 = 1.95m$
	Vertical position	$y_0 = 2m$

Table 4.2: Measurement parameters in Massif Central tunnel by Lienard [16].

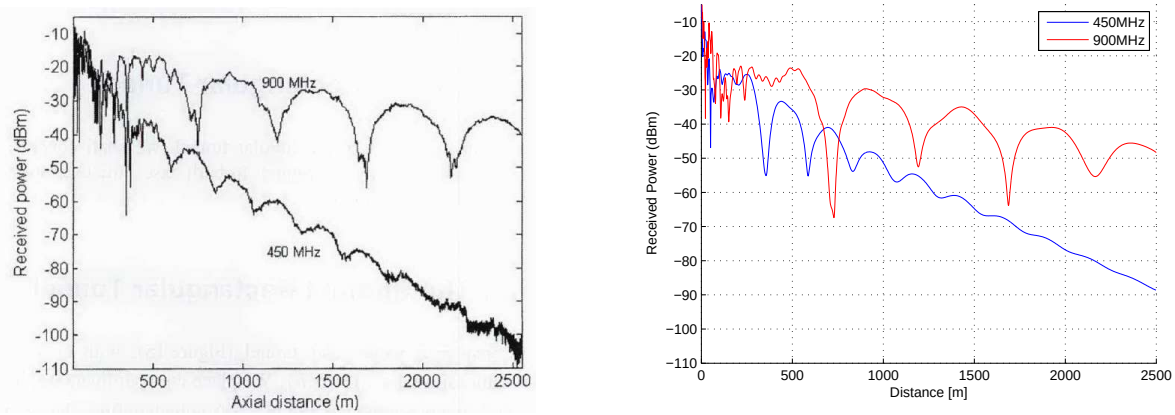

(a) Measurement results taken from [16], Fig.18.

(b) Simulation results.

Figure 4.5: Polarimetric results at 450MHz and 900MHz.

measurements with simulations, very good agreement is reached at $f_2 = 900MHz$ while, even though the path loss pattern is similar to the measured one, differences at $f_1 = 450MHz$ are notable - around $10dB/km$ - in terms of slope. Table 4.3 gathers the attenuation and pseudo-periodicities values for both measurements and simulations.

All in all, the reasons after the incorrect behaviour of the propagation predictions are due to different reasons. For the first analysed set of measurements, where the focus was on the short-range propagation, it is clear that environment error modelling plays an important role in the results inaccuracy. However, this is not the case for the long-range region of the second measurement set. As the scheme of Fig.3.1 shows, BC are applied after field components in the current transversal plane have been found from the APWS via IFFT. At that point the field distribution is continuous all over the spatial domain. By computing the field values along the boundaries and modifying those points, discontinuities are created and field distributions do not fulfil Maxwell's equations but, because dominant mode distributions usually have small values at the boundaries in the tunnel inner region, such an impact on the propagation conditions was not expected.

Frequency	Case	Attenuation [dB/Km]	Pseudo-periodicity [m]
450MHz	Measurements	33.0	240
	Simulations	24.1	241
900MHz	Measurements	8.5	486
	Simulations	8.7	485

Table 4.3: Parameter comparison between measurements and simulations. Rectangular tunnel.

4.2 Circular Tunnels

Perfect circular geometry is a special case of tunnel cross-section that can hardly be found in real scenarios. To the author knowledge, there are no measurements in large circular cavities, but recent works by Holloway [38] and Dudley [35],[39],[14] offer a detailed modal analysis based on exact analytical solutions of fields inside lossy circular waveguides.. This geometry is also ideal to study cross-polarisation effects induced at the tunnel walls surface. This aspect could hardly be given any consideration for the rectangular case because field components were oriented in the same directions as the tunnel walls. Hence, cross-polarisation was negligible. The circular case will also provide a better insight on the behaviour of the upper half of Barcelona L9 tunnels, whose arched profile is shown in Fig.3.11.

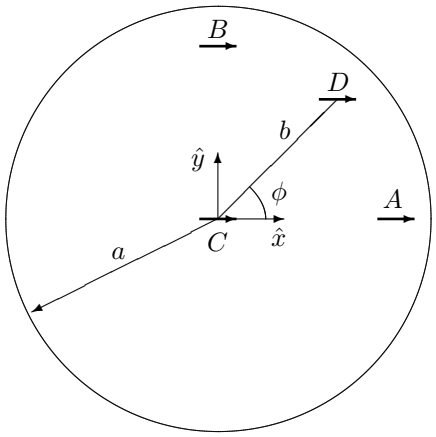

Figure 4.6: Circular tunnel and source positions.

The theoretical experiments developed by Dudley in [35] and [14] referred to the modal theory of propagation inside a straight circular tunnel. The work presented here is focused on the latter [14] - where a linear source is used as the tunnel excitation - rather than the former [35] - where a loop source is used - by two reasons: the first is that the linear source excites a richer set of modes than the ring source. Second, and related with the previous one: the ring source only excites circularly symmetric modes that are only excited by tangential currents. Because the simulator uses a cartesian grid, is hard to excite these modes because of the discrete nature of the problem, even if fine meshes are employed. The work developed by Dudley comprises the dominating modes, their attenuation and the cross-polarisation for several cases. Simulation parameters are displayed in Table 4.4.

The first experiment puts the elemental source at the tunnel centre, which corresponds to position

Frequency		$f = 1GHz$			
Tunnel dimensions	Radius	$a = 2m$			
	Length	$L = 1200m$			
Electrical parameters	Dielectric constant	$\epsilon_r = 12$			
	Conductivity	$\sigma = 0.02S/m$			
Transmitter(Tx)	Antenna	Elemental source			
	Polarisation	Horizontal			
	Position	A	B	C	D
	Radial	$b = 1.8m$	$b = 1.8m$	$b = 0m$	$b = 1.8m$
	Angular	$\phi = 0°$	$\phi = \pi/2°$	$\phi = 0°$	$\phi = \pi/4°$

Table 4.4: Simulation parameters taken from [14].

C in Fig.4.6. Only hybrid modes are allowed to propagate under these conditions. Fig.4.7 shows fields behaviour predicted by theory and simulations, while Table 4.5 gathers the attenuation of the dominant mode. Decreasing rates differ in $1dB/100m$ approximately - the same error order of the rectangular tunnel at $f_1 = 450MHz$ in the previous section - and the interference pattern lasts longer and is stronger in simulations. Faster fading predicted by theory is associated to high order modes and seems to not be present in simulations. Other than that, results agree quite well. For instance: if fast variations were filtered in the theoretical case and a bimodal interference pattern is considered, pseudo-periodicity is very much alike in both approaches. This can be easily appreciated for the $\rho = 0.5m$ traces in the $200m - 400m$ tunnel interval. On top of that, the simulator keeps the track of the theoretical behaviour in more aspects. First, the closer to the centre, the stronger the field strength is and the earlier the single-mode pattern arises. Also, the offset in dB between $\rho = 0.5m$ and $\rho = 1.8m$ receiver positions is very similar in both cases.

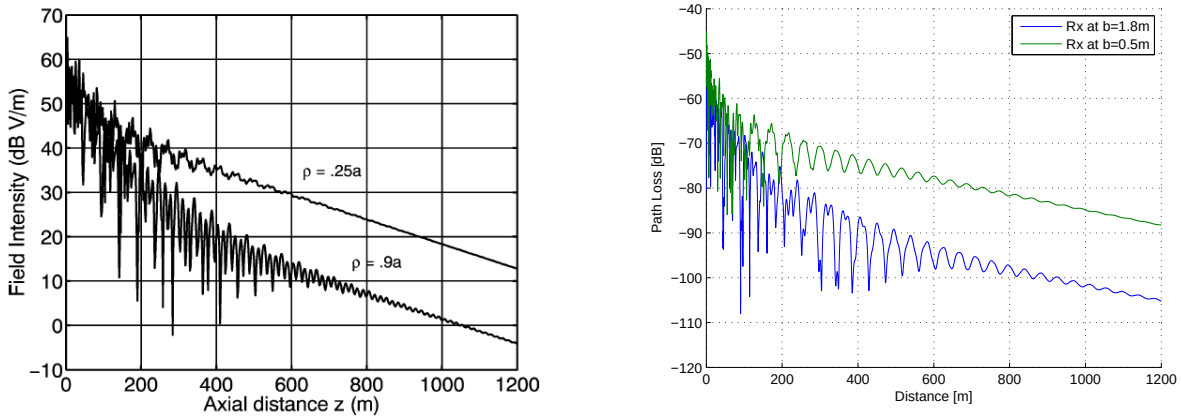

(a) Theoretical results taken from [14], Fig.8. $a = 2m$.

(b) Simulation results.

Figure 4.7: Comparison at position C for $f = 1GHz$.

Analysis of the transversal field distribution confirms that the dominating mode is the expected HE_{11} - as Fig.4.8 shows - so this indicates that propagation constants are not accurately predicted by the spectral

Theory $[dB/100m]$	Simulations $[dB/100m]$
2.78	1.72

Table 4.5: Attenuation comparison at $f = 1GHz$. Source at C position.

technique: attenuation constant for HE_{11} mode does not match with theory, while the phase constant, that is related to the small difference in the pseudo-periodicity values commented previously, diverges in a much less significant manner. The fact that the interference pattern lasts longer in simulations is also related with that: it means that the difference between the attenuation rates of the two lower order modes - HE_{11} and HE_{21} - is smaller than it should be, so the HE_{21} does not extinguish as fast as it should.

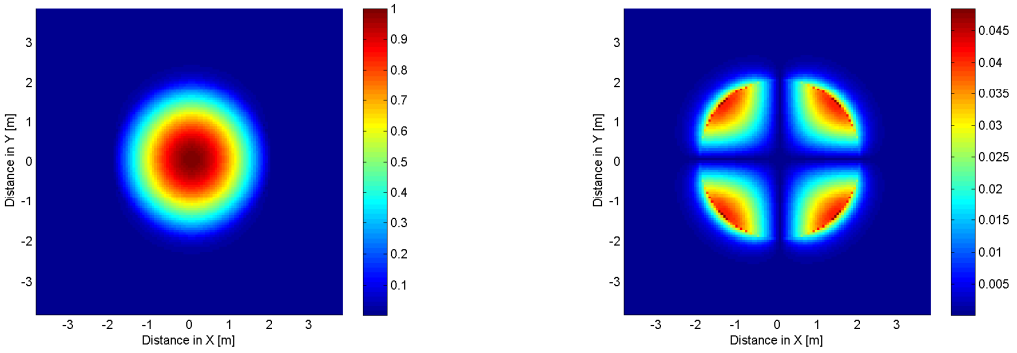

(a) $HE_{11}mode$. X component.

(b) $HE_{11}mode$. Y component.

Figure 4.8: Transversal field distribution. Source at C position.

Two more interesting experiments by Dudley consist on placing the source at positions A or B of Fig.4.6 for $b = 1.8m$. Case A does not allow for TE modes to propagate while the same happens in case B with TM modes. Hybrid HE and EH modes are allowed in both cases. Because no TE modes propagate in case A, a straight decreasing behaviour is expected to arise towards the end of the considered tunnel length, the slope corresponding to the HE_{11} attenuation value of $2.78dB/100m$. Theory and simulations can be compared in Fig.4.9.

The single-mode behaviour does not arise at the distance predicted by Dudley. However, if further distance is simulated with the spectral technique, this is reached around $1500m$ from the transmitter. Inspection of the transversal fields and attenuation leads to the same distribution obtained in case C, as expected. The fall-off is again $1.71dB/100m$ and field components are those of Fig.4.8. Nevertheless, similarities between theory and simulations in Fig.4.9 for the first $600m$ are remarkable.

Case B offers a more interesting study: there is an interference pattern because of the presence of TE_{01} and HE_{11} modes, whose attenuation values - $1.1dB/100m$ and $2.78dB/100m$ respectively - are close. In this case the slope should finally relax to that of TE_{01} mode of $1.1dB/100m$ but, because of the presence of the HE_{11} mode, Dudley says that the single mode behaviour arises later than for case A, around $2000m$. In simulations, the HE_{11} mode extinguishes at the $3000m$ mark approximately. Results are presented in Fig.4.10.

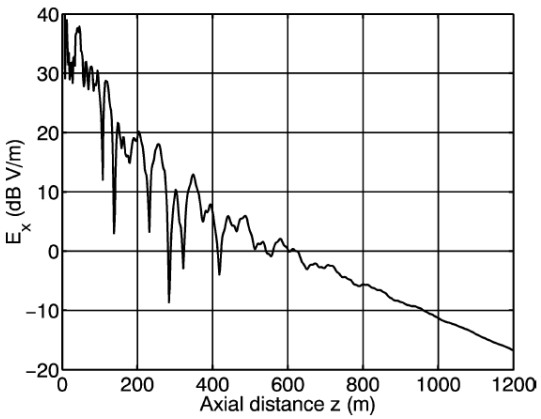

(a) Theoretical results taken from [14], Fig.11.

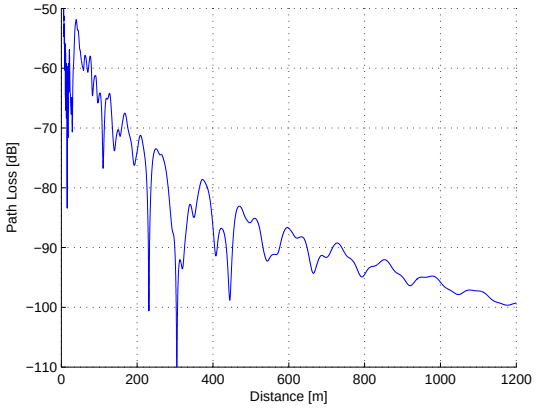

(b) Simulation results.

Figure 4.9: Comparison at position A.

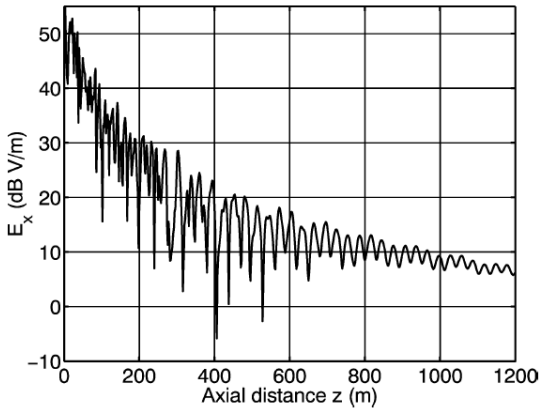

(a) Theoretical results taken from [14], Fig.12.

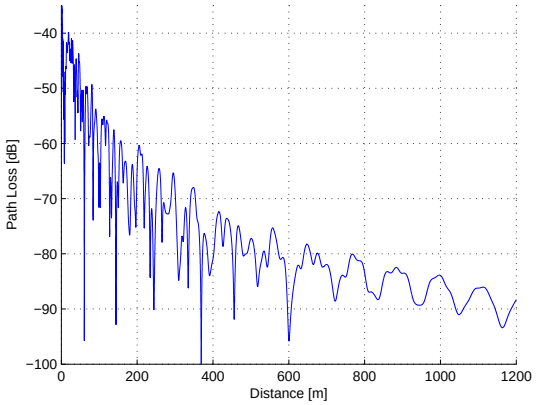

(b) Simulation results.

Figure 4.10: Comparison at position B.

In this case, the small ripple due to high order modes is missing, while the bimodal interference pattern is much stronger in simulations: note that it is rather weak in Dudley's predictions, but it exists. The bouncing pattern is due to the presence of both TE_{01} and HE_{11} modes - revealed by the study of the transversal fields - but, if the tunnel is simulated at further distances, the TE_{01} prevails, the attenuation being $1.49dB/100m$ and its distribution that of Fig.4.11.

The closeness between TE_{01} and HE_{11} modal attenuations - summarised in Table 4.6 - makes the bimodal pattern last longer in simulations. However, despite the difference between predicted and simulated attenuation values, the phase constant is quite close. Note that higher-order modes have not been excited.

In light of the results at $f = 1GHz$, it can be concluded that the spectral simulator does not make a good job of computing the propagation constants correctly: neither attenuation nor phase constants take correct values.

The last case being considered from Dudley experiments is oriented to the cross-polarisation study. To

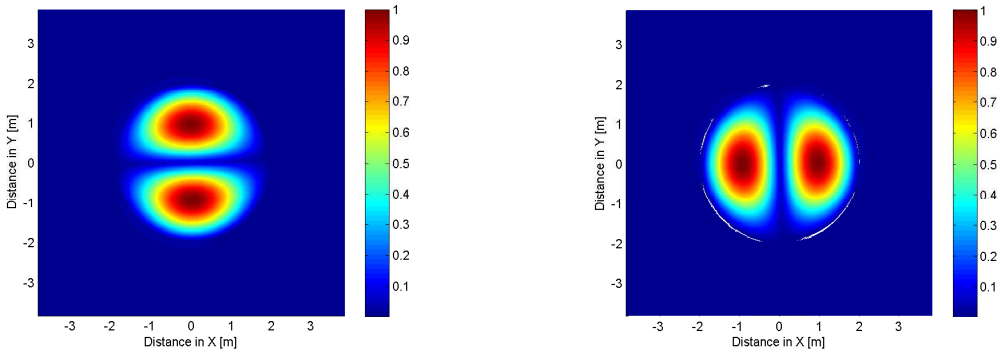

(a) $TE_{01} mode$. X component.

(b) $TE_{01} mode$. Y component.

Figure 4.11: Transversal field distribution at $L = 3000m$. Source at B position.

Case		Attenuation [dB/100m]	Pseudo-periodicity [m]
A	Theory	2.774	-
	Simulations	1.710	-
B	Theory	1.098	30
	Simulations	1.492	111

Table 4.6: Parameter comparison between measurements and simulations. Circular tunnel.

do so, the source is placed at position D in Fig.4.6. At that point the resulting fields are a combination of those attained in cases A and B but, while for those cases the cross-polar fields should theoretically vanish - in simulations, the difference between co-polar and cross-polar components for cases A and B was larger 40dB -, that does not hold in this case. Results are displayed in Fig.4.12. Again, high order modes are missing, but the theoretical pseudo-periodicity due to the lower order modes matches pretty well with the theoretical expected values. Closeness between co-polar and cross-polar components reflect the impact of cross-polarisation effect.

The same comments made for the rectangular case can be made about the performance of the simulator in the circular tunnel. On top of that, here the comparison is being made with exact analytical solutions, which should be even more difficult to reproduce with an approximated method like the one being used. The difference between theoretical and simulated propagation constants is not that large except for case B, where phase constants are quite apart. On the other hand, the simulator makes correct predictions qualitatively speaking, and the transversal field distributions match with those determined by Dudley [16] and Holloway [38].

4.3 Arched Tunnels

Performance of the spectral technique in rectangular and circular tunnels has been assessed so far. The former proved to be very valuable from a modal point of view, as approximate closed expressions are available regarding to mode computation and allowed to understand the propagation phenomena happening in the

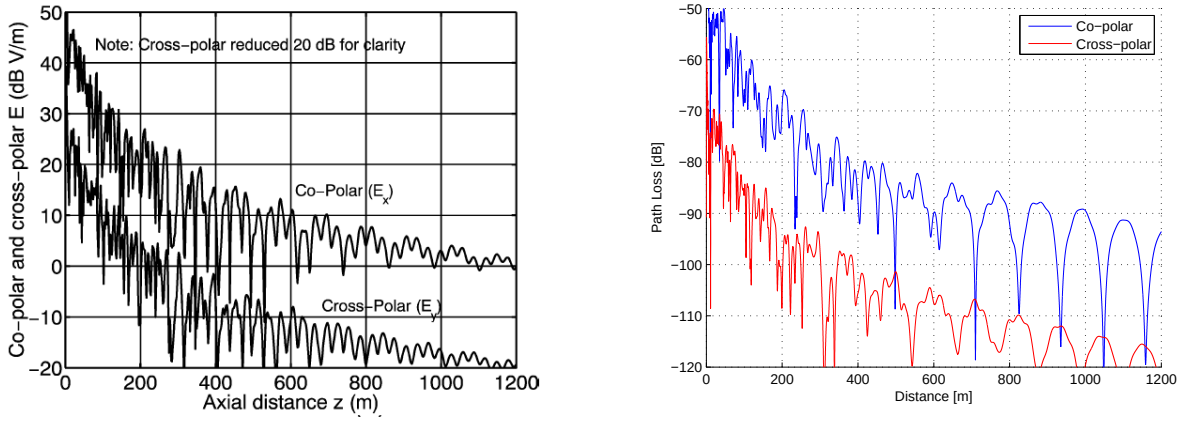

(a) Theoretical results taken from [14], Fig.16.

(b) Simulation results.

Figure 4.12: Comparison at position D. $f = 1GHz$. Cross-polars reduced $20dB$.

tunnel. On the other hand it offered very little insight on cross-polarisation. The latter presents some issues in regard to practical applications in real tunnel scenarios but helped to ensure the presence of cross-polarisation in the spectral technique when proper conditions are present. The arched tunnel is a particularisation of the circular case with the advantage that there is much more information available ranging from theoretical studies [24],[15] to extensive measurements in tunnels with such geometry [18]. A typical arched tunnel cross-section is shown in Fig.4.13.

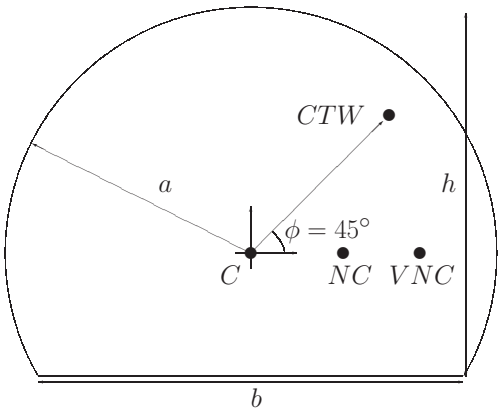

Figure 4.13: Semi-arched tunnel.

Proceeding in the same fashion as for the rectangular tunnel, short distance behaviour will be analysed first. To this end, the Xin-hai tunnel, measured by Wang and Yang [18] is used. The parameters of the measurement campaign are specified in Table 4.7. They developed a ray-tracing method, as Didascalou et al. did [40], to also run simulations.

They use two simultaneous horizontally-polarised transmitters placed at the tunnel ceiling, the signal strength being measured with the receiver both at vertical and horizontal polarisations. Results can be compared in Figs.4.14 and 4.15, with Rx polarisation horizontal and vertical respectively. Better agreement

Frequency			$f = 943.4MHz$
Tunnel dimensions	Radii		$a = 5m$
	Height		$H = 6.22m$
	Length		$L = 450m$
Transmitter(Tx)	Polarisation		Horizontal
	Position Tx1	Horizontal	$x_{Tx1} = 2m$
		Vertical	$y_{Tx1} = 5.22m$
	Position Tx2	Horizontal	$x_{Tx2} = -2m$
		Vertical	$y_{Tx2} = 5.22m$
Receiver(Rx)	Polarisation		Horizontal and Vertical
	Position	Horizontal	$x_{Rx} = 2m$
		Vertical	$y_{Rx} = 1.8m$

Table 4.7: Simulation parameters for the arched tunnel taken from [18].

is reached for the former, where the pattern and overall attenuation are quite similar between measurements and spectral simulations. For the latter, there are more similarities with the ray-tracing simulations than with measurements. The measured fall-off for the first $70m$ is larger than predicted, while at larger distances the closeness between ray-tracing and spectral simulations is noticeable. In general, though, the path loss dynamic range are on the same order for both HH and HV polarisations.

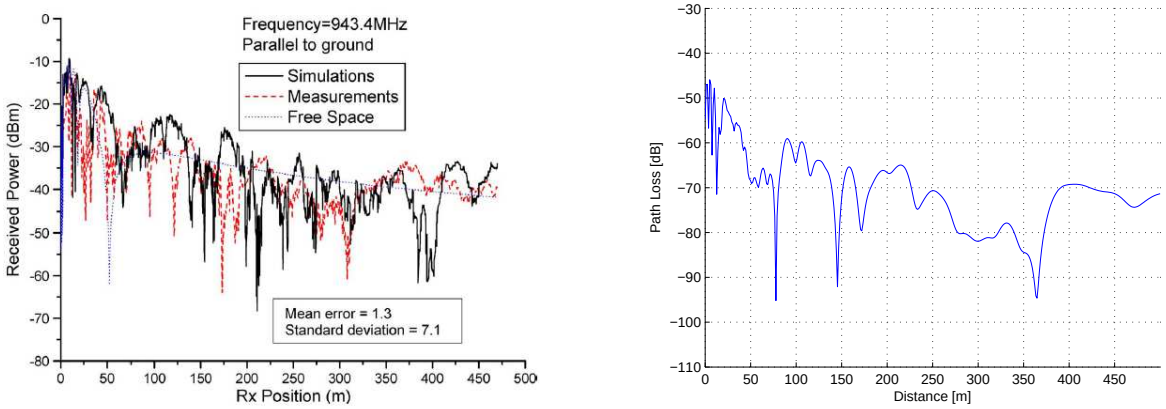

(a) Measurements taken from [18], Fig.7.

(b) Simulation results.

Figure 4.14: Results comparison at Xinhai tunnel. Horizontal Rx polarisation.

As for the long-term behaviour of the simulator in arched tunnels, the Lienard experiments [16] of Section 4.1 are recalled. On top of that, the more complete analysis undertaken by Molina-García-Pardo [24] in the same environment will also be used. Measurements for the latter were performed in the same tunnel at more frequency bands and antenna positions, allowing a better assessment of the spectral technique performance in such tunnels. The extended information is gathered in Table 4.8, while the rest of the parameters are those of Table 4.2.

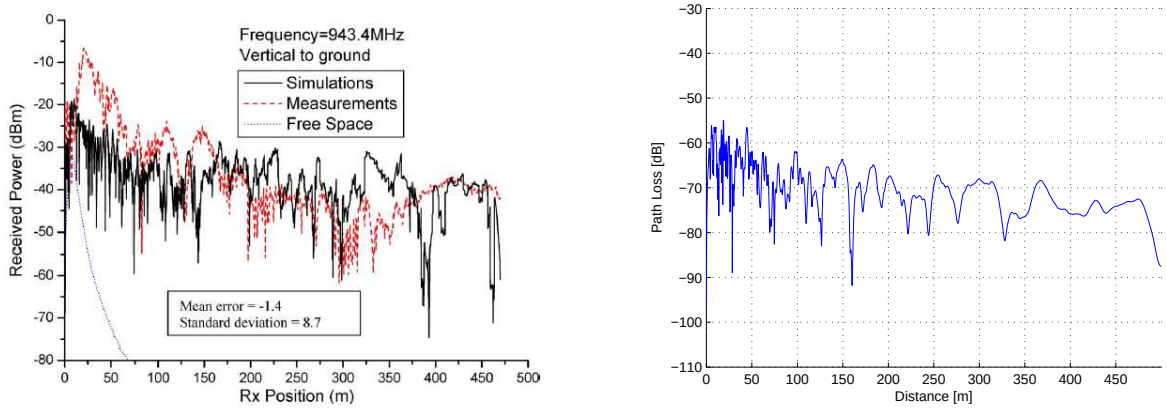

(a) Measurements taken from [18], Fig.8.

(b) Simulation results.

Figure 4.15: Results comparison at Xinhai tunnel. Vertical Rx polarisation.

Frequencies	$f_1 = 450MHz$	$f_2 = 510MHz$	$f_3 = 900MHz$	$f_4 = 2GHz$	$f_5 = 5GHz$
	Position	C	NC	VNC	CTW
Transmitter	x_{Tx}	$0m$	$2m$	$3.1m$	$2.5m$
	y_{Tx}	$2m$	$2m$	$2m$	$4.3m$

Table 4.8: Measurement parameters by Molina-García-Pardo [24].

Note that the experiment at f_1, f_2, position NC, corresponds to the Lienard measurements of Section 4.1. This time no equivalent tunnel cross-section is used, but the real arched one instead. A similar pattern to that of Fig.4.5 is obtained, the results being presented in Table 4.9 for measurements, simulations with the equivalent rectangular cross section and simulations with the arched cross-section. The attenuation decreases when the arched tunnel is simulated, but phase constants have close values. For the arched cross section, inaccuracy on the attenuation is higher than $1dB/km$, that is the bound for which the spectral simulator has heretofore been able to make predictions.

Frequency	Case	Attenuation [dB/Km]	Pseudo-periodicity [m]
$450MHz$	Measurements	33.0	240
	Rectangular Sim.	24.1	241
	Arched Sim.	16	240
$900MHz$	Measurements	8.5	486
	Rectangular Sim.	8.7	485
	Arched Sim.	5.7	486

Table 4.9: Parameter comparison. Arched tunnel. Position NC, Polarisation VV.

Moreover, Molina [24] completed the analysis at positions C, NC of Fig.4.13 at f_1, f_2, f_3 for two polarisations: HH, where Tx and Rx are horizontally polarised, and VV, where both are vertically polarised. Table 4.10 compares the measured values for attenuation and pseudo-periodicity with the simulator results

providing better insight. The VV polarisation offers more accurate results for the phase constant than the HH polarisation and it is just the opposite for the attenuation constant: even though attenuation values are generally larger for HH cases and smaller for VV cases, phase constant in the latter case are retrieved with higher accuracy than for the HH case. Also, the trend commented in previous sections holds: the attenuation constant usually has more error than the phase constant, as the simulated pseudo-periodicity matches pretty well with measured values.

Frequency	Position	Polarisation	Case	Attenuation $[dB/Km]$	Pseudo-periodicity $[m]$
$450MHz$	C	VV	Measurements	29.2	86
			Simulations	20.3	88
$510MHz$	C	HH	Measurements	11	156
			Simulations	15.4	117
		VV	Measurements	23	106
			Simulations	16.4	106
$900MHz$	C	HH	Measurements	3.53	253
			Simulations	6	200
		VV	Measurements	7.5	190
			Simulations	6.8	189
	NC	HH	Measurements	4	505
			Simulations	5.7	526

Table 4.10: Parameter comparison. Arched tunnel.

A more practical case in tunnels occurs when the source is displaced towards the lateral wall. The f_2 results at position VNC of Fig.4.13 are plotted in Fig.4.16. Larger attenuation is obtained for the VV polarisation rather than for the HH, and values do not differ much in both cases respect to measurements. But the pseudo-periodicity for the HH case is not correctly predicted.

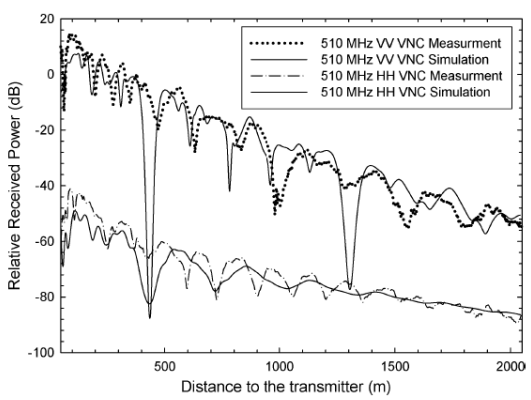

(a) Measurements taken from [24], Fig.4.

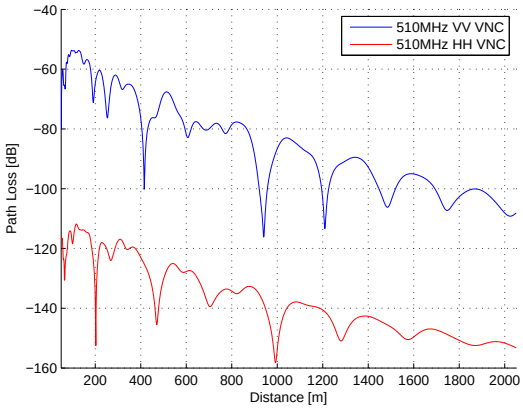

(b) Simulation results.

Figure 4.16: Results comparison at $f_2 = 510MHz$. VNC position. HH polarisation reduced $60dB$.

Similar to the Dudley experiment to study cross-polarisation, the source at f_2, f_4 and f_5 frequencies is placed at the CTW position in order to maximise the impact of this effect in propagation. Fig.4.17 depicts the propagation at f_2, where it can be observed how the difference between co-polar and cross-polar components is larger in simulations than in measurements.

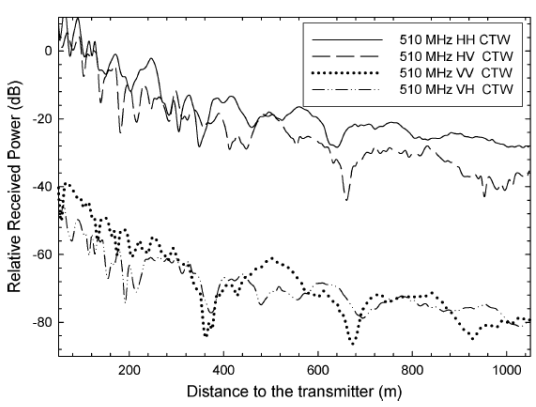

(a) Measurements taken from [24], Fig.5.

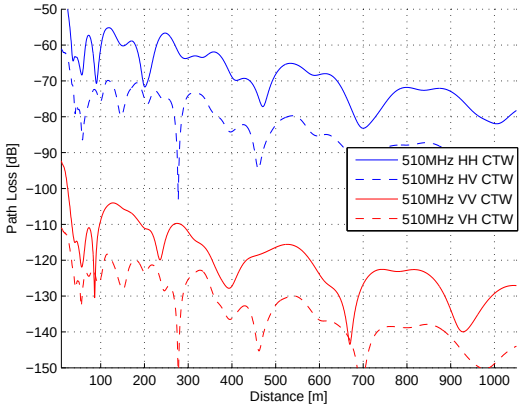

(b) Simulation results.

Figure 4.17: Results comparison at $f_2 = 510MHz$. CTW position. VV and VH polarisations reduced $60dB$.

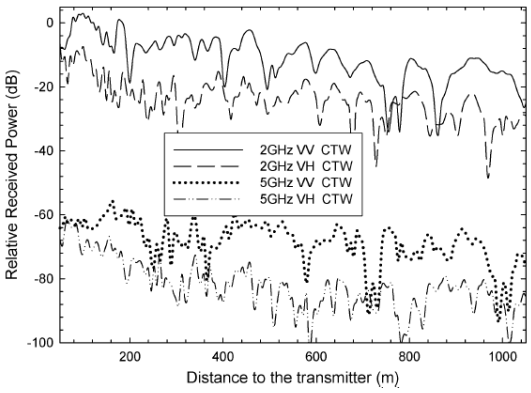

(a) Measurements taken from [24], Fig.6.

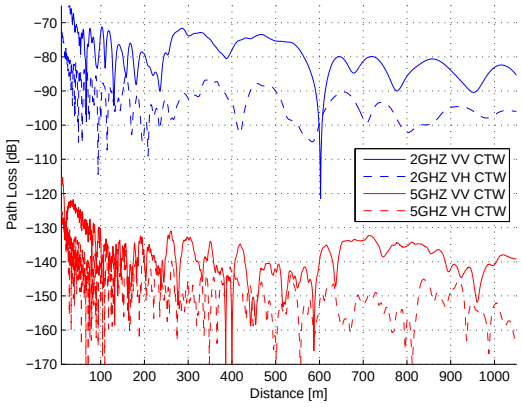

(b) Simulation results.

Figure 4.18: Results comparison at $f_4 = 2GHz$ and $f_5 = 5GHz$. CTW position.

Adding a random angle of incidence because of the wall roughness proximity did not introduce much changes at 510MHz, but it did at f_4 and f_5 in Fig.4.18, reducing the difference between co-polar and cross-polar components. This is probably because wall roughness, modelled by means of the randomness introduced on the incidence angle, has larger impact on short wavelengths. The overall attenuation is correctly predicted but patterns differ quite between them.

Summarising, results for the VNC and CTW positions suggest that the behaviour of the simulator gets worse as the source gets closer to the tunnel bounds. The reason seems to be the application of BC,

because it generates discontinuities at the boundary that lead to the incorrect calculation of the appropriate propagation constants by the spectral technique. An exception has been proven to be the Xin-hai experiment by Wang and Yang [18], analyzed at the beginning of this section, where the two transmitters were placed close to the tunnel ceiling: simulation results resembled quite to measurements, although it must be noted that the obtained path loss was at the receiver position, situated in the inner part of the cavity.

4.4 Bended Tunnels

Another scenario of interest are curved paths, where most of the train underground activities take place. It has been shown in Section 3.2.3 that the curve modelling has a definitive impact on the simulator output. This section addresses the need to determine the range of parameters in which the spectral technique is able to successfully predict the EM behaviour in such scenarios.

Modal analysis on curved tunnels has been developed since the mid 70's [41], and more recently Mahmoud [15] completed the analysis in curved rectangular tunnels. There is a large number of publications containing measurements in curved tunnels [42],[43],[36],[44],[45]. Unfortunately, many of them do not give details on the course the tunnel follows, thus making it difficult to compare with the spectral technique. Simulations performed by Wang and Yang [18] with their ray-tracing software will be used as a reference.

Frequency			$f = 1GHz$
Tunnel dimensions	Width		$w = 8m$
	Height		$H = 6m$
	Radii		$r = \infty, 150, 300m$
	Curve length		$L = 400m$
	Total length		$L = 100, 150m$
Transmitter(Tx)	Polarisation		Vertical
	Position	Horizontal	$x_{Tx} = 0m$
		Vertical	$y_{Tx} = 3m$
Receiver(Rx)	Polarisation		Vertical
	Position	Horizontal	$x_{Rx} = 0m$
		Vertical	$y_{Rx} = 1.5m$

Table 4.11: Simulation parameters for the curved tunnel taken from [18]

They studied the impact the curvature radius and length of the curved section have on propagation. The parameters they chose are collected in Table 4.11, while the results are presented in Figs.4.19 and 4.20. The former compares a straight $100m$-long section, followed by a curved $200m$-long stretch and another $100m$-long section for three different cases: a $r = \infty$ tunnel radius, a $r = 150m$ radius and a $r = 300m$ radius. Note the good agreement between ray-tracing and spectral simulations for the three analyzed cases except for higher peaks in the straight tunnel. As expected, smaller radius of curvature lead to larger losses.

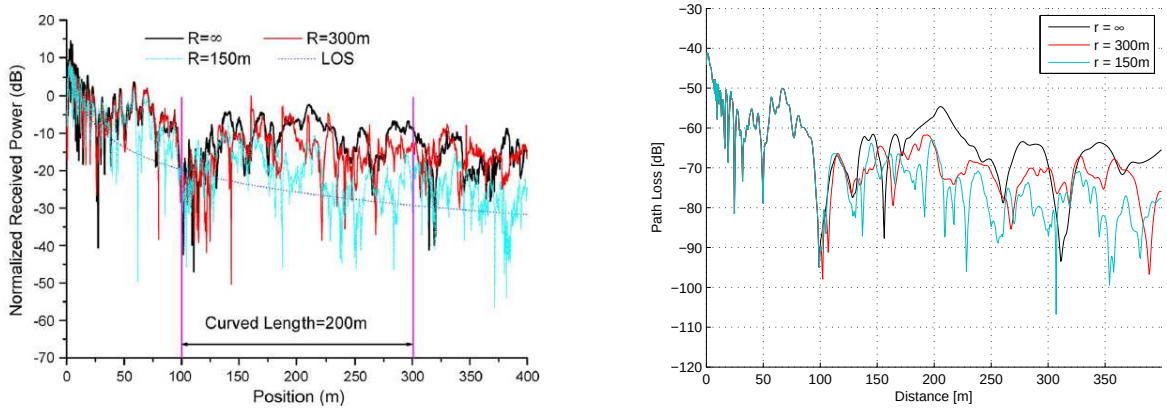

(a) Results taken from [18],Figure 15.

(b) Simulation results.

Figure 4.19: Results comparison for different curvature radii.

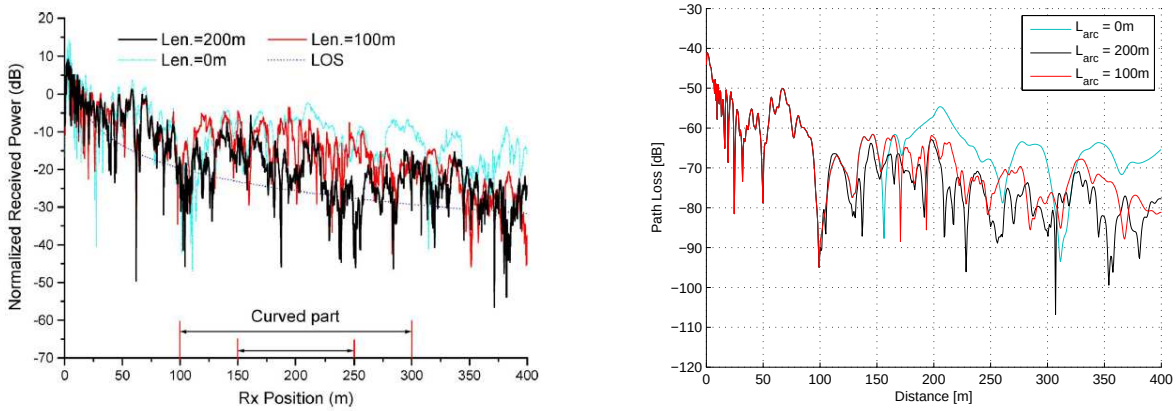

(a) Results taken from [18],Figure 16.

(b) Simulation results.

Figure 4.20: Results comparison for different curvature length.

The second scenario focuses on the relation between path losses and length of a curved stretch in the middle of the simulated path. Again, and for a tunnel radius of $r = 150m$, three tunnels are analyzed: a straight tunnel $L_{arc} = 0m$, a $100m$-straight plus $200m$-curved plus $100m$-straight tunnel - $L_{arc} = 200m$ - and finally a $150m$-straight plus $100m$-curved plus $150m$-straight tunnel $L_{arc} = 100m$. See how the longer the curve, the larger the losses. Again, simulations using both techniques are close and both attenuation and pattern are quite alike.

4.5 Computational Issues in Spectral Propagation

The spectral technique computational efficiency is based on the implemented FFT algorithm. The chosen algorithm used in this case is based on the Cooley-Tuckey version, whose operational order is $O\left(M \log_2(M)\right)$ for 1D-FFT and $O\left(M^2 \log_2(M)\right)$ for 2D-FFT [46], M being the FFT number of points for a square $M \times M$ matrix. Square matrices are used within the examples illustrated throughout the thesis because of tunnels

cross-section geometry and better FFT performance. Because of the several scenarios chosen to illustrate the performance of the spectral technique, the parameters varied between the following values:

- Frequency: $f = 400MHz - 6GHz$
- Sampling distance: $\Delta = \lambda/4 - \lambda/20$
- Number of points: $M = 128 - 1024$

Within the ranges of operation mentioned above, the totality of the tunnels presented throughout this document can be analysed. In general, sampling frequency is set equal to the working frequency. Hence, lower frequencies allow to work with less points because their wavelengths are larger: less points are needed to span the whole spatial domain. Also, small irregularities on the tunnel cross-section - originated during the quantisation process - do not affect the outgoing prediction at these frequencies, so coarser meshes - such as $\Delta = \lambda/4$ for instance - can be used. This is the case of frequencies up to $900MHz$, allowing the use of $M = 128, 256$ points, that are executed at a very high rate by general-use computer processors.

On the other hand, higher frequencies - whose wavelength is on the same order as the tunnel roughness, a few centimeters - require more points and finer meshes, such as $\Delta = \lambda/10, \lambda/20$.When the $\Delta = \lambda/4$ is used at these frequencies, the mesh is useful to obtain a preliminary qualitative idea of the simulated environment. Then, in these cases the number of points are usually in the $M = 512, 1024$ range, whose execution time slowed considerably respect to the $M = 128, 256$ cases.

The spectral algorithm described in Section 3 iterates N times - the tunnel length, in points - the following instructions:

1. Two 2-D FFT to convert the spatial field distributions into the Angular Plane Wave Spectrums (APWS), one per field component.
2. Two point-per-point multiplications between the field components and the propagation phasor.
3. Two 2-D IFFT to retrieve the spatial field distributions from APWS.
4. Two point-per-point multiplications between the field components and the attenuation mask.

Steps 1 and 3 complexity is $O\left(M^2 \log_2(M)\right)$, while steps 2 and 4 have $O\left(M^2\right)$ order. Thus, for sufficiently large M values the algorithm asymptotical would be:

$$S_{order} = O(M^2 \log_2 M) \tag{4.1}$$

It must be noted, though, that the number of times the loop iterates the process longitudinally, N, has not been included on the previous expression because it varies greatly depending on the analysis being carried over: near source studies, up to a few hundred meters, will typically command a number of iterations N of some hundred times at small frequencies or a few thousand times at large frequencies. Meanwhile, long range analysis will account for intensive computational work. See in Fig.4.21 how the number of operations needed to perform propagation drastically increases for values higher than $M = 512$, and how for values such as $M = 128, 256, 512$ the computational burden is less than or in the order of 10^6 operations.

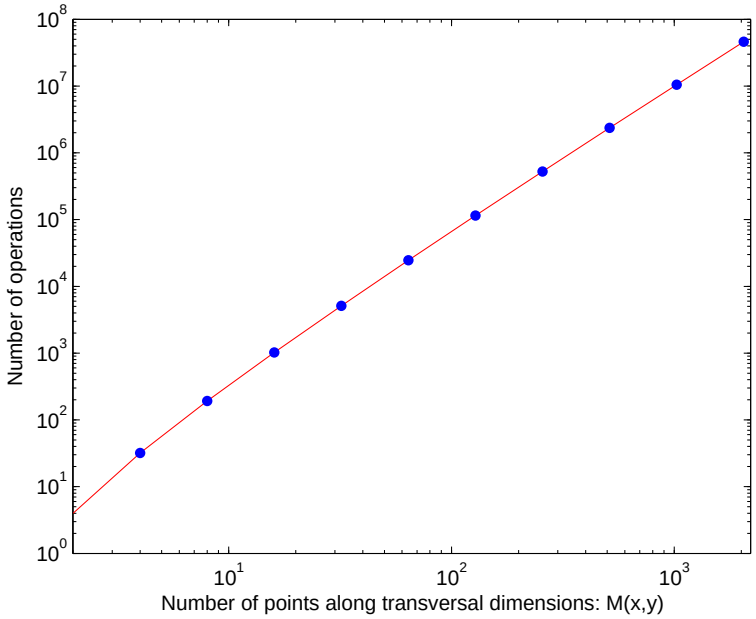

Figure 4.21: Simulations complexity as a function of the transversal dimensions. Spectral case

The required memory space is the second issue discussed in this section. It is well-known that fast access memory modules avoid time-costly disk access, so it is critical to limit this parameter to a reasonable value. The algorithm needs four $M \times M$ arrays containing the field distributions in the spatial domain and the APWS, two per polarisation, and two more highly-compressible arrays of the same dimensions for the propagation phasor and the attenuation mask, whose majority of points are zero, so they can be ignored. On top of that, output arrays containing axial evolution - $1 \times N$ - can be neglected but horizontal cuts along the tunnel - $M \times N$ - must be added to the amount of memory required. A typical case consists on storing the vertical and horizontal cuts at a significant point in the tunnel for both polarisations. This case would lead to a total memory requirement of:

$$\left(4M^2 + 2 \times 2 \times MN\right) bytes \tag{4.2}$$

Supposing a longitudinal length in points of $N = 5000$, which would correspond to a $375m$-long stretch for a sampling frequency $F_s = 1GHz$ and step $\Delta z = \lambda/4$, Fig.4.22 shows the required memory for the range of M values used throughout the thesis. Two traces are plotted, the first - $d = 1$ - being that corresponding to the case where all data points are stored. See how for values larger than of $M = 512$ the free memory space needed is more than $10GB$ approximately. This amount proves to be excessively large for a common-use PC, so a decimating factor $d = 8$ on the output array can be applied to reduce number of stored data points, thus decreasing the needed amount of memory, as showed in the second trace.

Anyway, the $d = 8$ decimating factor permits a more than qualitative look at field distribution. At large frequencies and for sampling distances in the order of $\Delta = \lambda/4, \lambda/10$ the distance between observable points may be on the order of a dozen centimetres, more than enough for the purpose of application in the current EM study in tunnels.

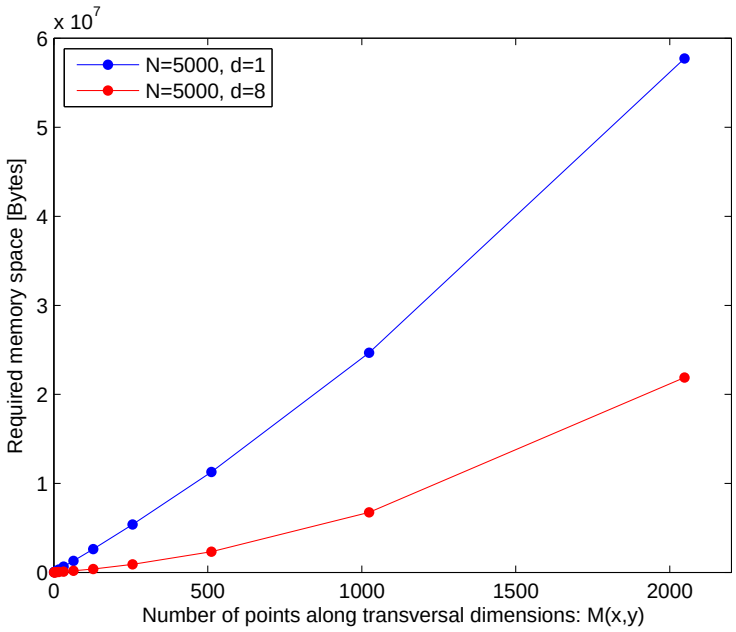

Figure 4.22: Memory requirements as a function of the transversal dimensions. Spectral case.

After running several simulations it has been found that both M and N are equally time-limiting: the former because of the FFT size implying larger CPU effort, and the latter because large values finally lead to time consuming disk access operations.

4.6 Conclusions on Spectral Propagation

The scope of this chapter was showing the behaviour of the implemented spectral technique and its limitations have also been exposed. Predictions are good in many cases, while there are some of them where they differ notably from the chosen references.

The main problems have been identified in arched tunnel profiles and highlighted when the source is placed close to the tunnel boundaries, due to the importance that boundary conditions take under those circumstances. The implementation of the vector BC described in Section 3.3 works properly in rectangular tunnel cross-sections and also when the source is placed in the inner part of the tunnel. However, the previously mentioned issues are still there and must be resolved. After seeing the results, it is clear that the optical approach taken for the BC implementation is not 100% suited for the spectral techniques. Several alternatives were used, none of them providing significant improvements, so it was decided sticking with the current version while addressing its limitations with a new technique where the application of BC was easier.

Another reason for this path was the computational burden implied by the full-tunnel analysis. If propagation at high frequencies want to be studied, simulation time must be reduced somehow. Some simulations presented in this chapter took almost a full day of intensive computation and there are alternatives that can reduce this span while also providing accurate predictions.

The parabolic technique for EM propagation was chosen because it solved the mentioned issues, the

following chapters devoted to its description, implementation and results.

Chapter 5

Parabolic Equation Approach for Propagation in Tunnels

As it has been mentioned in the previous chapter, spectral techniques have shortcomings. After devoting much time to solving the challenges presented it was noticed the advantages that partial differential equations and parabolic techniques offered. They are employed to model several areas of knowledge such as economics, chemistry, biology and physics, representing a powerful and flexible tool when the appropriate conditions are given.

Parabolic Equation (PE) was first used to provide better understanding of the heat equation and physical processes because of its correct modelling of three-dimensional problems with slow variations in one dimension ([47],[48]). Radiowave propagation in enclosed areas such as tunnels is then well-suited to be modelled with PE because the wavefront propagates predominantly along the tunnel longitudinal axis. Assuming a homogeneous cross-section in the far-field region of the transmitting antenna, field variations are smooth enough to allow the use of this method, as Popov [49],[50],[51] has shown in recent years.

The first section presents the Thomas algorithm. The importance of this tool, very useful when dealing with tri-diagonal systems, will be highlighted in subsequent sections. The second section derives the Parabolic Equation (PE) from Helmholtz' wave equation and the third one is devoted to the Alternating Direction Implicit (ADI) technique, an efficient method to solve the vector PE (VPE). The last section in this chapter deals with boundary conditions application and results validation.

5.1 The Thomas Algorithm

The Thomas algorithm is a powerful tool used to solve tri-diagonal systems in a simple an efficient manner. A tri-diagonal system can be, for instance, a system of partial differential equations where central differences scheme is used to calculate the partial derivatives:

$$\frac{\partial^2 u_l}{\partial x^2} = \frac{u_{i-1} - 2u_i + u_{i+1}}{\Delta x^2} \tag{5.1}$$

See how the value at point $l = i$ is related to its neighbours, specifically in this case the previous and subsequent points. In this case, a smooth tendency is hinted as the values at the three points are interrelated, and so are the values for the rest of points $i = 1...L$. These points could represent the discretisation of a certain field distribution that, from Maxwell equations, must be continuous even on surface discontinuities.

The algorithm presented in this section was developed in the mid-20th century and is a Gaussian-based elimination procedure without pivoting. The algorithm is briefly introduced here, although better insight can be found in [47], [48] as well as in other numerical analysis books.

Consider first a system of equations such as:

$$a_i w_{i-1} + b_i w_i + c_i w_{i+1} = d_i \tag{5.2}$$

with $i = 1, 2, ..., K$. In matrix form it can be arranged as:

$$\underline{\underline{A}} \cdot \underline{w} = \underline{d} \tag{5.3}$$

Vector $\underline{w}$ has K unknowns. It represents a row or column of a field matrix. Hence, the first and last elements, w_1 and w_K, can be determined applying the boundary conditions. Matrix $\underline{\underline{A}}$ has tri-diagonal form:

$$\begin{bmatrix} 1 & 0 & & & & \\ a_1 & b_1 & c_1 & & \underline{\underline{0}} & \\ & a_2 & b_2 & c_2 & & \\ & \ddots & \ddots & \ddots & & \\ & & a_i & b_i & c_i & \\ & & & \ddots & \ddots & \ddots \\ & \underline{\underline{0}} & & & a_{K-1} & b_{K-1} & c_{K-1} \\ & & & & 0 & 1 \end{bmatrix}$$

Hence, w_i is computed off its neighbour values w_{i-1} and w_{i+1}. A solution of the form:

$$w_i = p_{i+1} w_{i+1} + q_{i+1} \tag{5.4}$$

is chosen in order to proceed as in Gaussian elimination. Substituting Eq.5.4 in Eq.5.2, the number of unknowns is reduced so that:

$$w_i = p_{i+1} w_{i+1} + q_{i+1} \tag{5.5}$$

with:

$$p_{i+1} = \frac{-c_i}{a_i p_i + b_i} \tag{5.6}$$

$$q_{i+1} = \frac{d_i - a_i q_i}{a_i p_i + b_i} \tag{5.7}$$

By application of boundary conditions, $w_1 = \beta_1$ and $w_K = \beta_K$ are found together with the rest of p_i and q_i values with Eqs.(5.6) and (5.7). The algorithm requires that $\mid p_i \mid \leq 1$ for all i values to be well-conditioned. Otherwise increased error would propagate throughout Eq.(5.6). From here, unknowns w_i are found by backsubstitution using Eq.(5.5).

5.2 The Parabolic Equation

Consider an oversized rectangular waveguide, sampled with a grid with axis on the x and y directions. Let Δx and Δy be the sampling distance over both axis and Δz the propagation step in the longitudinal axis. The solution of the parabolic equation over this grid will account for propagation on rectangular tunnels but, as [24] has shown, propagation in arched tunnels can be successfully studied by means of an equivalent rectangular tunnel.

It starts with the Helmholtz equation applied to the electric scalar potential F:

$$\left(\frac{\partial^2}{\partial x^2}+\frac{\partial^2}{\partial y^2}+\frac{\partial^2}{\partial z^2}+k_0^2\right)F(x,y,z)=0 \tag{5.8}$$

A solution of the form:

$$F(x,y,z)=U(x,y,z)e^{-jk_0z} \tag{5.9}$$

is chosen with U representing the plane wave solution along the axial directions and e^{-jk_0z} a common fast-varying phase term along the z-axis. Substitute Eq.5.9 into Eq.(5.8) and what follows is:

$$\begin{aligned}&\frac{\partial^2}{\partial x^2}\left\{Ue^{-jk_0z}\right\}+\frac{\partial^2}{\partial y^2}\left\{Ue^{-jk_0z}\right\}+\\&\frac{\partial^2}{\partial z^2}\left\{Ue^{-jk_0z}\right\}+k_0^2Ue^{-jk_0z}=0\end{aligned} \tag{5.10}$$

If the chain rule is applied on the z partial derivative, then the previous expression becomes:

$$\begin{aligned}&\frac{\partial^2U}{\partial x^2}e^{-jk_0z}+\frac{\partial^2U}{\partial y^2}e^{-jk_0z}+\\&\frac{\partial}{\partial z}\left\{\frac{\partial U}{\partial z}e^{-jk_0z}+U\frac{\partial}{\partial z}\left\{e^{-jk_0z}\right\}\right\}+\\&k_0^2Ue^{-jk_0z}=0\end{aligned} \tag{5.11}$$

Applying the chain rule again:

$$\begin{aligned}&\frac{\partial^2U}{\partial x^2}e^{-jk_0z}+\frac{\partial^2U}{\partial y^2}e^{-jk_0z}+\\&\frac{\partial^2U}{\partial z^2}e^{-jk_0z}+2\frac{\partial U}{\partial z}\frac{\partial}{\partial z}\left\{e^{-jk_0z}\right\}+\\&U\frac{\partial^2}{\partial z^2}\left\{e^{-jk_0z}\right\}+k_0^2Ue^{-jk_0z}\quad=\quad 0\end{aligned} \tag{5.12}$$

The nth-order derivatives of the phase term are:

$$\frac{\partial^n}{\partial z^n}\left\{e^{-jk_0z}\right\}=(-jk_0)^ne^{-jk_0z} \tag{5.13}$$

If the previous expression is substituted in Eq.(5.12):

$$\begin{aligned}&\frac{\partial^2U}{\partial x^2}e^{-jk_0z}+\frac{\partial^2U}{\partial y^2}e^{-jk_0z}+\\&\frac{\partial^2U}{\partial z^2}e^{-jk_0z}-2jk_0\frac{\partial U}{\partial z}e^{-jk_0z}+\\&(jk_0)^2Ue^{-jk_0z}+k_0^2Ue^{-jk_0z}=0\end{aligned} \tag{5.14}$$

The last two terms cancel in the expression above. Grouping the z-derivative on one side of the equality and ignoring the phase term:

$$2jk_0\frac{\partial U}{\partial z} - \frac{\partial^2 U}{\partial z^2} = \frac{\partial^2 U}{\partial x^2} + \frac{\partial^2 U}{\partial y^2} \tag{5.15}$$

Here, the parabolic approximation must be stated. Let θ be the angle of propagation relative to the z-axis. If fields are to vary smoothly as the wavefront progresses through the waveguide, plane waves must propagate with small θ angles. Then, the following holds:

$$\left|\frac{\partial^2 U}{\partial z^2}\right| \ll k_0\left|\frac{\partial U}{\partial z}\right| \tag{5.16}$$

The second term on the left side of Eq.(5.15) can thus be neglected and the SPE is obtained:

$$\frac{\partial U}{\partial z} = \frac{1}{2jk_0}\left(\frac{\partial^2 U}{\partial x^2} + \frac{\partial^2 U}{\partial y^2}\right) \tag{5.17}$$

Popov in [49],[50],[51] derives the full vectorial parabolic equation for arbitrary cross-sections and curved paths following a similar analysis as the one performed in this section.

5.3 The Alternating Direction Implicit Method

The Alternate Direction Implicit method solves the parabolic equation found in Eq.(5.17) in two steps at reasonable computational cost. A complex two-dimensional problem is reduced to several one-dimensional problems as the method iteratively finds the propagated field line per line. In the first step the outcome is determined by variations in one of the two transversal directions, whereas the second step uses the remaining direction.

Consider a rectangle of dimensions (A, B). A rectangular grid is overimposed as in the following picture:

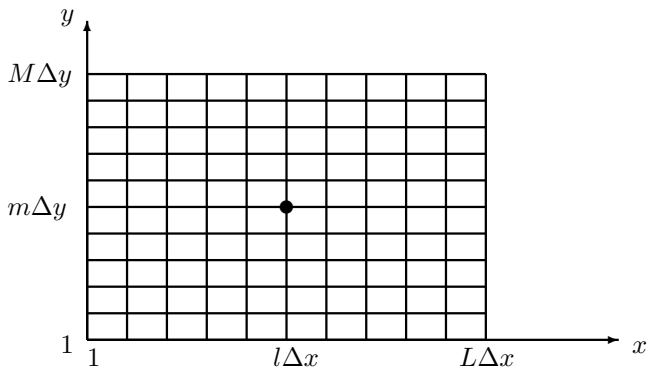

with:

$$A = L\Delta x \tag{5.18}$$

$$B = M\Delta y \tag{5.19}$$

and:

$$l = 1, 2, ..., M \tag{5.20}$$

$$m = 1, 2, ..., L \tag{5.21}$$

Suppose now that $\underline{\underline{U}}$ is a matrix corresponding to one of the transversal field components E_x or E_y. Eq.(5.17) can be rewritten as follows:

$$\frac{\partial \underline{\underline{U}}}{\partial z} = A_1 \underline{\underline{U}} + A_2 \underline{\underline{U}} \tag{5.22}$$

where A_1 and A_2 are two linear operators defined as:

$$A_1 = \frac{1}{2jk_0} \frac{\partial^2}{\partial x^2} \tag{5.23}$$

$$A_2 = \frac{1}{2jk_0} \frac{\partial^2}{\partial y^2} \tag{5.24}$$

The differential scheme is taken around the centre point between two consecutive propagation steps so that:

$$z = (n + 1/2)\Delta z \tag{5.25}$$

The Taylor series expansion of Eq.(5.22) is:

$$\begin{aligned} \frac{\underline{\underline{U}}^{n+1} - \underline{\underline{U}}^{n}}{\Delta z} =& \frac{1}{2}\left(A_1 \underline{\underline{U}}^{n+1} + A_1 \underline{\underline{U}}^{n}\right) + \\ & \frac{1}{2}\left(A_2 \underline{\underline{U}}^{n+1} + A_2 \underline{\underline{U}}^{n}\right) + O(\Delta z^2) \end{aligned} \tag{5.26}$$

where $O(\cdot)$ is the error related to higher order terms of the Taylor series not taken into account. Regrouping terms the previous expressions can be rewritten as:

$$\begin{aligned} &\left(I - \frac{\Delta z}{2} A_1 - \frac{\Delta z}{2} A_2\right) \underline{\underline{U}}^{n+1} = \\ &\quad \left(I + \frac{\Delta z}{2} A_1 + \frac{\Delta z}{2} A_2\right) \underline{\underline{U}}^{n} + O(\Delta z^3) \end{aligned} \tag{5.27}$$

with I the identity matrix. This is the Crank-Nicolson scheme for the parabolic equation. Although the solution for $\underline{\underline{U}}^{n+1}$ can be obtained at this point, inverting the matrix may prove to be too hard computationally when using large meshes. ADI overcomes this problem by decomposing the matrix line per line in two steps. To do so, the term $\Delta z^2 A_1 A_2 \underline{\underline{u}}^{n+1}/4$ is added on both sides and the expression is factored:

$$\begin{aligned} &\left(I - \frac{\Delta z}{2} A_1\right)\left(I - \frac{\Delta z}{2} A_2\right) \underline{\underline{U}}^{n+1} = \\ &\quad \left(I + \frac{\Delta z}{2} A_1\right)\left(I + \frac{\Delta z}{2} A_2\right) \underline{\underline{U}}^{n} + \\ &\quad \frac{\Delta z^2 A_1 A_2}{4}\left(\underline{\underline{U}}^{n+1} - \underline{\underline{U}}^{n}\right) + O(\Delta z^3) \end{aligned} \tag{5.28}$$

The last term order is Δz^3, so it can be included in the error term:

$$\begin{aligned} &\left(I - \frac{\Delta z}{2} A_1\right)\left(I - \frac{\Delta z}{2} A_2\right) \underline{\underline{U}}^{n+1} = \\ &\quad \left(I + \frac{\Delta z}{2} A_1\right)\left(I + \frac{\Delta z}{2} A_2\right) \underline{\underline{U}}^{n} + O(\Delta z^3) \end{aligned} \tag{5.29}$$

A new error term is introduced when the equation is discretized. Let A_{1h} and A_{2h} be the second-order approximations of A_1 and A_1 respectively. Both error terms can be included in a new variable $\underline{\underline{V}}$ so that:

$$\left(I - \frac{\Delta z}{2} A_{1h}\right)\left(I - \frac{\Delta z}{2} A_{2h}\right)\underline{\underline{V}}^{n+1} = \left(I + \frac{\Delta z}{2} A_{1h}\right)\left(I + \frac{\Delta z}{2} A_{2h}\right)\underline{\underline{V}}^{n} \tag{5.30}$$

that is the final expression of the ADI method. Peaceman and Rachford (P-R) rewrote it in a two-step formula that computed the field in the next propagating plane $\underline{\underline{U}}^{n+1}$ from the known values in the $\underline{\underline{V}}^{n}$ plane by means of an intermediate virtual plane $\underline{\underline{\tilde{V}}}^{n+1/2}$:

$$\left(I - \frac{\Delta z}{2} A_{1h}\right)\underline{\underline{\tilde{V}}}^{n+\frac{1}{2}} = \left(I + \frac{\Delta z}{2} A_{2h}\right)\underline{\underline{V}}^{n} \tag{5.31}$$

$$\left(I - \frac{\Delta z}{2} A_{2h}\right)\underline{\underline{V}}^{n+1} = \left(I + \frac{\Delta z}{2} A_{1h}\right)\underline{\underline{\tilde{V}}}^{n+\frac{1}{2}} \tag{5.32}$$

The discretized second-order differential operators A_{1h} and A_{2h} defined in Eqs.(5.23,5.24) can be computed by means of a central differences scheme such as:

$$A_{1h}u_{m,l} = \frac{1}{2jk_o}\frac{\partial^2 u}{\partial x^2} = \frac{1}{2jk_o}\frac{u_{m+1,l} - 2u_{m,l} + u_{m-1,l}}{\Delta x^2} \tag{5.33}$$

$$A_{2h}u_{m,l} = \frac{1}{2jk_o}\frac{\partial^2 u}{\partial y^2} = \frac{1}{2jk_o}\frac{u_{m,l+1} - 2u_{m,l} + u_{m,l-1}}{\Delta y^2} \tag{5.34}$$

From the previous expressions, differentiation at a certain point $u_{m,l}$ solely depends on the neighbour elements of the same row or column. Hence, Eqs.(5.31,5.32) become 2 tri-diagonal systems that can be solved by means of the Thomas algorithm.

To ensure convergence of the ADI method, values for the different Δx, Δy and Δz must fulfil conditions imposed by the PE-ADI scheme [52],[47]. These parameters determine the error that is introduced by the method through the calculations via finite differences scheme. Zelley [53] showed, while implementing his method, that with a ratio of $\frac{\Delta x, \Delta y}{\Delta z} = \frac{1}{8}$ the error introduced is much smaller than $1dB$, while Martelly [54] obtained a 5% error for a ratio of $\frac{\Delta x, \Delta y}{\Delta z} = \frac{1}{20}$. Compared to Nyquist criteria to which the spectral technique is subdued, it immediately follows that simulation time will decrease significantly.

ADI solves the fields at the next longitudinal point in two steps. A loop along the z-axis is used to find the fields by means of the Peaceman-Rachford scheme at every iteration. In the first P-R step (see Eq.(5.31)), the field v^n is decomposed column per column and the virtual intermediate plane $\tilde{v}^{n+1/2}$ is found. The column element values are solved with the Thomas algorithm. The second P-R step (see Eq.(5.32)) follows the same procedure to obtain v^{n+1} from $\tilde{v}^{n+1/2}$, but this time the decomposition is performed row-wise.

The propagation logic for the Peaceman-Rachford scheme is summarized in Figs.5.1,5.3. As it has can be seen, BC are specified in a different manners. It is important to note them as implementation differs for each case (see Section5.4). The different p_i, q_i and w_i mentioned below correspond to the notation employed in Section 5.1. There are three different cases:

1. *case* BC_1: boundary conditions applied through p_2 and q_2 to find the first element of the row or column being considered:

   - 1st step, left boundary $\tilde{v}^{n+1/2}_{m,1}$

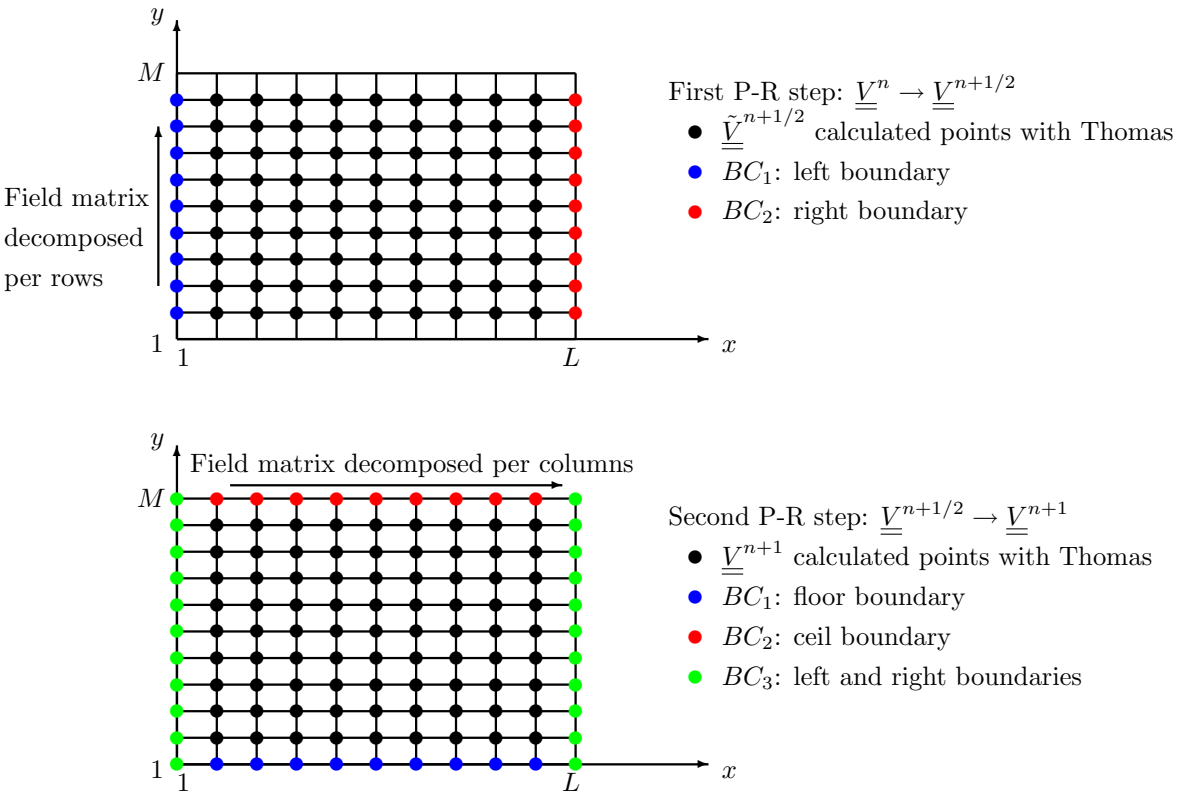

Figure 5.1: The two-step Peaceman-Rachford decomposition

- 2nd step, floor boundary $v_{1,l}^{n+1}$

2. *case* BC_2: boundary conditions applied to the last element of the row or column being considered:

   - 1st step, right boundary $\tilde{v}_{m,L}^{n+1/2}$
   - 2nd step, ceil boundary $v_{M,l}^{n+1}$

3. *case* BC_3: boundary conditions applied at the end of the 2nd step for all possible m values:

   - 2nd step, left boundary $v_{m,1}^{n+1}$
   - 2nd step, right boundary $v_{m,L}^{n+1}$

5.4 Boundary Conditions for PE

The sections that follow describe the expressions encountered for the different p_i, q_i and w_i of the Thomas algorithm of Section 5.1. The latter represent field points of a determined row or column of the field matrix, while the formers are constants related with neighbour field point values and boundary conditions that allow retrieving the field at each propagation step.

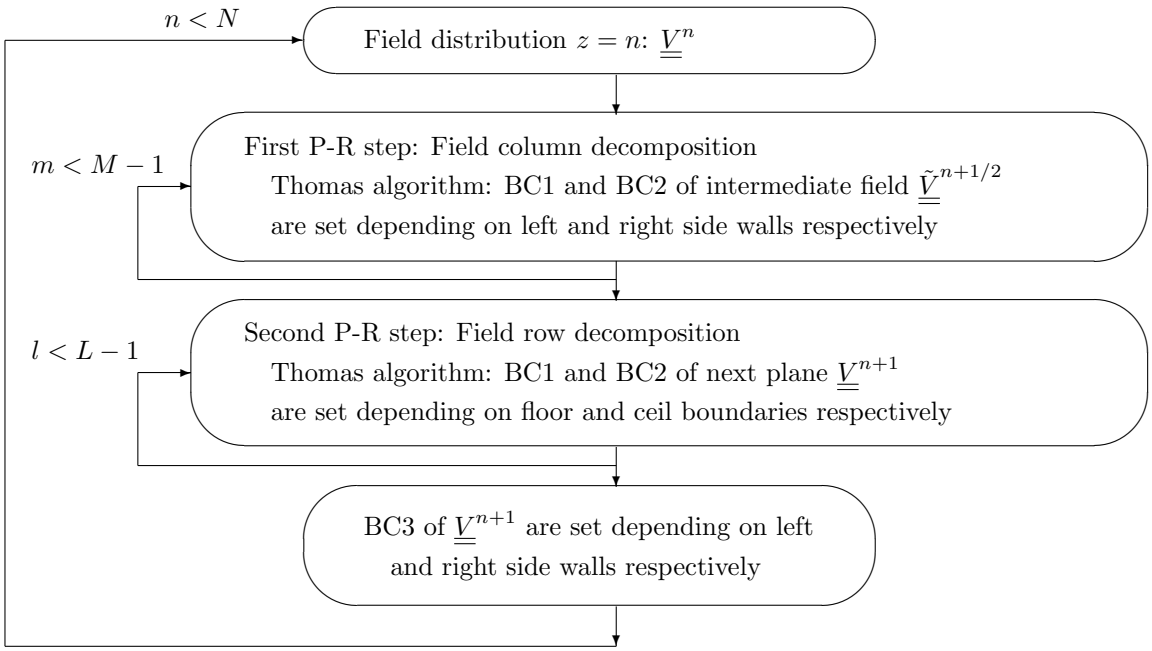

Figure 5.2: Peaceman-Rachford Propagation Scheme.

5.4.1 Dirichlet Boundary Conditions

This boundary condition specifies the value γ that the field must take on the boundary surface. In PEC surfaces, it is used when the boundary surface and the polarisation of the impinging field are parallel. It can be written as:

$$\underline{\underline{U}}|_{BC}^{Dir} = \gamma \tag{5.35}$$

Let $\underline{w}$ be a field row or column of $\underline{\underline{U}}$ being solved with the Thomas algorithm. For the BC_1 case appropriate p_2 and q_2 values must be set. Over PEC surfaces, fields must cancel over the boundary. Thus:

$$w_1 = 0 \tag{5.36}$$

On the other hand, solution has the form stated in Eq.(5.5) so that:

$$w_1 = p_2 w_2 + q_2 \tag{5.37}$$

A pair of values that fulfill the previous equations are:

$$p_2 = 0 \tag{5.38}$$

$$q_2 = 0 \tag{5.39}$$

For cases BC_2 and BC_3 the value must be just set to 0. For instance, when dealing with the right wall on the second Peaceman-Rachford step:

$$v_{m,L}^{n+1} = 0 \tag{5.40}$$

5.4.2 Neumann Boundary Conditions

In this case the boundary condition determines the value that the derivative of the field needs to take to become a valid solution. In PEC surfaces, it is used when the boundary surface and the polarisation of the impinging field are orthogonal. It can be written as:

$$\left.\frac{\partial \underline{\underline{U}}}{\partial n}\right|_{BC}^{Neum} = \gamma \tag{5.41}$$

For points belonging to the boundaries, the centred differentiation scheme cannot be applied and forward differences must be used instead. Thus, when dealing with such points as, for instance, the left boundary:

$$\frac{\partial}{\partial x}\{u_{m,1}\} = \frac{u_{m,2} - u_{m,1}}{\Delta x} \tag{5.42}$$

Now consider the BC_1 case and PEC surfaces. Then:

$$\frac{\partial}{\partial x}\{w_1\} = \frac{w_2 - w_1}{\Delta x} = 0 \tag{5.43}$$

So:

$$w_1 = w_2 \tag{5.44}$$

Again, from Eq.(5.5) it holds that:

$$w_1 = p_2 w_2 + q_2 \tag{5.45}$$

So, for Neumann boundary conditions, p_2 and q_2 must be set equal to:

$$p_2 = 1 \tag{5.46}$$

$$q_2 = 0 \tag{5.47}$$

Proceeding in a similar manner for case BC_2:

$$\frac{\partial}{\partial x}\{w_K\} = \frac{w_K - w_{K-1}}{\Delta x} = 0 \tag{5.48}$$

And:

$$w_K = w_{K-1} \tag{5.49}$$

From Eq.(5.5):

$$w_{K-1} = p_K w_K + q_K \tag{5.50}$$

So, for case BC_2, the values that the last two elements must take are:

$$w_K = w_{K-1} = \frac{q_K}{1 - p_K} \tag{5.51}$$

For case BC_3, as in Eqs.5.44 and 5.49 for the left and right boundaries respectively, the values must be equal to the neighbour values in the horizontal direction for all m values:

$$v_{m,1}^{n+1} = v_{m,2}^{n+1} \tag{5.52}$$

$$v_{m,L}^{n+1} = v_{m,L-1}^{n+1} \tag{5.53}$$

5.4.3 Leontovich Boundary Conditions

Also known as the impedance boundary condition, it applies to non-PEC surfaces. It enforces a field solution that depends on the first-derivative of the field itself over the boundary, as well as the frequency, the boundary surface impedance and the angle of incidence. Let $\underline{U}$ be an array corresponding to x and y field components on the boundary such that $\underline{U} = [U_x, U_y]^T$. Then:

$$\underline{U}\Big|_{BC}^{Leon} = \frac{i}{k_0}\underline{\underline{T_0}}\,\underline{\underline{G_0}}\,\underline{\underline{T_0}}\frac{\partial \underline{U}}{\partial n}\Big|_{BC} \tag{5.54}$$

with:

$$\underline{\underline{T}}_0 = \begin{bmatrix} n_x & n_y \\ n_y & -n_x \end{bmatrix} \tag{5.55}$$

$$\underline{\underline{G}}_0 = \begin{bmatrix} 1/Z & 0 \\ 0 & Z \end{bmatrix} \tag{5.56}$$

$$\frac{\partial U_i}{\partial n} = n_x\frac{\partial U_i}{\partial x} + n_y\frac{\partial U_i}{\partial y} \tag{5.57}$$

Here n_x and n_y are the outward normal components on the boundary domain, and Z the medium surface impedance. Neglecting cross-polarisation effects - i.e., ignoring the rectangle corners - and developing the Leontovich boundary condition, a close expression is found for both U_x and U_y components:

$$U_x\Big|_{left}^{Leon} = \frac{i}{k_0}\left[\frac{n_x^2}{Z} + n_y^2 Z\right]\left[n_x\frac{\partial U_x}{\partial x} + n_y\frac{\partial U_x}{\partial y}\right] \tag{5.58}$$

$$U_y\Big|_{left}^{Leon} = \frac{i}{k_0}\left[n_x^2 Z + \frac{n_y^2}{Z}\right]\left[n_x\frac{\partial U_y}{\partial x} + n_y\frac{\partial U_y}{\partial y}\right] \tag{5.59}$$

On the left boundary $nx = -1$ and $n_y = 0$. Then, for case BC_1:

$$U_x\Big|_{left}^{Leon} = \frac{-i}{k_0}\frac{1}{Z}\frac{\partial U_x}{\partial x} \tag{5.60}$$

$$U_y\Big|_{left}^{Leon} = \frac{-i}{k_0}Z\frac{\partial U_y}{\partial x} \tag{5.61}$$

Suppose $\underline{w}$ is a row of U_x being solved with Thomas. Applying forward differences to 5.60:

$$w_1 = \frac{-i}{k_0}\frac{1}{Z}\frac{w_2 - w_1}{\Delta x} = \gamma_{left}^x\left[w_2 - w_1\right] \tag{5.62}$$

where:

$$\gamma_{left}^x = -i/k_0 Z\Delta x \tag{5.63}$$

Isolating w_1:

$$w_1 = \frac{\gamma_{left}^x}{1+\gamma_{left}^x}w_2 \tag{5.64}$$

And from Eq.(5.5):

$$w_1 = p_2 w_2 + q_2 \tag{5.65}$$

Finally:

$$p_2 = \frac{\gamma_{left}^x}{1+\gamma_{left}^x} \tag{5.66}$$

$$q_2 = 0 \tag{5.67}$$

For a y-polarised field, the solution is the same but replacing γ^x_{left} with:

$$\gamma^y_{left} = -iZ/k_0\Delta x \tag{5.68}$$

instead. When applying the boundary conditions on the floor for the 2nd Peaceman-Rachford step, $n_x = 0$ and $n_y = -1$ and the Leontovich BC become:

$$U_x\Big|^{Leon}_{floor} = \frac{-i}{k_0} Z \frac{\partial U_x}{\partial y} \tag{5.69}$$

$$U_y\Big|^{Leon}_{floor} = \frac{-i}{k_0} \frac{1}{Z} \frac{\partial U_y}{\partial y} \tag{5.70}$$

Solution for p_2 and q_2 are those of Eqs.(5.66,5.67) but with the following γ values instead:

$$\gamma^x_{floor} = \frac{-iZ}{k_0\Delta y} \tag{5.71}$$

$$\gamma^y_{floor} = \frac{-i}{k_0 Z\Delta y} \tag{5.72}$$

BC_2 case applies for two different boundary domains: the right wall in the first Peaceman-Rachford step and the ceil in the second. As for the right wall, $n_x = 1$ and $n_y = 0$ so the solution must fulfill:

$$U_x\Big|^{Leon}_{right} = \frac{i}{k_0} \frac{1}{Z} \frac{\partial U_x}{\partial x} \tag{5.73}$$

$$U_y\Big|^{Leon}_{right} = \frac{i}{k_0} Z \frac{\partial U_y}{\partial x} \tag{5.74}$$

Proceeding in a similar manner as for BC_2 case in the Neumann case the solution has the following form:

$$w_K = \frac{\gamma^x_{right}}{\gamma^x_{right}(1 - p_K) - 1} q_K \tag{5.75}$$

$$w_{K-1} = \frac{\gamma^x_{right} - 1}{\gamma^x_{right}(1 - p_K) - 1} q_K \tag{5.76}$$

with:

$$\gamma^x_{right} = \frac{i}{k_0 Z\Delta y} \tag{5.77}$$

$$\gamma^y_{right} = \frac{iZ}{k_0\Delta y} \tag{5.78}$$

For the upper boundary $n_x = 0$ and $n_y = 1$ and the boundary conditions become:

$$U_x\Big|^{Leon}_{ceil} = \frac{i}{k_0} Z \frac{\partial U_x}{\partial y} \tag{5.79}$$

$$U_y\Big|^{Leon}_{ceil} = \frac{i}{k_0} \frac{1}{Z} \frac{\partial U_y}{\partial y} \tag{5.80}$$

The solution takes the form of Eqs.(5.75,5.76) but with the following γ values:

$$\gamma^x_{ceil} = \frac{iZ}{k_0\Delta y} \tag{5.81}$$

$$\gamma^y_{ceil} = \frac{i}{k_0 Z\Delta y} \tag{5.82}$$

For case BC_3, expressions for the boundary conditions have already been found in Eqs.(5.60,5.61,5.73,5.74) for the left and right walls respectively, as also have been the corresponding γ in Eqs.(5.63,5.68,5.77,5.78). Again, the values must be set for the whole range of m values. This time the solution takes the form:

$$v_{m,1}^{n+1} = \frac{\gamma}{1+\gamma} v_{m,2}^{n+1} \tag{5.83}$$

$$v_{m,L}^{n+1} = \frac{\gamma}{1+\gamma} v_{m,L-1}^{n+1} \tag{5.84}$$

with v^{n+1} being U_x or U_y according to the polarization, and γ takes the appropriate values depending on the boundary domain and the polarization.

Chapter 6

Simulation Results and Validation: Parabolic Approach

Once the base upon this part of the simulator is based has been explained, the issues addressing the proper behaviour of the simulator in real scenarios must still be resolved and that is the main purpose of this chapter.

First of all it is worth comparing the simulator results with published theoretical waveguide models for tunnels. As it has been previously mentioned, the validity of the parabolic approach is comprised for small propagation angular ranges, so field configurations that are supposed to be stables throughout the tunnel are a perfect fit to assess the simulator performance.

Afterwards comparisons with published measurement data will be shown and some of the algorithm limitations will be exposed. Real scenarios imply several assumptions to be made and restrictions to be imposed in order to be able to use the ADI technique for EM prediction in tunnels.

In the next chapter simulations will be displayed with the results of a measurement campaign carried out by our group at L9 of Barcelona Metro, showing the degree of accuracy that can be expected from the developed work.

6.1 Validation of PE in Theoretical Scenarios

6.1.1 Dirichlet Waveguide

One of the examples presented in [54] are used to validate the developed ADI method with Dirichlet boundary conditions over the whole boundary domain. Suppose a PEC square waveguide with the following parameters:

1. Frequency $f = 3GHz$
2. Waveguide dimensions: $40\lambda \times 40\lambda$, 100m long
3. Source field: centred unit strength gaussian, $\sigma = 3.5\lambda$

4. Sampling parameters: $\Delta x = \Delta y = 0.4\lambda$, $\Delta z = 5\lambda$

Fig.6.1 shows the field at the starting transversal plane and the resulting solution 100m beyond. As the zero is forced at over boundary, see how the maximums of the solution are distributed symmetrically in the middle of the waveguide, with the only nulls being placed at the borders. A correct result for the here implemented method is obtained when compared against the analytical solution.

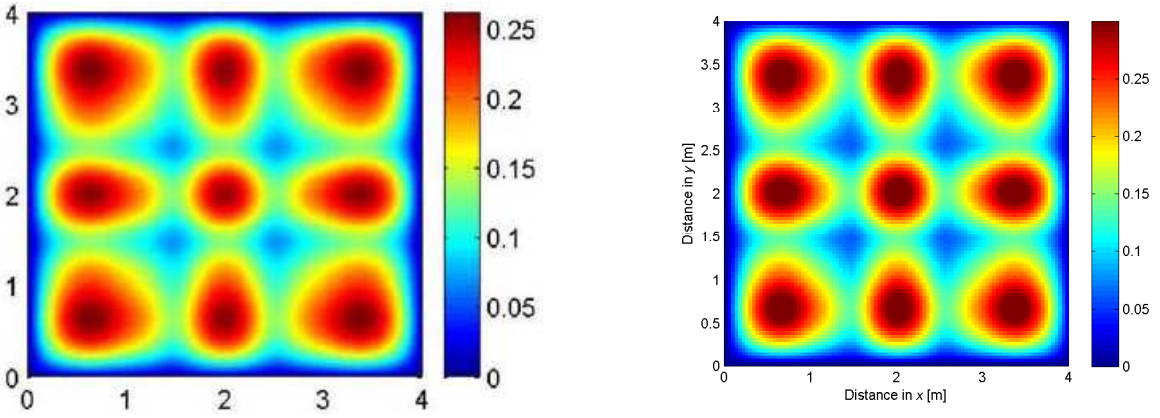

(a) Analytical solution taken from [54],Figure 4(a).

(b) Simulation results.

Figure 6.1: Dirichlet BC test.

6.1.2 Neumann Waveguide

The same example as in the Section 5.4.1 is run with Neumann boundary conditions over the whole boundary. Fig.6.2 shows the field at 100m from the source plane. See now that zeros along the boundary appear naturally at some points, but because the Neumann BC forces zero on the first derivative, some points still have some significant value at the borders. Again, see how the simulator correctly finds the solution when compared against the analytical case, with the symmetrically distributed field around the guide centre.

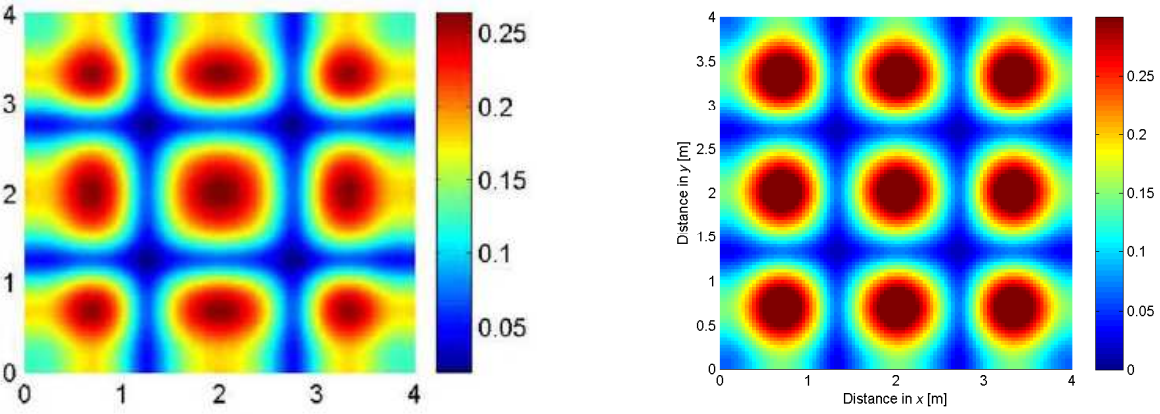

(a) Analytical solution taken from [54],Figure 4(c).

(b) Simulation results.

Figure 6.2: Neumann BC test.

6.1.3 Leontovich Hybrid Waveguide

To validate the correct application of the Leontovich boundary conditions an example presented in [31] and [54] is used. Suppose a rectangular guide such as that of the Fig.6.1.3, with 3 PEC walls and an impedance wall at $x = 4$.

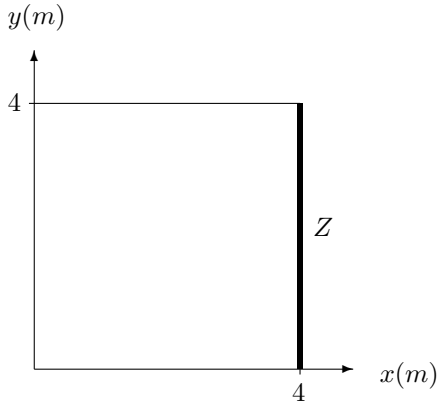

On the wall placed at $x = 0$ the boundary conditions are:

$$\frac{\partial E_x}{\partial x} = 0 \tag{6.1}$$

$$E_y = 0 \tag{6.2}$$

whereas for walls at $y = 0$ and $y = 4$ are:

$$E_x = 0 \tag{6.3}$$

$$\frac{\partial E_y}{\partial y} = 0 \tag{6.4}$$

Over the impedance wall placed $x = 4$ Leontovich boundary conditions must be applied. Cross-polarisation effects are neglected but, the guide being imperfect, small coupling between E-waves and H-waves occurs at the impedance wall. This means that, as waves pass down the guide, pure E-modes and H-modes are not stable and the field distribution changes throughout. Only a precise combination of both modes - $(E_x H)_{m,n}$ and $(E H_x)_{m,n}$ - propagates without substantial changes on its shape. Details about this modes are offered in [31].

Consider first that the y-component of $(E_x H)_{1,1}$ mode, shown in Figure 6.3a, propagates with the following parameters:

1. Frequency $f = 1GHz$
2. Wall impedance $Z = 0.3(1 + i)$
3. Sampling $\Delta x = \Delta y = 0.27\lambda$, $\Delta z = 11\lambda$
4. Waveguide length $z = 5km$

As it can be seen in Figure 6.3b, the field has passed down the guide preserving the field distribution with a notable resemblance to the theoretical solution. Field amplitude at $z = 1km$ agrees with results presented in [54].

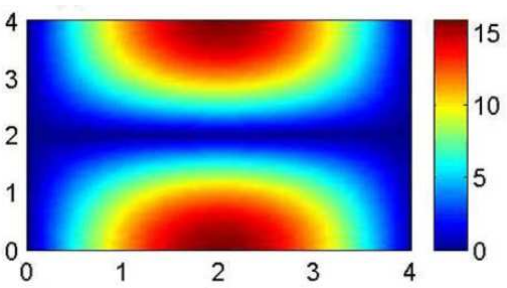

(a) Analytical solution at z=1km

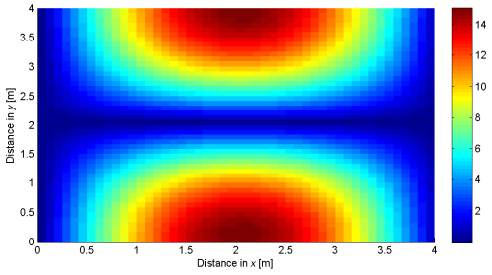

(b) Simulation results at z=1km

Figure 6.3: $E_x H_{11}$ case

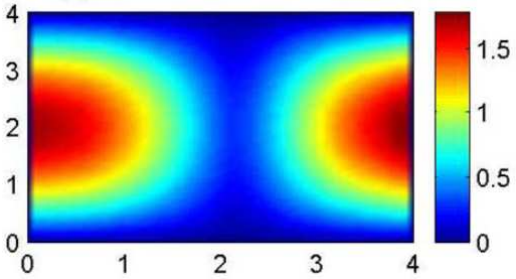

(a) Analytical solution at z=5km

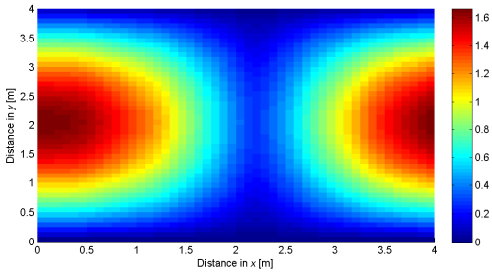

(b) Simulations result at z=5km

Figure 6.4: EH_{x11} case

The same example is repeated for the $(EH_x)_{1,1}$ x-component with wall impedance of $Z = 0.01(1+i)$ and waveguide length of $z = 1km$. This case gives more insight than the previous one as the field distribution has a maximum on the impedance boundary. In Figures 6.4a and 6.4b the initial and final transversal field configurations are shown. Again, the field pattern is preserved along the guide and close to the analytical solution, and the difference between theoretical and simulated modal attenuation factor is $2.64dB/km$.

A last remark must be done regarding the use of Leontovich BC. In a general case, modal field distributions are composed of a determined combination of sine and cosine functions. Depending on the mode, and talking in absolute value terms, a maximum or a zero will be placed at the boundary. In the former, and from the properties of sinusoidal functions, maximums have zero slope so the application of Leontovich BC will tend to impose a null along the boundary. The other case, where a zero is placed at the boundary, yields the same results. So, with a few exceptions such as the example in Fig.6.4, Leontovich BC forces field distributions to be confined inside the cavity, with nulls at the bounds and maximums distributed around the centre of the cavity.

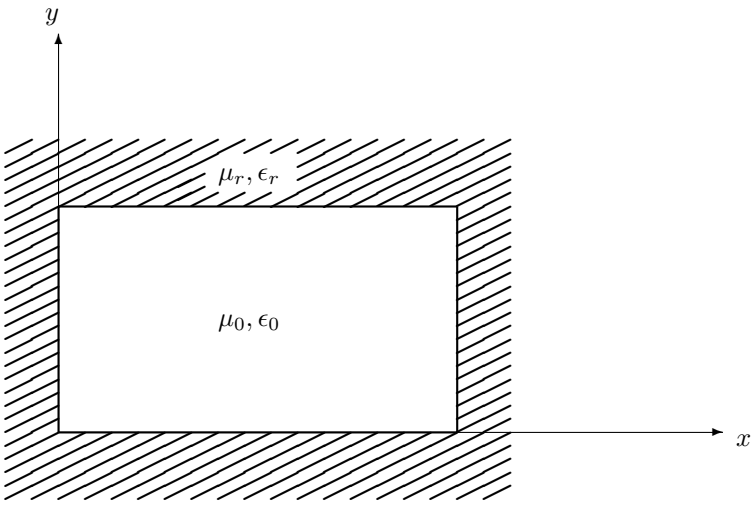

Figure 6.5: A rectangular dielectric waveguide

6.2 Theoretical Validation of ADI Simulations

6.2.1 Hybrid Modes in Rectangular Dielectric Waveguides

Several studies [31],[22],[34] have discussed that an exact analytical solution for hybrid modes in a rectangular dielectric hollow such as that of Fig.6.5 cannot be found. Approximate solutions have been found corresponding to the modes propagating inside the guide, although in the cited references different axial references were used. To ease the interpretation of the EM guiding phenomena and avoid confusion, the used expressions to find the field distributions for the horizontally - or x-polarised - modes (HE^x_{mn}) and vertically - y-polarised - modes (HE^y_{mn}) are listed below. Using the traditional transverse wavenumbers

$$k_x = \frac{m\pi}{a} k_y = \frac{n\pi}{b} \tag{6.5}$$

the approximate expressions for the modes can be summarised as follows:

1. Horizontally polarised hybrid modes: HE^x_{mn}

$$E_z \simeq 0 \tag{6.6}$$

$$H_z \simeq 0 \tag{6.7}$$

$$E_x = E_0 \sin(k_x x + \varphi_x) \cos(k_y y + \varphi_y) e^{-jk_z z} \tag{6.8}$$

$$H_x = 0 \tag{6.9}$$

$$E_y = 0 \tag{6.10}$$

$$H_y = H_0 \sin(k_x x + \varphi_x) \cos(k_y y + \varphi_y) e^{-jk_z z} \tag{6.11}$$

with phase constants φ_x and φ_y depending on the mode number as follows:

$$\varphi_x = \begin{cases} \pi/2, & \text{if } m \text{ odd} \\ 0, & \text{if } m \text{ even} \end{cases}$$

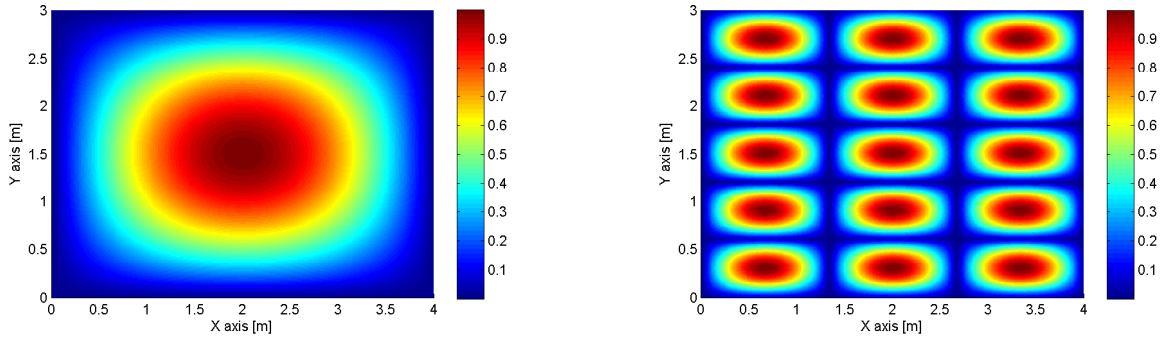

(a) The HE_{11}^x x-component

(b) The HE_{35}^x x-component

Figure 6.6: The x-field components of two hybrid modes.

$$\varphi_y = \begin{cases} \pi/2, & \text{if } n \text{ even} \\ 0, & \text{if } n \text{ odd} \end{cases}$$

2. Vertically polarised hybrid modes: HE_{mn}^y

$$E_z \simeq 0 \tag{6.12}$$

$$H_z \simeq 0 \tag{6.13}$$

$$E_x = 0 \tag{6.14}$$

$$H_x = H_0 \cos(k_x x + \varphi_x) \sin(k_y y + \varphi_y)\, e^{-jk_z z} \tag{6.15}$$

$$E_y = E_0 \cos(k_x x + \varphi_x) \sin(k_y y + \varphi_y)\, e^{-jk_z z} \tag{6.16}$$

$$H_y = 0 \tag{6.17}$$

$$\tag{6.18}$$

with phase constants φ_x and φ_y depending on the mode number as follows:

$$\varphi_x = \begin{cases} 0, & \text{if } m \text{ odd} \\ \pi/2, & \text{if } m \text{ even} \end{cases}$$

$$\varphi_y = \begin{cases} 0, & \text{if } n \text{ even} \\ \pi/2, & \text{if } n \text{ odd} \end{cases}$$

As an example, the field distribution of the transversal x-components - note that the longitudinal and y-transversal are zero - for the HE_{11}^x and HE_{35}^x are presented in Fig.6.6. The tunnel dimensions are $a = 4m$ and $b = 3m$.

The theoretical expressions for attenuation of the modes are given in the previous references. To assess the validity of the simulator, modes $HE_m^y 1$ for $m = 1, ..., 9$ were propagated for a distance up to $z = 500m$ with the implemented ADI algorithm. Correct results were obtained - see Table 6.1 - as modes preserved the same configuration throughout the tunnel and the attenuation was similar to the expected theoretical values.

Mode	$\alpha_{theoretical}$ [dB/km]	$\alpha_{simulation}$ [dB/km]
HE^y_{11}	0.0726	0.0704
HE^y_{12}	0.2561	0.2352
HE^y_{13}	0.5622	0.5422
HE^y_{14}	0.9907	0.9788
HE^y_{15}	1.5416	1.5427
HE^y_{16}	2.2150	2.2226
HE^y_{17}	3.0107	3.0178
HE^y_{18}	3.9289	3.9362
HE^y_{19}	4.9695	4.9865

Table 6.1: Attenuation comparison for $HE^y modes$

6.2.2 Propagation in Rectangular Tunnels

After obtaining good simulation results with theoretical cases, the next step is observing its performance in a more realistic scenario. To this end, the published measurement results presented in [16] and [24] are used as a reference again. The simulation parameters are the same as in Section 4.1. This time, however, results are greatly improved as shown in Fig.6.7 and Table 6.2. The deviation both for the attenuation constant

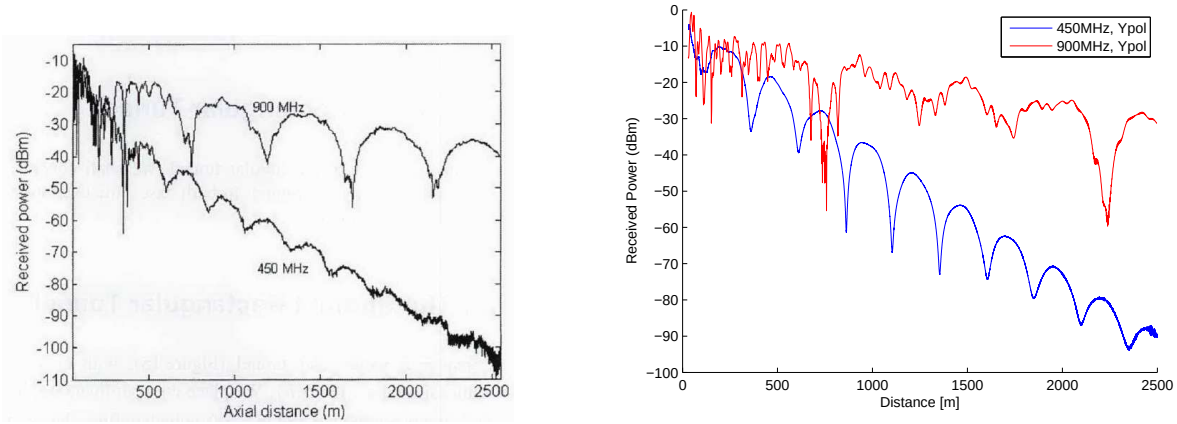

(a) Measurement results taken from [16],Figure 18.

(b) Simulation results.

Figure 6.7: Parabolic simulation results at 450MHz and 900MHz.

and the phase constant has decreased notably, as the good behaviour presented demonstrate. To obtain the initial fields for the PE technique, a spectral simulation is run with the equivalent rectangular tunnel cross section for the first few meters, until a certain point is reached and the propagation is switched to the PE. Details about how the switching point is chosen are presented on the following section

Therefore the modal expressions found in the previous section can be used to here to give some insight on the effects occurring inside the tunnel.

Case	Attenuation [dB/Km]	Pseudo-periodicity [m]
Measurements 450MHz	33	240
Simulations 450MHz	33.3	248
Measurements 900MHz	8.5	486
Simulations 900MHz	9.6	500

Table 6.2: Parameter comparison between measurements and simulations

6.3 Computational Issues for ADI-PE

On top of the advantages that represent higher accuracy and easier application of boundary conditions with the parabolic technique respect to the spectral method, there is also the benefit of allowing longer tunnel studies that would otherwise become too costly. The simple implementation chosen for ADI - even if faster procedures have been described and successfully tested in [55],[56] for instance - greatly enhanced the time needed for EM prediction.

First, recall that transversal matrices used during ADI simulations only account for points belonging to the inner part of the tunnel. So, if the spectral simulator works with $M \times L$ matrices, where usually $L = M$, ADI works with non-squared matrices such that $(M_{ADI}, L_{ADI}) < (M, L)$. Commonly, matrix dimensions reduced to 50% of the original matrix size, so to ease the analysis consider ADI square matrices of $M_{ADI} \times M_{ADI}$.

The procedure described in Section 5.3 has an operational order of $O\left(M_{ADI}^2\right)$, which is smaller than that found for the spectral technique even if the same matrix dimensions - $M_{ADI} = M$ - are considered for both methods. Fig. 6.8 highlights this feature, considering $M_{ADI} = 0.7M$. See how the number of operations decreases by almost 40%. This notable reduction is very positive, and it must also be noted that time spent to jump from one technique to the other is negligible.

On the other hand, memory resources are also less demanding due to the aforementioned transversal matrices size reduction, but also because of the nature of ADI techniques. Because they are applied to model slowly varying processes along one dimension, the total number of sampling points along that dimension can be reduced. For instance: for fields sampled every $\lambda/4$ along the transversal dimensions, the longitudinal sampling can be made every $\Delta z^{ADI} = \lambda, 5\lambda$ when spectral simulations sampled the longitudinal axis every $\Delta z^{spectral} = \lambda/4, \lambda$. ADI only uses two $M_{ADI} \times L_{ADI}$ matrices - one for each transversal field component - and two $M_{ADI} \times N_{ADI}$ arrays for longitudinal field storage, so the total required memory space is:

$$\left(2M_{ADI}^2 + 2 \times 2 \times M_{ADI} N_{ADI}\right) bytes \tag{6.19}$$

Fig. 6.9 shows the difference between the required memory resources of spectral and ADI techniques, considering $\Delta z^{ADI} = 5\Delta z^{spectral}$. Memory requirements are down to very reasonable $10MB$ when all data are stored, or to $5MB$ when data are decimated, when large simulations are run. Adding to that fact, the time saved by avoiding hard disk access while working with fast-access memory may be the top reason to root for a mixed spectral-ADI approach. That was one of the hardest points with full-spectral simulations: $1000m$-long simulations at large frequencies, as those presented in Section 6.2.2, were difficult to perform

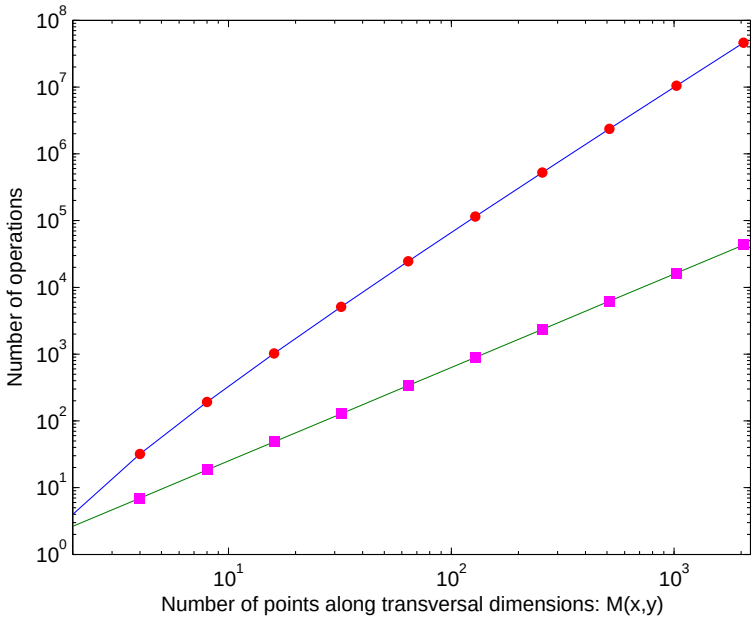

Figure 6.8: Simulations complexity as a function of the transversal dimensions. ADI case.

without ADI approach. Also, computer requirements are less demanding, allowing for common use PC or laptops to run simulations without much troubling.

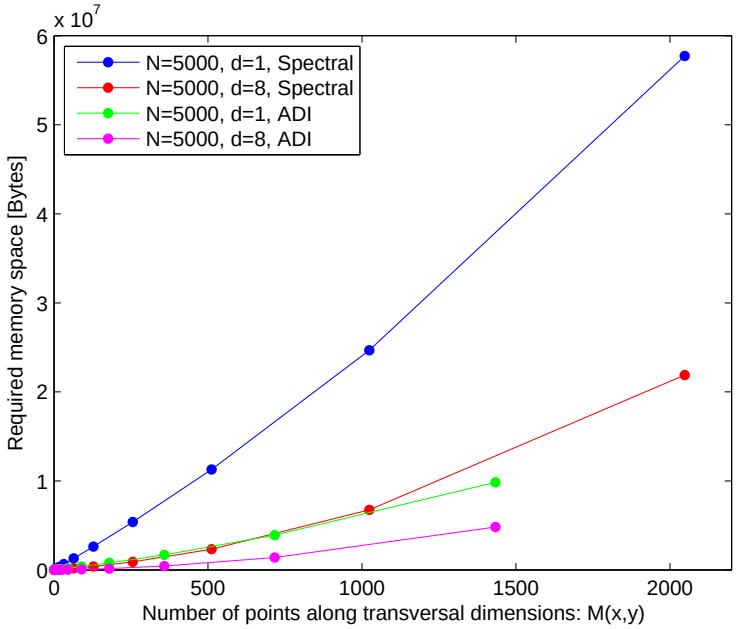

Figure 6.9: Memory requirements as a function of the transversal dimensions. ADI case.

Chapter 7

Propagation in Tunnels: A Combined Spectral-PE Approach

The previous chapters have been devoted to the performance analysis of two different approaches used for modelling EM propagation in tunnels: the spectral method and the parabolic equation. So far, it has been shown that both techniques are able to provide meaningful results in certain situations and that their strong points lie in complementary areas.

Thus, the combination of both techniques to cover the full range of distances along the tunnel comes naturally. This chapter will introduce the criterion used to combine both techniques and results will immediately follow, comparing the approach predictions and the measured path losses of a set of measurement campaigns carried out at Metro L9 in Barcelona, Spain.

For all the examples presented in this chapter, path loss results both from measurements and simulations will be normalised to the free space fall-off in the meters close to the source.

7.1 The Hybrid Spectral-PE Approach

After working intensively with spectral techniques, it was clear that some adjustments had to be made in order to reduce the simulation time required for tunnel simulations at 5.8GHz when long distances were analysed. Somehow also, problems with the application of BC had to be overcome to provide accurate results at long distances.

On the other hand, contributions from Popov [50] and Martelly [54, 57] proved the usefulness of parabolic equation techniques for EM predictions in tunnels, although it was singled out that the close-to-transmitter region had to be obtained by other means, as the conditions imposed for the parabolic regimen were not fulfilled at such short distances.

Hence, it is only a matter of meeting an optimal combination between the techniques detailed in the previous sections to overcome their respective shortcomings. In fact, [50] uses a geometrical optics method for the first few meters, although it does not offer details on the criterion followed to switch between

techniques. Here, the main point is finding the appropriate switching point that maximises the trade-off between time, resources and accuracy.

7.1.1 Algorithms Advantages and Limitations

Spectral methods are specially suited in complex scenarios such as tunnels because the whole geometry of the cavity is analysed integrally. However, there are disadvantages too. The following list summarises both positive and negative aspects of spectral methods:

- Advantages

    1. Integral treatment of the cavity and the surrounding area.
    2. Two-domain information of the EM phenomena occurring in the tunnel.
    3. Able to model properly the near-to-the source fields behaviour.
    4. Obstacles or cross-section changes easy modelling.

- Disadvantages

    1. Difficult application of polarimetric BC.
    2. Inaccurate long-distance path loss prediction.
    3. Intensive computational load at high frequencies.

As for PE methods:

- Advantages

    1. Integral treatment of the cavity.
    2. Accurate long-distances modelling.
    3. Easy application of polarimetric BC.
    4. Low computational load.

- Disadvantages

    1. Initial field plane definition must be obtain using external methods.
    2. Initial fields must be slow-varying in one direction.
    3. Obstacles or cross-section changes are hard to model.

From the description made above it seems clear that both techniques are a good fit to be paired together: both deal with the whole tunnel cavity and while the former properly models the transmitter short range, the latter is more adept to be used far from it. The fact that irregularities at the tunnel walls have large impact near the transmitter and are much less significant in the far region is also a good match. For last, after detailed analysis of the near-field region of the transmitting antenna is performed with the spectral technique, computational effort is eased by means of the PE in the long distance. Table 7.1 summarizes the most important advantages and shortcomings of each technique.

	Spectral	Parabolic
Distance range	near to the source	far from the source
Boundary condition	difficult to apply	Leontovich approach
Initial field set-up	from antenna currents	need for external set-up
Tunnel modelling	adaptable to obstacles	constant cross-section
Computational load	high	low

Table 7.1: Spectral and Parabolic techniques comparison

7.1.2 The Angular Criterion

This section describes the criterion employed to determine when to switch from spectral propagation to PE propagation.

As it has been documented in [47] and [48], the condition for the parabolic regimen accurate modelling requires the propagation to rely heavily in the components comprised between $\pm 15°$. In Section 3.2.3, the number of points from the spectrum centre had been related to the propagation angle θ_i (Eq.3.22):

$$v = \frac{L\Delta x}{\lambda} \sin \theta_i \tag{7.1}$$

where L is the total number of points along the x-axis and Δx the sampling distance. From here, it is straightforward to find the maximum displacement that a component can have in the APWS in order to belong to the parabolic regimen. If the angle θ_i is bounded to $\theta_{max} \leq \pm 15°$:

$$v_{max} = \frac{L\Delta x}{\lambda} \sin \theta_{max} \simeq \frac{L\Delta x}{4\lambda} \tag{7.2}$$

The same can be said along the y-directions and, considering identical sampling conditions in both directions, it results in a circular pattern around the centre of the spectrum. The procedure consists in computing the amount of energy accumulated inside the margin by a v_{max}-radius circumference around the centre of the spectrum respect to the total amount of energy contained across the whole spectrum. Afterwards, this magnitude is compared with a certain threshold γ. Denoting SPE as the spectrum components propagating with angles $\theta_{max} \leq \pm 15°$, it would look as follows:

$$\zeta_{PE} = \sum_{l \in SPE} \sum_{m \in SPE} \left[|APWS_x(x_l, x_m)|^2 + |APWS_y(x_l, x_m)|^2 \right] \tag{7.3}$$

$$\zeta_{total} = \sum_{\forall l} \sum_{\forall m} \left[|APWS_x(x_l, x_l)|^2 + |APWS_y(x_l, x_m)|^2 \right] \tag{7.4}$$

Note that the quantities written above are not energy, because they are the square modulus of the spectral components, but the ratio between them is an equivalent magnitude as both are expressed in the spatial frequency domain. Thus, γ being the threshold, the condition that must be checked while the wavefront progresses in the spectral method is:

$$\frac{\zeta_{PE}}{\zeta_{total}} \overset{?}{\geq} \gamma \tag{7.5}$$

When the condition is fulfilled, the propagation method is switched from spectral to PE. Note that, from this point on, as mentioned in the advantages and disadvantages in the previous sections, fields outside of the

cavity are not further propagated, thus reducing the arrays size and memory requirements. The information loss - corresponding to scattered fields in the external vicinity of the boundary - is not important at this stage because main contributions are already propagating along the tunnel longitudinal axis. Otherwise the criterion would not be fulfilled.

It still remains to be seen which value is a good fit for the threshold. For this point, an experimental study rather than a theoretical approach has been undertaken.

7.1.3 Spectral-PE Simulations Results

Curves of Fig.6.7 in Section 6.2.2 have been obtained applying the procedure detailed above: the first tunnel stretch is simulated with the spectral method periodically checking if the threshold is reached and, once it does, the rest of the tunnel is run with the PE method. The threshold in that case has been set at 95%.

After running many simulations, the evolution of the quotient in Eq.7.5 is always similar to that of Fig.7.1. In this case, a large rectangular tunnel is simulated with the transmitted shifted $1m$ from the centre of the tunnel, and transversal fields are stored every $10m$.

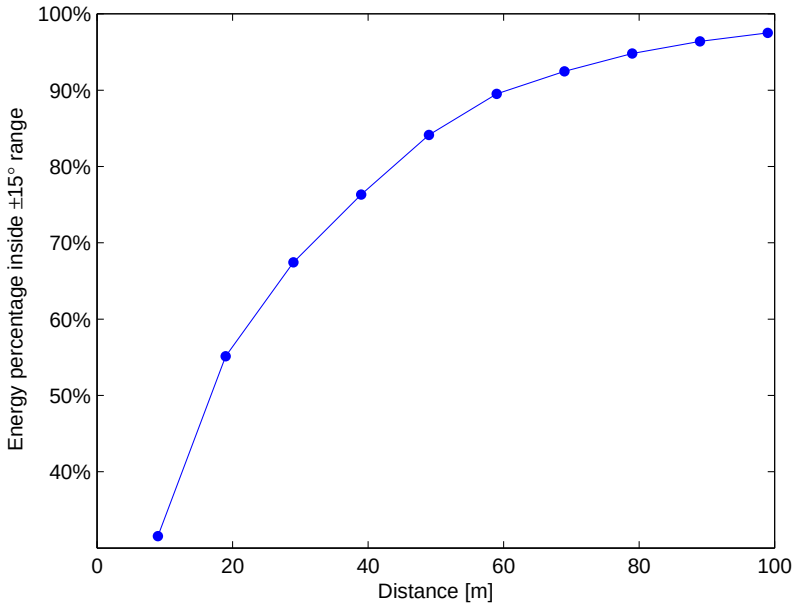

Figure 7.1: Energy inside the $\pm 15°$ range versus distance.

Some tests were made varying the transmitter position or its radiation pattern, but the shape of the curve remained relatively constant for all analysed scenarios, the only point changing being the quickness - or distance - with which the energy is gathered inside the $\pm 15°$ range with high values. After that, it is interesting to see when does the combination between spectral and PE methods converge. To address this issue several simulations are run varying the switching point. The same rectangular tunnel as above is simulated for a total of $600m$ and four different split points: $10m$, $30m$, $50m$ and $70m$. Results for the first $100m$ are presented in Fig.7.2, with blue lines being the spectral simulations and red lines PE simulations.

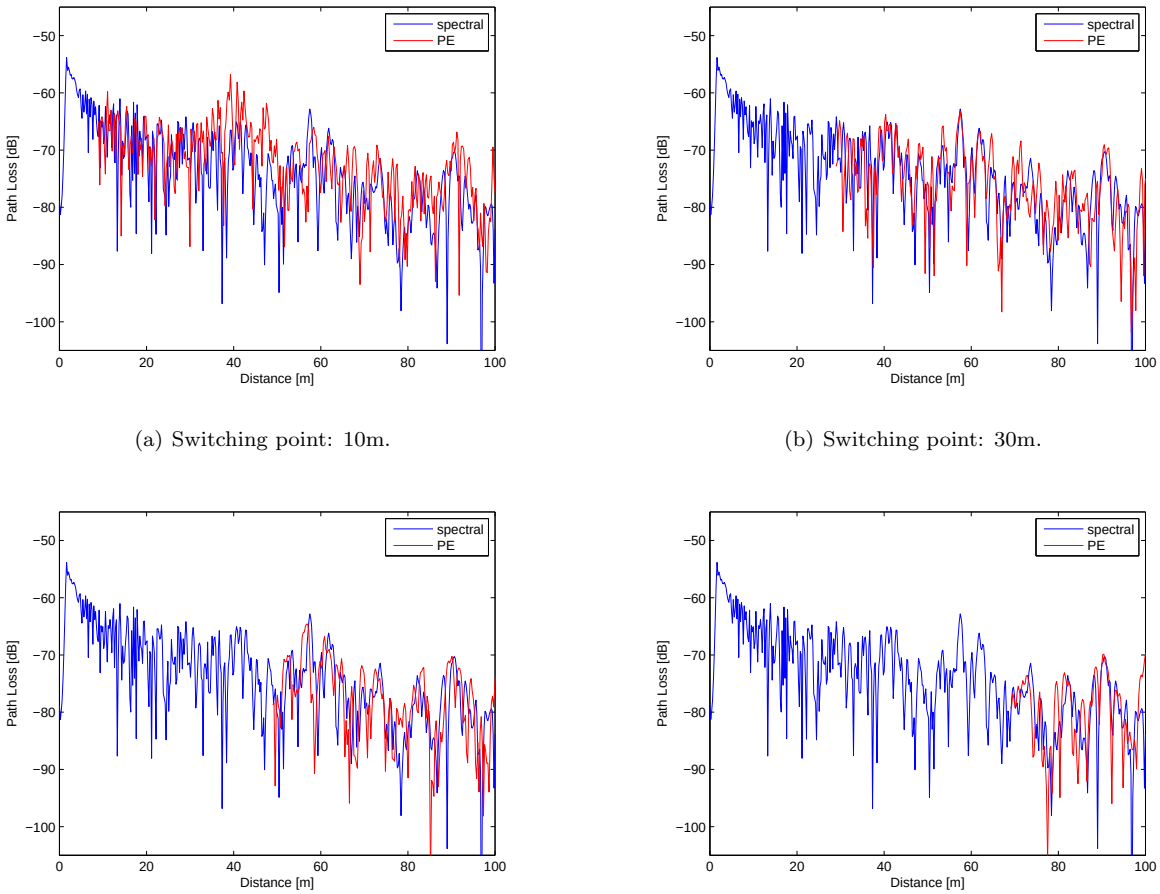

(a) Switching point: 10m.

(b) Switching point: 30m.

(c) Switching point: 50m.

(d) Switching point: 70m.

Figure 7.2: Combination between spectral and PE simulations at different points.

See how PE simulations follows quite accurately the pattern predicted by spectral simulations for all cases up to the $100m$ mark. It also shows that both techniques are compatible to work together mainly because, just as geometrical optics techniques also do, they deal with the wavefront as a decomposition of rays or plane waves equivalently.

Taking a look at the first $100m$ in Fig.7.2, it would seem logical start using the PE technique as soon as possible in order to enhance the management of computational time and resources, but if the full distance span of $600m$ is analysed, simulation shows that, the combination being made at $10m$, the trace is very *noisy*, in the sense that many deep, fast oscillations are present along the path loss curve, making the analysis harder. As the combination is retarded the traces become clearer. An example of such is represented in Fig.7.3, where combinations at $10m$ and at $70m$ are compared.

Hence, recalling the results shown in Fig.7.1 and seeing the small differences obtained between setting the switching point at $30m$ or later, it seems that, percentage-wise, around 80% of energy contained inside the PE margin is a good enough threshold to start working with the PE technique at L9 tunnels.

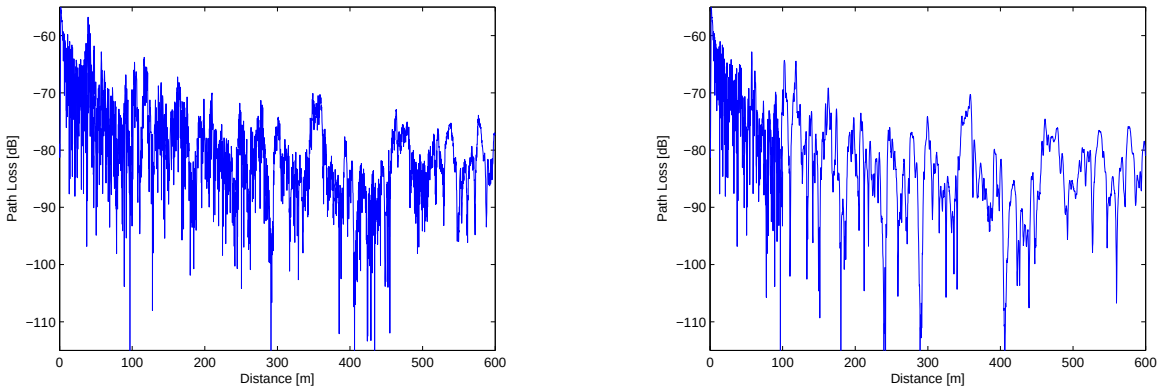

(a) Switching point: 10m.

(b) Switching point: 70m.

Figure 7.3: Full view of spectral-PE simulations.

7.2 Barcelona Metro L9 Measurement Campaigns

Some details have already been mentioned about Metro L9 service. It accounts for one of the most challenging projects on urban development nowadays, and its impact on the transport service of the Barcelona metropolitan area cannot be ignored.

The tool developed during this thesis aims to be useful for the radiocommunication planning of the different services of L9. Due to the high-standard requirements of the service and the Automatic Train Control system, a safe, reliable and efficient planning is of paramount importance. During the thesis development, several measurement campaigns were carried out that greatly helped to add new elements to the simulator and contrast the obtained results.

Most of the information described in subsequent sections has already been published in [58],[59] and [60] referring to the environment and measurement setup description. Here, a brief introduction of the measured tunnels is given to provide some consistent background to the results presented in this section.

7.2.1 Metro L9 Environment Description

As it has been shown in Section 3.2.1, L9 tunnel has a horizontally-split circular shape with diameter comprised between $9m$ and $12m$, depending on the tunnel stretch. The walls are made of steel-fiber reinforced concrete and are quite smooth except for the different cables, pipes and boxes that account for power and communications supply. This objects have a regular longitudinal pattern and, in the boxes case, are placed periodically along the tunnel. This usually is corresponded with non-random scattering, favouring certain directions of propagation instead. The fact that, prior to the measurement campaigns, no random scattering was expected, did not have much significance for the spectral simulations, as it has been shown that this aspect can be easily taken into account, but it could have had for the PE case because of the considerable size of this objects, even if under the $\pm 15^\circ$ range main contributions propagate almost parallel to the tunnel longitudinal axis.

Some significant data related with L9 tunnels is summarised in the following points:

- Tunnel diameter: $9m - 12m$.
- Upper cavity dimensions: $9.94m$ radius x $4.77m$ high.
- Lower cavity dimensions: $9.54m$ wide x $4.65m$ high.
- Wall dielectric constant: $\epsilon_r = 12$
- Wall conductivity: $\sigma = 0.01S/m$
- Tunnel curvature radius (when appropriate): $240m$
- Transmitting and receiving antennas: Patch antennas placed $2m$ above ground and shifted between $1m - 3m$ from the tunnel axis, depending on the measurement set.

Although the spectral simulator is prepared to deal with the whole L9 cross-section geometry, no measurements could be taken that allowed to observe the EM behaviour of one cavity while transmitting from the other one. Thus, to ease the analysis, only half section was simulated - whether it was upper or lower - each time. This also facilitated the integration of PE simulations, keeping the number of points relatively manageable and not having to introduce new boundary conditions in the middle of the cavity corresponding to the intermediate platform.

(a) L9 upper cavity.

(b) L9 lower cavity.

Figure 7.4: L9 tunnel environment.

Some pictures of the tunnels are shown in Fig.7.4, where two semi-curved paths are shown to illustrate both the straight and curved paths. The presence of the mentioned items next to the walls can be appreciated in the pictures, as well as the large tunnel curvature radius at the end of the depicted tunnel stretch. See the arched ceiling - almost a complete semi-circular profile - in the upper cavity and the horizontal ceiling with partially-curved lateral walls in the lower cavity. It can be seen that the upper cavity area - $38.8m^2$ - is a bit smaller than that of lower cavity - $44.36m^2$.

As the PE technique has only been implemented to deal with rectangular cross-sections, it is necessary to find an equivalent rectangular cross-section for both upper and lower cavities. Unfortunately, the technique

employed in [16] and [24] of measuring the fundamental mode attenuation at the working frequency cannot be employed here because the tunnel did not offer a straight, long enough stretch to measure it and adapt the equivalent rectangular tunnel dimensions to match that attenuation. As [37] proved, arched tunnels can be analysed using rectangular sections with the same cross-sectional area as the original one. Fig.7.5 presents the real and the simulated tunnels for both cavities. The dimensions of the equivalent rectangular cross-sections are summarised in Table 7.2, as well as the employed terminology for antenna polarisation during the measurement campaigns.

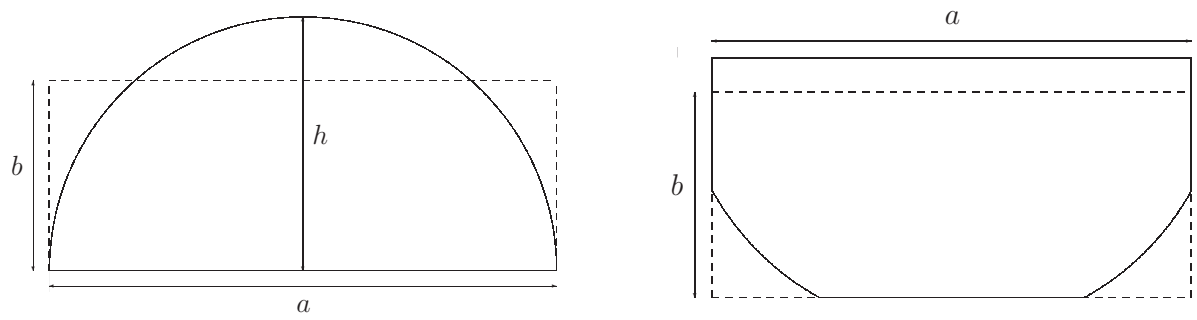

(a) L9 upper tunnel cross-section and its rectangular equivalent.

(b) L9 lower tunnel cross-section and its rectangular equivalent.

Figure 7.5: L9 simulated cross-sections.

Tunnel	a[m]	b [m]
Upper Straight Tunnel (UST)	9.94	3.91
Lower Straight Tunnel (LST)	9.54	4.36
Lower Curved Tunnel (LCT)	9.54	4.36
Horizontal polarisation	Hpol, parallel to ground	
Vertical polarisation	Vpol, orthogonal to ground	

Table 7.2: Equivalent tunnel dimensions and terminology

7.2.2 Validation of Spectral-PE Simulations in Real Scenarios

Once the environment in which the measurements took place has been presented, results are shown in this section. Assessment of measured and simulated path losses is given, focusing on the comparison between experimental and simulated curves.

Even if a total of three long campaigns have been carried out, only three specific scenarios are going to be analysed. There is a variety of reasons for this. First, because L9 was being constructed or being finished at the moment the measurements took place, not all the desired scenarios could be measured under proper conditions, or measured at all. Secondly comes the limitations of the developed algorithms: only the spectral technique can deal with the different options L9 tunnels present, as the PE technique here implemented is limited to straight tunnels with homogeneous cross-section.

Ideally, the interest should be focused on long straight or curved stretches because of the impact the different objects along the tunnel boundaries have on the short range. As a consequence, the three analysed situations are an upper straight tunnel stretch, a lower straight tunnel stretch and a lower curved tunnel stretch, the latter being simulated fully with the spectral method. The upper curved tunnel stretch could not be measured, so there is no reference to compare against and this case is omitted from these results.

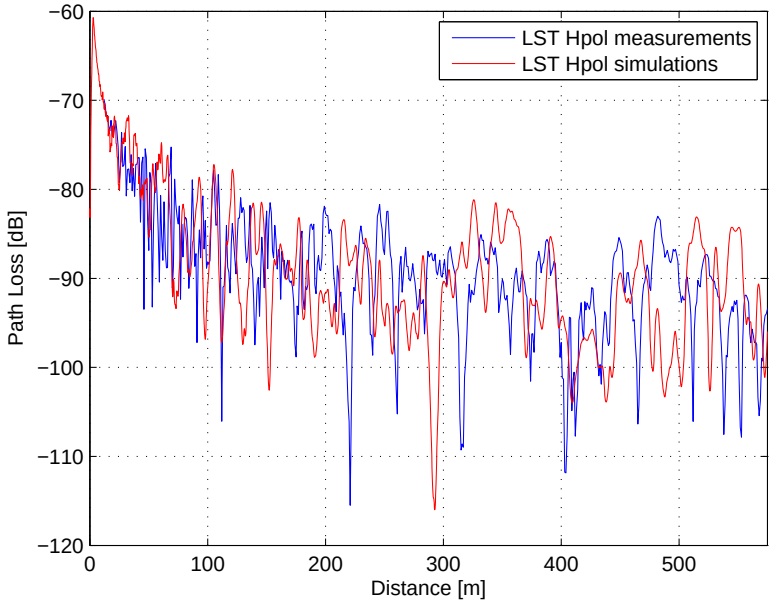

Figure 7.6: L9 comparison. LST H polarisation.

Figs.7.6 and 7.7 compare the results of measurements and simulations for the Lower Straight Tunnel (LST), the former with H polarisation and the latter with V polarisation. Simulations were run using the equivalent-area rectangular tunnel of Fig.7.5b. The switching distance between spectral and parabolic techniques was $r = 60m$, where more than a 87% of the energy was contained inside the $\pm 15°$ angular propagation range. Once the free space behaviour disappears, losses are small, as the corresponding the fundamental mode theoretical attenuations in the equivalent rectangular LST tunnel for H and V polarisation show: $\alpha_H = 0.01dB/100m$ and $\alpha_V = 0.05dB/100m$. In this case the difference is not much noticeable but this is due low attenuations corresponding to such high - $5.8GHz$ - frequencies. The measured scenario does not allow to identify the lower order modes as in the experiment from Molina-García-Pardo et al. [24], which would be very interesting, because the distance between transmitter and receiver required to extinguish higher order modes at this frequency range exceeds by large the available straight tunnel stretches at L9.

Measurements and simulations in Fig.7.6 for horizontally polarised case have similar trends and match pretty well for the whole analysed stretch, although several local differences can be appreciated. Nevertheless, this was expected in light of results presented in Chapters 4 and 6. Similar comments apply for the vertically polarised case of Fig.7.7: there is a first region where both measurements and simulations fall-off is that of free space, with a noticeable decay up to 100m from the source. From that point on, decay occurs at a much slower pace. The modal richness is still present, while fast-fading vanishes as expected as the distance

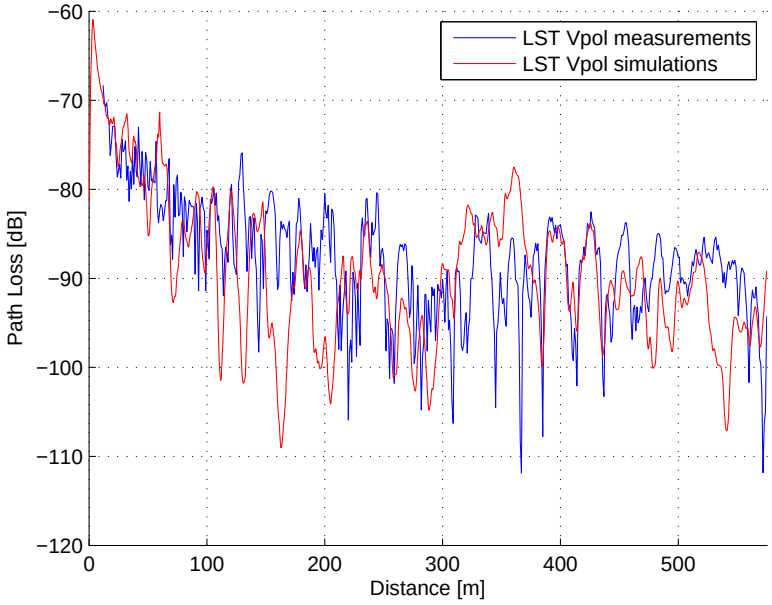

Figure 7.7: L9 comparison. LST V polarisation.

between transmitter and receiver increases. Some peaks and valleys are unmatched between measurements and simulations though, but the overall attenuation is well predicted.

Figs.7.8 and 7.9 show a similar study at the Upper Straight Tunnel half (UST) for both polarisations. Larger differences in the path loss shape are expected in this case because of the difference between the semi-arched real tunnel cross-section and the equivalent-area rectangular profile used in simulations. Also, the fundamental mode theoretical attenuations for the UST tunnel are small and do not differ much: $\alpha_H = 0.01dB/100m$ and $\alpha_V = 0.07dB/100m$In spite of it, the simulator is able to make correct predictions for the horizontal polarisation, but the behaviour is quite worse for the vertical case. Fast fading lasts longer than in the LST tunnel, due to the arched ceiling forcing larger number of reflections. The Hpol case follows a similar trend to that of LST until the 350m mark: a free space fall-off first, a slow decay afterwards. Afterwards though, a significant drop occurs that that the simulator successfully predicts. For the Vpol case, the drop occurs later, at 400m approximately, but this time the difference between measurements and predictions is significant in the last stretch. As in the LST scenario, partially success is achieved even if peaks and valleys are mismatched at certain points of the tunnel.

Trying to add some numerical consistency to the previous comments for both tunnels and polarisations, an analysis frequently used in mobile communications environments is carried out [61]. This analysis substitutes the comparison against modal attenuation used throughout the thesis because of the high frequency and relatively short distances used during measurements. Root mean square values (RMS) for measurements and simulations of Figs.7.6,7.7,7.8,7.9 are obtained filtering both curves with a moving average window of length 40λ. Once the difference in absolute value between both RMS curves is computed, mean μ and standard deviation σ are found to numerically characterise the simulator's performance. Results are presented in Table 7.3.

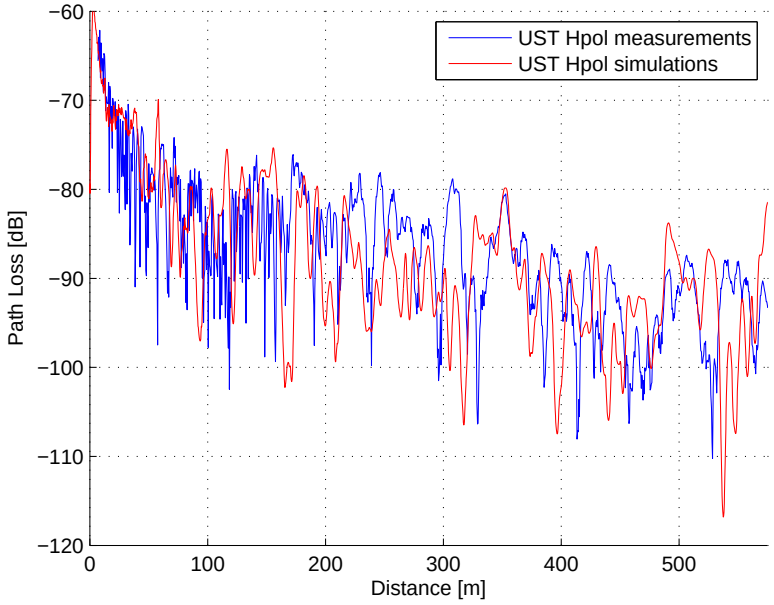

Figure 7.8: L9 comparison. UST H polarisation.

Tunnel	LST		UST	
Polarisation	Hpol	Vpol	Hpol	Vpol
μ [dB]	5.92	5.52	6.06	7.83
σ [dB]	7.55	7.25	7.66	10.78

Table 7.3: Numerical comparison between measurements and simulations for straight L9 tunnels. Window length: 40λ.

As it can be seen, simulator predictions have an average difference of $6dB$ respect to measurements during the 600m-long analysed stretches; standard deviation also have large values. The obtained accuracy is worse than that presented by Didascalou et al. [20]. There are several reasons to that: the frequency of analysis has a much smaller wavelength, which leads to larger presence of fast-fading throughout the tunnel that can be hardly predicted even if the tunnel is modelled accurately. Related with the previous one, smaller attenuation accounts for higher number of modes involved throughout the measured propagation path. See the difference between path loss curves of Figs. 4.3a and 4.4a and those presented in this section, how the bouncing is smoother and clearer in the former ones even though the distance span is different, larger for the current figures. At $5.8GHz$, the higher peaks and deeper valleys predicted by the simulator may be interpreted as an indicator that some higher order modes are missing, thus allowing the possibility of purer constructive and destructive interferences as the large bouncing dynamic range of the previous figure suggests. The difference at these mismatched peaks and valleys largely contribute to increase the values of standard deviation presented in Table 7.3. Another source of error is that it was difficult to model the irregular wall obstacles because tunnel works were not finished and sizes of the different boxes attached to the tunnel boundaries and obstacles - such as metallic scaffoldings, railway end structures - were considerable.

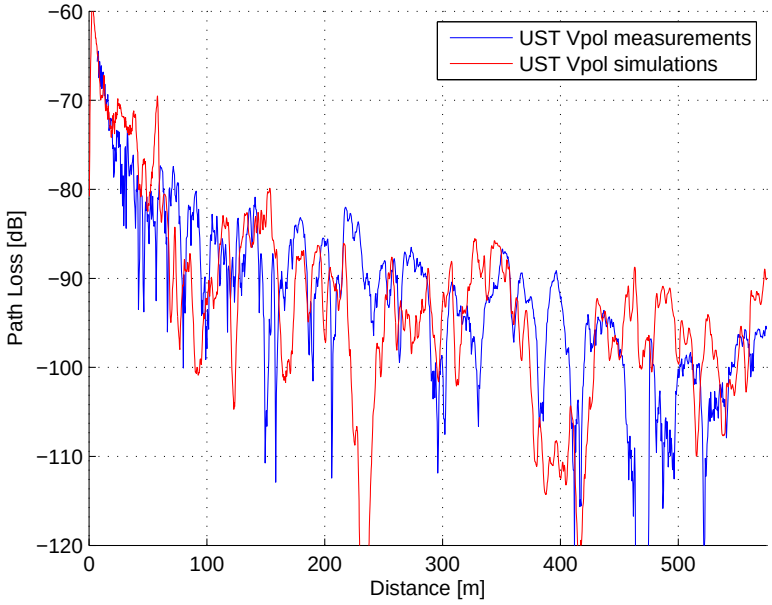

Figure 7.9: L9 comparison. UST V polarisation.

If the window size is increased to a metric span comparable to the one used in Didascalou analysis [20] - between 12 and 20m, depending on the frequency - accuracy improves. In this case a window of 300λ or $15m$ at $f = 5.8GHz$ is employed and used henceforth. Results are those of Table 7.4, which show a much better accuracy except for the UST Vpol case, that is still quite biased. The other cases, however, offer results that are more in line with the degree of precision presented in Chapters 4 and 6. This window size also fits better with the parabolic approach, that relies on the fact that the physically modelled process must be slow-variating along one of the dimensions, which corresponds to the longitudinal axis in this analysis. Partially filtering fast variations helps improving the accuracy provided by this technique. In fact, if Martelly results [54],[57] are analysed, few fast-fading references are used to be compared against and even in those cases the predictions provided by their ADI approach are slow-varying along the longitudinal direction.

Tunnel	LST		UST	
Polarisation	Hpol	Vpol	Hpol	Vpol
μ [dB]	3.58	4.16	3.58	6.19
σ [dB]	4.6	5.00	4.17	8.24

Table 7.4: Numerical comparison between measurements and simulations for straight L9 tunnels. Window length: 300λ.

Another interesting and measured scenario consisted of a short curved path of 160m-long on the Lower Curved Tunnel (LCT). A longer tunnel stretch would have been of major interest because of the border between Line of Sight (LoS) and nLoS situations, but those measurements could not be carried out. For the scenario, it was a right-hand bend with curvature radius equal to 280m. The rails were placed on the left

half of the tunnel, just after an underground station. Both transmitting and receiving antennas were placed over the rails, maximising the LoS distance and emulating the most likely deployment scenario for a real case. Larger losses are expected due to the curved path and the higher number of reflections occurring at the tunnel walls. Measurements were taken at both H and V polarisations and compared to simulations. Recall that, because no bended tunnels can be analysed using ADI simulator, results below have been obtained only with the spectral technique. Because the length of the curved stretch was not very long, it did not imply any computational issue. The tunnel is modelled as 10 sections of 16m, with rotations of 3° between sections.

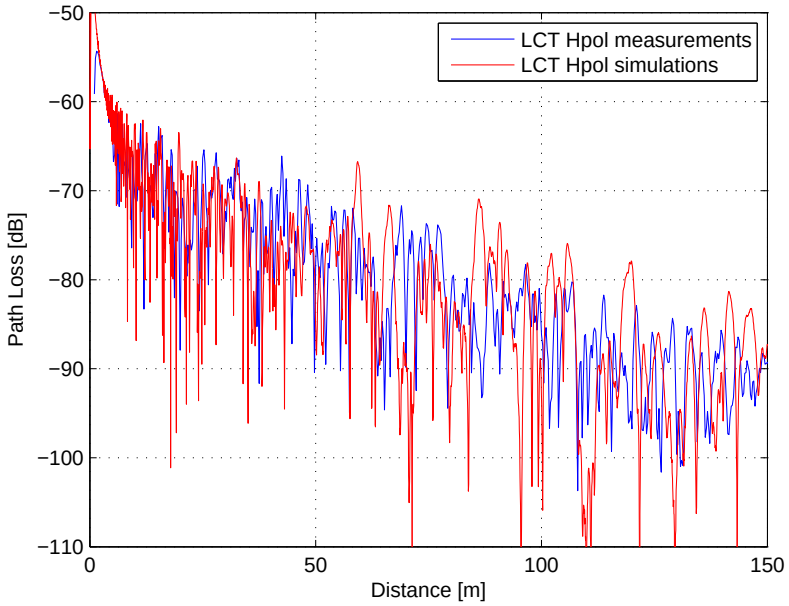

Figure 7.10: L9 comparison. LST curved H polarisation.

Figs. 7.10 and 7.11 show the comparison. It jumps out in both cases that bouncing is much stronger in simulations than in measurements. Despite this fact, path loss trend is predicted successfully by the simulator for both polarisations, and the speed of fast fading oscillations are quite alike also. Because length is shorter for the curved stretch, the above mentioned mismatched peaks and valleys are less probable to appear.

This time the vertical polarisation offers a more accurate prediction than the horizontal polarisation, as values in Table 7.5 show. It is also worth notice the degree of accuracy obtained in the curved scenario respect to those of Table 7.3, which can be directly related to the length of the analysed stretch: because the simulator successfully predicts the initial free space behaviour the precision is enhanced notably. As it has been mentioned throughout the thesis, the spectral technique successfully predicts radiated fields near the source and in this case a higher percentage of the tunnel stretch is predicted with this technique.

Results presented in Tables 7.3,7.4,7.5 indicate that adequate success is attained by the simulator predicting the propagation behaviour of EM waves through L9 tunnels. Though not at the level of accuracy shown by the ray-tracing tool developed by Didascalou [20], the EM simulator here described offers excellent

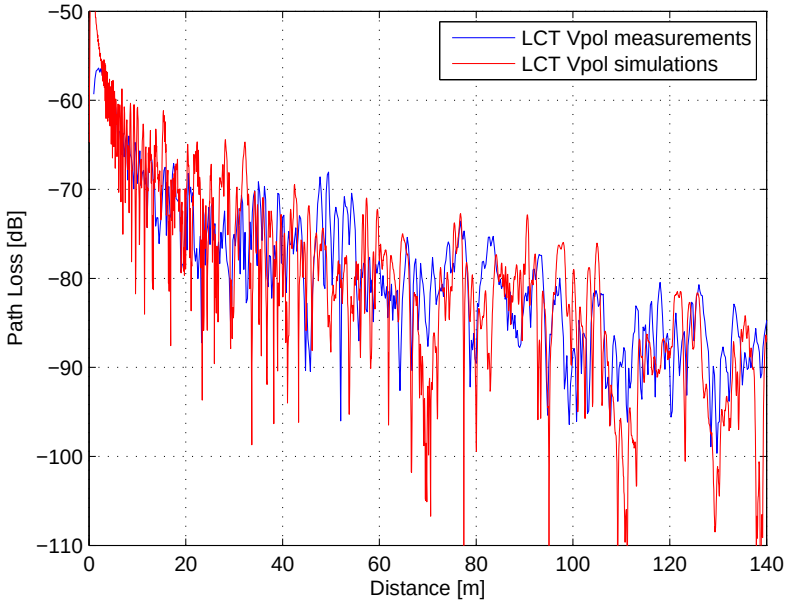

Figure 7.11: L9 comparison. LST curved V polarisation.

Tunnel	LST	
Polarisation	Hpol	Vpol
μ [dB]	4.46	3.81
σ [dB]	5.83	4.82

Table 7.5: Numerical comparison between measurements and simulations for curved L9 tunnels. Window length: 300λ

results in some cases and reasonable ones in others.

Adopting the role of a radio planning engineer, the focus should shift towards the amplitude and frequency of deep fadings. To this end, some statistics are retrieved from the previous figures. This new analysis tries to objectively measure the mean attenuation values and fading characteristics for the different measured and simulated paths.

A first-order linear regression is computed for the transmitting antenna far-field radiation region, where the free-space behaviour disappears and the guided propagation prevails. This will account for the mean path attenuation and the results are summarised in Table 7.6. The regression starts at $z = 60m$ from the transmitter, just where spectral and parabolic techniques are switched. It can be seen how mean attenuation in the straight tunnel is correctly predicted except for the UST, Vpol case - see Fig.7.9- where measurements and simulations less resemble. The values are larger than the theoretical attenuation of the fundamental mode - as computed at the beginning of this Section - because higher order modes have not extinguished due to the low attenuations at such high frequencies.

Notice from Table 7.6 the attenuation increase for the LCT tunnel. Differences between measurements and simulations can be explained by analysed stretch shortness and limitations of the implemented simulator, as

the parabolic technique cannot be used in this case. Again, mean simulated attenuation is close to measured one.

Tunnel	Polarisation	α_{meas} [dB/100m]	α_{sim} [dB/100m]
LST	Hpol	-1.53	-1.40
	Vpol	-1.19	-0.86
UST	Hpol	-2.99	-2.65
	Vpol	-4.55	-2.39
LCT	Hpol	-17.65	-16.73
	Vpol	-13.25	-15.27

Table 7.6: Mean attenuation comparison between measurements and simulations.

The interest now lies on fading characterisation, both amplitude and frequency or repeatability. These two parameters are widespread for indoor and urban radiowave propagation modelling in mobile communications, allowing to guarantee a certain Quality of Service (QoS) for end users.

Addressing the fading amplitude - or strength - issue is done by computing path loss excess as the difference between measured or simulated losses and the previously obtained longitudinal mean attenuation value at each longitudinal point. Figs.7.12,7.13,7.14 show the path loss excess for the different scenarios, while Table 7.7 summarises standard deviation values for each case.

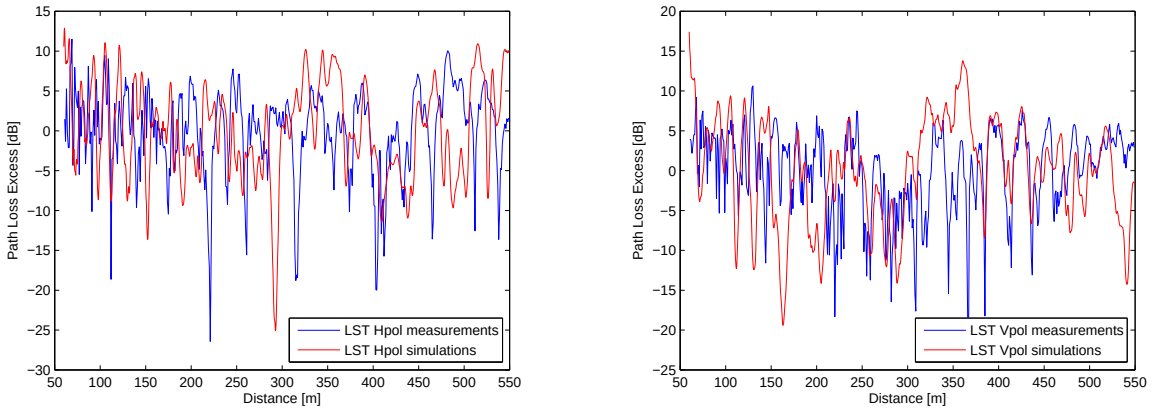

(a) LST, Hpol

(b) LST, Vpol

Figure 7.12: Path loss excess. LST paths.

Simulations offer higher standard deviation values for all cases, specially in LCT scenarios. Taking a look at straight tunnel cases, it can be seen that, in measurements, standard deviation are similar around $5.3dB$, whereas in simulations the values oscillate around $6.2dB$, less than $1dB$ difference. The same cannot be said for LCT, where measurements show a decrease on standard deviation amplitude. This is due to an increase of the attenuation associated to plane waves impinging at tunnel curved walls. On the other hand, LCT simulations numerically predict an increase on standard deviation values but a closer look at LCT Hpol, Vpol cases reveals that the numerical increase is due to a few very narrow, very deep fadings that occur

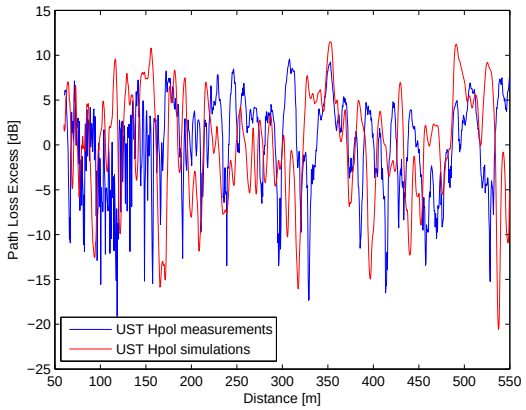

(a) UST, Hpol

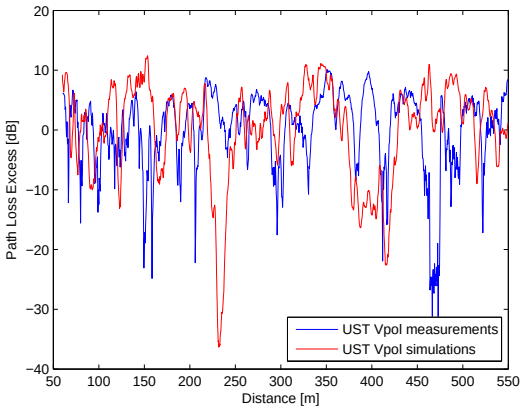

(b) UST, Vpol

Figure 7.13: Path loss escess. UST paths.

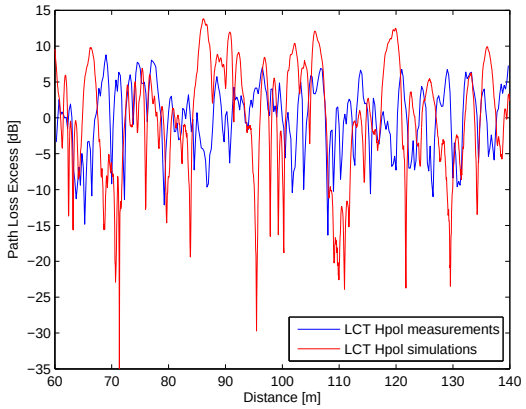

(a) LCT, Hpol

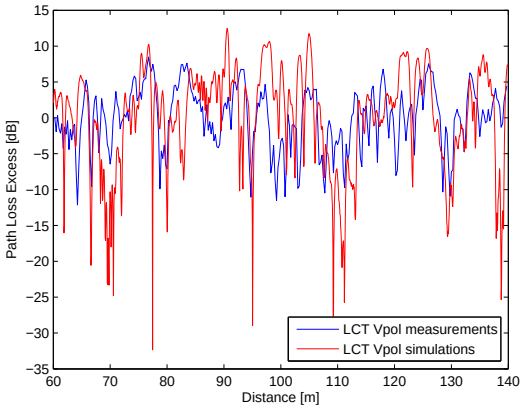

(b) LCT, Vpol

Figure 7.14: Path loss excess. LCT paths.

throughout the curved path. Such narrow deep fadings can be attributed to numerical singularities produced by wavefront phase changes induced during axis rotation -as described in Section 3.2.3 - and, if dismissed, simulation's standard deviation are down to a value approximately $1dB$ higher than measurements, just as in the straight tunnel case.

It is also interesting finding out about fading pseudo-periodicity or frequency of appearance, that will be here called spatial frequency. To do so, the normalised power spectrum of the path loss excess is computed. A quick inspection of the measured and simulated path losses evinces that deep fading spatial pseudo-periodicities are in the range of $10m$ to $100m$, which are associated to spatial frequencies up to $0.1[1/m]$. Figs.7.15,7.16,7.17 show the spatial frequency analysis for the different cases. Starting with the straight tunnel scenarios see how similarities between measurements and simulations are notable except for the UST, Vpol case. Note that for Hpol, both in LST and UST tunnels, spectral components are spread for spatial frequency values up to $0.1[1/m]$, whereas in Vpol cases the components are gathered in the $0 - 0.05[1/m]$

Tunnel	Polarisation	χ_{meas} [dB]	χ_{sim} [dB]
LST	Hpol	5.43	6.06
	Vpol	5.19	6.45
UST	Hpol	5.22	6.05
	Vpol	6.78	8.18
LCT	Hpol	4.83	7.83
	Vpol	4.40	6.81

Table 7.7: Standard deviation comparison between measurements and simulations.

range, meaning that there is higher fading occurrence in vertical polarisation. Meanwhile, it seems that Hpol cases have a richer variety of contributing spectral components.

LCT cases fading analysis shows up deeper, faster and narrower fadings, associated with higher frequency phenomena. Though the length of the tunnel stretch is shorter, more plane wave interactions are expected due to the curved path, leading to the mentioned fading characteristics. If results of Fig.7.17 are observed, higher frequency components - note also that the frequency range has been enlarged - are present in the power spectrum. Figs.7.14 show that there is also the presence of pseudo-periodicities $1m$ to $10m$, associated to these components. The width of the frequency peak components has also increased, which accounts for the narrowness of the spatial fading detected in the LCT cases.

The conclusions of the fading analysis are that simulations predict stronger fadings, which could be overcome by adding some sort of random effect [57] throughout the boundary conditions. This would probably increase the richness of propagation directions and would reduce the fading strength by increasing the number of contributions and decreasing the presence of shadow areas. While it is true that measured and simulated pseudo-periodicities do not match exactly, they are very similar and of the same order, and it also must be taken into account that it is impossible to model all the objects present at the tunnel walls. It is quite possible, though, that including the rough wall modelling developed by Martelly [57] recently would improve the accuracy of simulations herein presented, as it is here recalled that the implemented ADI-parabolic technique is limited to smooth walls.

7.2.3 MIMO results

The use of multiple antennas to exploit the advantages of multipath environments has been well documented. The theoretical properties and limits of Multiple Input, Multiple Output (MIMO) communications systems were first studied by [62] and [63]. This research topic has been subject of study for the last ten years due to the widespread use of personal communications systems. MIMO systems take advantage of he environment by exploiting the diversity that can be applied to a system not only in terms of number of elements, but also in frequency, coding, radiation pattern or polarisation. In here, only the former and the latter are going to be analysed.

A few authors have been interested in the application of MIMO systems in tunnels [64],[65][66],[59],[67] as a method of enhancing the throughput of communications systems operating in such enclosed areas. This

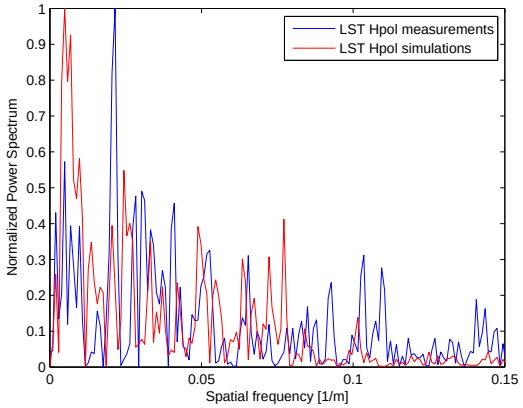

(a) LST, Hpol

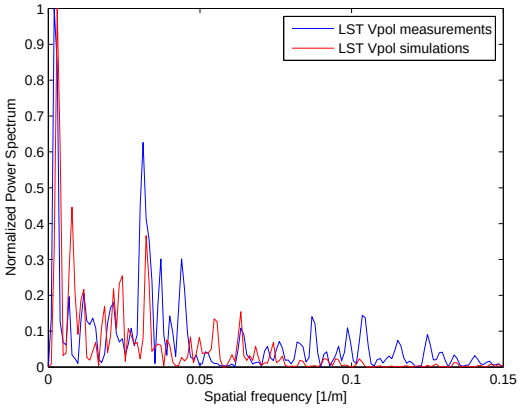

(b) LST, Vpol

Figure 7.15: Fading frequency of appearance for LST paths.

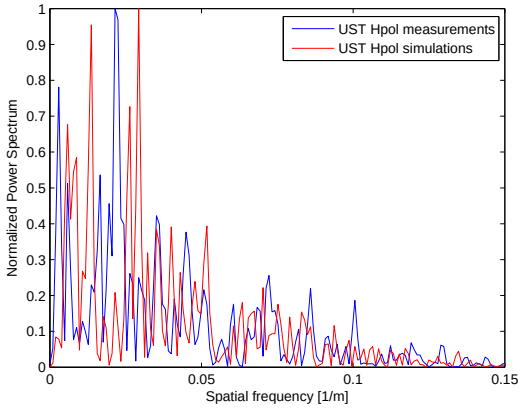

(a) UST, Hpol

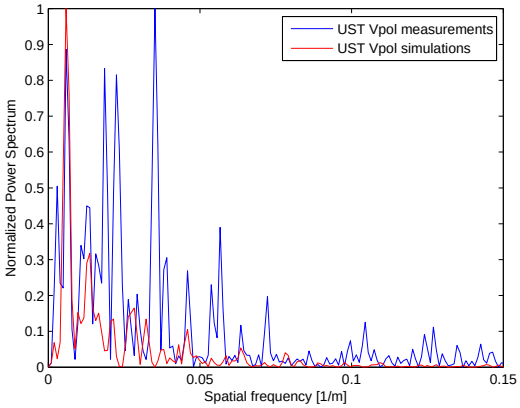

(b) UST, Vpol

Figure 7.16: Fading frequency of appearance for UST paths.

section is not intended to provide a better knowledge of the underlying concepts of MIMO techniques, but rather present the tools required to assess the performance of the implemented EM simulators when dealing with such systems. Theoretical concepts will be briefly introduced and later simulations will be compared against measurements carried out in L9 Barcelona Metro.

The scheme presented in Fig.7.18 shows the different theoretical direct paths that exist in a system with $N_{tx} = 2$ number of transmitters and $N_{rx} = 2$ number of receivers. Path p_{11} corresponds to the signal radiated through transmitting antenna 1 and captured by receiving antenna 1, while path p_{12} corresponds to the signal radiated through transmitting antenna 1 and captured by receiving antenna 2. Paths p_{21} and p_{22} follow the same logic for transmitting antenna 2.

The channel matrix $\underline{\underline{H}}$ is then constructed as follows:

$$\underline{\underline{H}} = \begin{bmatrix} p_{11} & p_{12} \\ p_{21} & p_{22} \end{bmatrix} \tag{7.6}$$

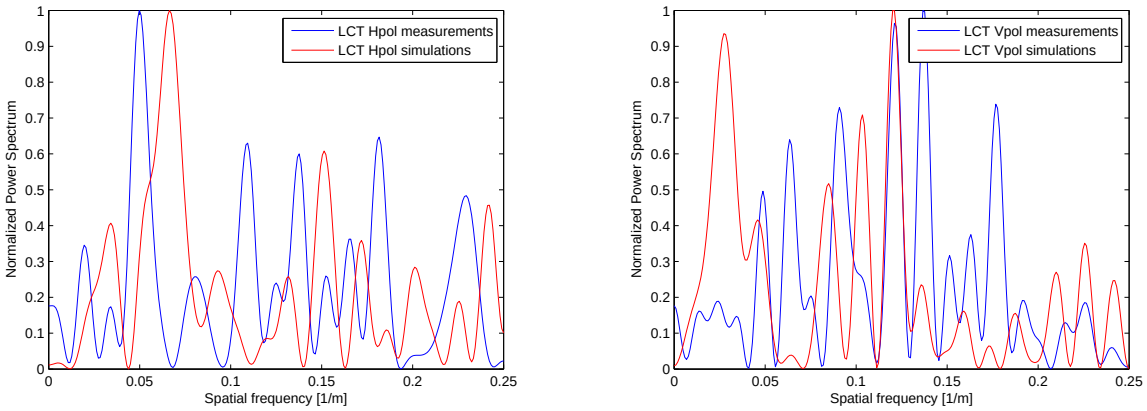

(a) LCT, Hpol

(b) LCT, Vpol

Figure 7.17: Fading frequency of appearance for LCT paths.

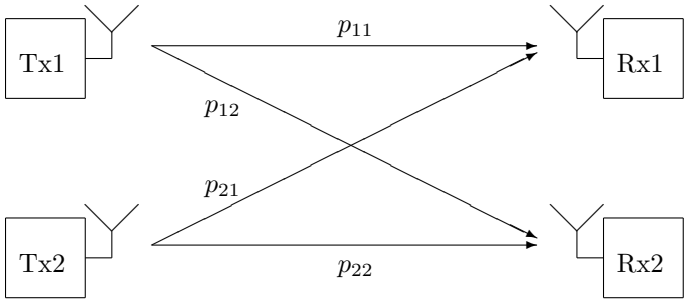

Figure 7.18: Scheme for a 2×2 MIMO communications system.

where the different p_{ij} are the values in phase and magnitude of the corresponding paths. In our case, p_{ij} are obtained from the EM simulator prediction as the wavefront progresses through the tunnel, so $\underline{\underline{H}}$ matrix becomes an array of $2 \times 2 \times N$, N being the total number of points along the longitudinal axis. In order to allow the MIMO channel information arise, attenuation must be taken out of the equation, so the channel matrix is normalised locally at each longitudinal step. Normalisation is computed as [68]:

$$\underline{\underline{H_0}} = \underline{\underline{H}} \frac{\sqrt{N_{rx}}}{\|\underline{\underline{H}}\|_F} \tag{7.7}$$

where the Frobenius norm has been used in the denominator. Once this is done, MIMO processing can be applied to retrieve the characteristics of the multipath environment. The most widespread parameter to measure MIMO systems is the capacity, defined by Shannon [69]. An updated formula for the capacity adapted to MIMO scenarios is [70]:

$$C = log_2 det\left(\underline{\underline{I}} + \frac{SNR_{rx}}{N_{rx}} \underline{\underline{H}}_0 \underline{\underline{H}}_0^H\right) \tag{7.8}$$

This formula, computed for every longitudinal point, offers an idea of how the throughput evolves as the receiver moves away from the transmitter, as we shall see later. The throughput for a Single Input, Single Output (SISO) system - i.e.: a 1×1 transmitting/receiving system - is $C = 3.46\,[bps/Hz]$, while the theoretical limit for a 2×2 MIMO system is $C = 5.17\,[bps/Hz]$, a 50% increase respect to a SISO radio link.

The upper bound is reached when favorable conditions are present, such as multipath richness and totally uncorrelated transmitting antennas.

Another useful way of looking into the capacity is obtaining its Empirical Cumulative Distribution Function (ECDF) along the longitudinal path, which computes the probability of reaching a throughput higher than a certain value that, in this case, is comprised between the SISO and 2×2 MIMO bounds.

The performance of MIMO systems is a function of the environment and the distance and correlation between antenna elements in the transmitting and receiving arrays. In this case, distance between array elements is set to $d_0 = 6\lambda$, and correlation between transmitting antennas is 0. The latter is due to the fact that a first simulation is run with transmitting antenna 1 weighted with a power equal 1 and transmitting antenna 2 weighted with a power equal 0. Paths p_{11} and p_{12} are stored in this first simulation. A second simulation is run with the values reversed, completing the prediction of paths p_{21} and p_{22}. This way, a MIMO EM simulation takes a time that doubles that of a simple EM prediction.

The analysed cases correspond to those measured during L9 campaigns, excluding the curved path. That leaves a total of 6 analysed cases, including upper (UST) and lower (LST) straight tunnels with three different antenna configurations:

1. HH polarisation: transmitting antennas $Tx1$ and $Tx2$ are set with horizontal polarisation. Identical configuration for receiving antennas $Rx1$ and $Rx2$.

2. VV polarisation: transmitting antennas $Tx1$ and $Tx2$ are set with vertical polarisation. Identical configuration for receiving antennas $Rx1$ and $Rx2$.

3. VH polarisation: $Tx1$ is set with horizontal polarisation, $Tx2$ is set with vertical polarisation. Identical configuration for receiving antennas $Rx1$ and $Rx2$.

The analysed cases were simulated as in the L9 propagation analysis, with the respective upper and lower equivalent rectangular tunnels. Results in terms of capacity and ECDF are presented in Figs.7.19,7.20,7.21 for the UST tunnel and Figs.7.22,7.23,7.24 for the LST tunnel. Recall that a moving average filter is used to filter fast fading oscillations in order to be able to retrieve meaningful information, the window length being 300λ as in the propagation study of the previous Subsection.

First comparing the behaviour exhibited by the upper and lower tunnel cavities, it jumps out that the former seems to lead to higher and narrower capacity peaks than the latter, whose behaviour is slightly different, with capacity being more steadily, lower and broader peaks. This behaviour is also obtained in simulations for the different presented cases.

It can be noted that the minimum capacity bounds are lower for the UST tunnel than for the LST tunnels: while minimums are comprised between $3.5 - 3.6bps$ for the former, these values are mildly increased to the $3.6 - 3.8bps$ range for the latter, and this is successfully modelled by the simulator too.

Comparing measurements and simulations, more similarities between MIMO results can be found for the LST tunnel than for the UST as expected. The tunnel cross-section similarity in the first case is the reason to such results. Though the adoption of the Chen approach [28] for the arched tunnel allows to analyse the curved profile while obtaining good results, the difference between the interaction if impinging plane waves

at parallel and orthogonal boundaries or at curved boundaries is a limit that cannot be overcome, at least to a certain degree.

On the other hand it can be observed that predicted capacity is higher than the one extracted from measurements. This is a direct consequence of the higher standard deviation values for path loss excess shown throughout this chapter. Higher values lead to increased capacity.

Finally, notice that the VHpol case provides better throughput in the LST tunnel. This is due to the fact that the arched ceiling of the UST tunnel leads to larger cross-polarisation effects. Hence signals from Tx1 and Tx2 become less uncorrelated and capacity drops. Meanwhile, parallel or orthogonal surfaces avoid such a rich cross-polarisation behaviour, signals remaining higly uncorrelated. The simulator has more success with the lower cavity, and predicts the increase in capacity respect to the copolarised HHpol and VVpol cases.

Alonso [71] showed that differences in MIMO performance is highly dependant on local scattering. Hence, without a highly accurate scenario modelling it is very hard to reproduce measurement results consistently. It is to be expected that the development of the ADI simulator for curved boundaries will lessen the differences between measurements and simulations. As results in Table 4.9, the spectral technique does not better EM predictions for curved boundaries than it does for rectangular boundaries, and just looking at the accuracy improvement provided by ADI in Table 6.2 suggests that predictions will be much better.

Having analyzed the simulator's performance and the EM behaviour at L9 tunnels, the impact of the 2x2 MIMO scheme on the capacity is not amazing overall. In the majority of cases the threshold of $4bps$ is not reached for the 50% of the analyzed stretch, exception being the LST-VHpol case. True is that transmitting antennas were placed close to the tunnel centre, while in the study developed by Alonso [71] it was concluded that an optimal position for transmitting antennas would be centred and close to the tunnel ceiling.

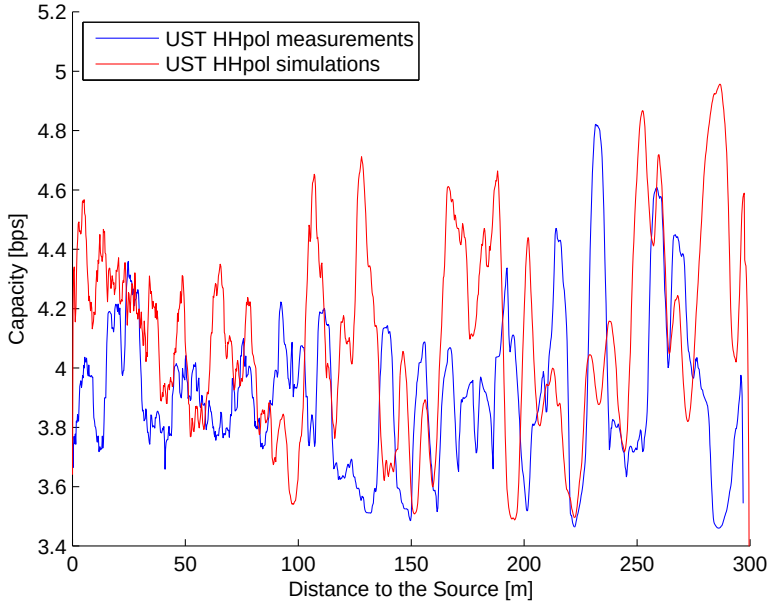

(a) Capacity

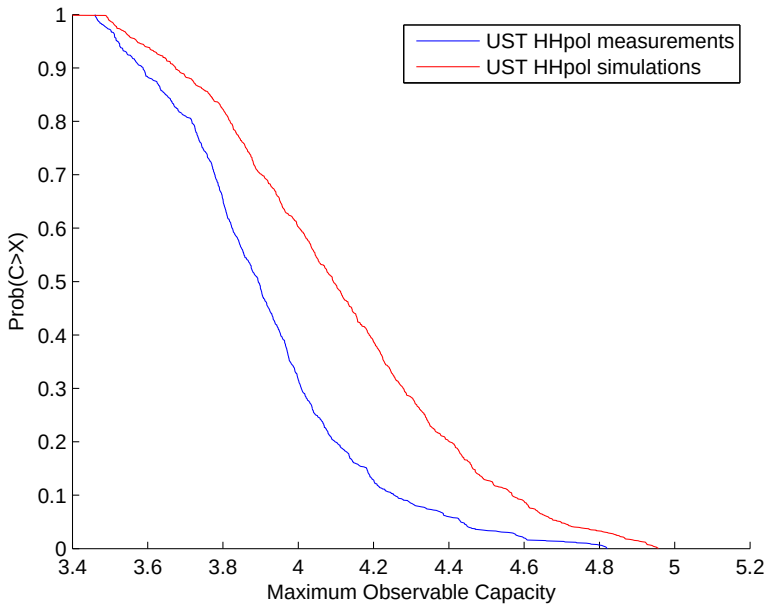

(b) ECDF

Figure 7.19: MIMO measurements and simulations comparison. UST, HH polarisation.

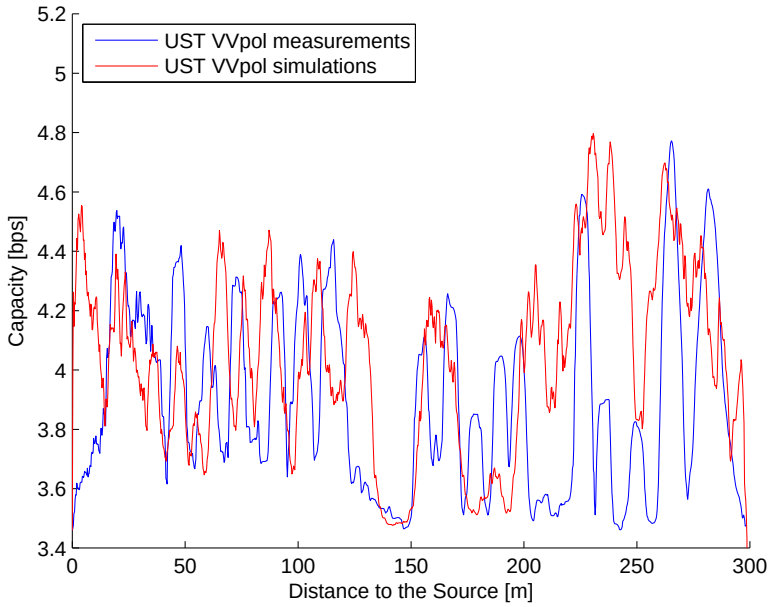

(a) Capacity

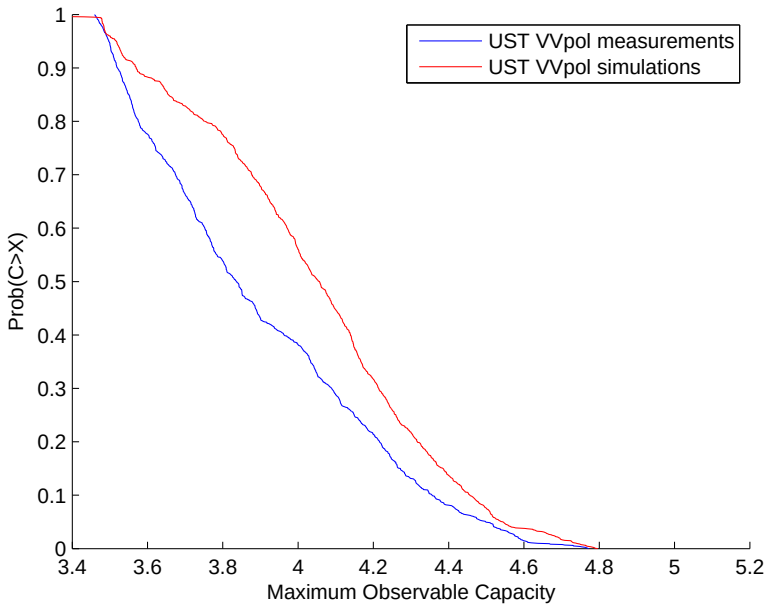

(b) ECDF

Figure 7.20: MIMO measurements and simulations comparison. UST, VV polarisation.

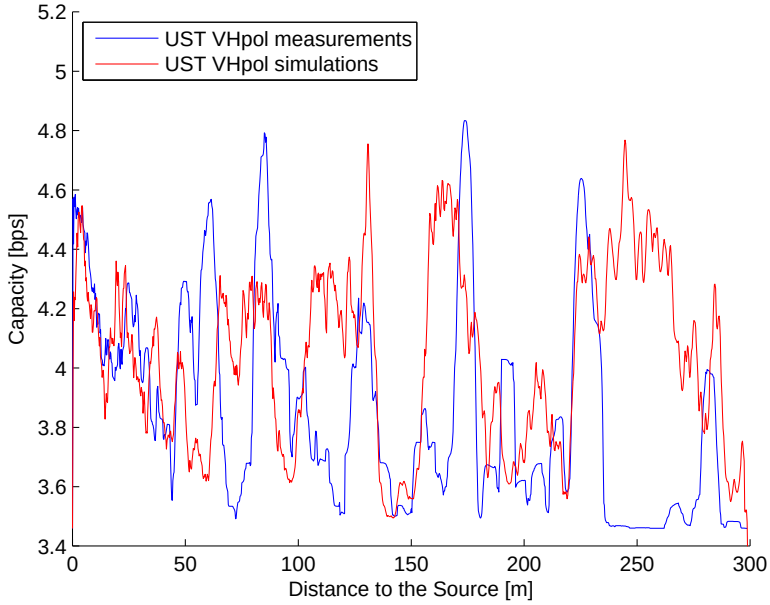

(a) Capacity

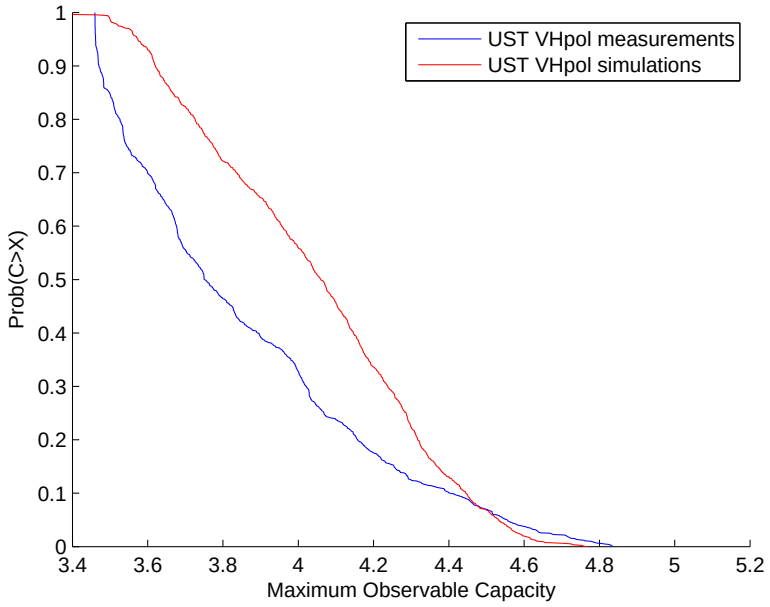

(b) ECDF

Figure 7.21: MIMO measurements and simulations comparison. UST, VH polarisation.

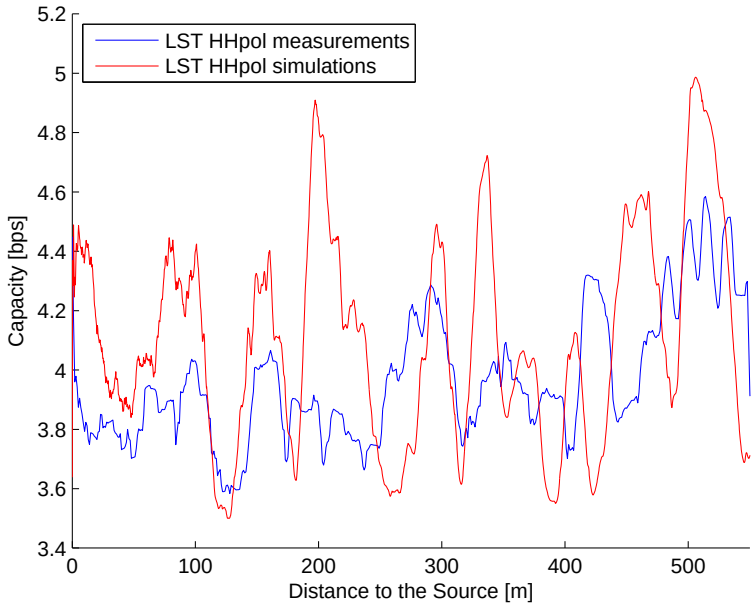

(a) Capacity

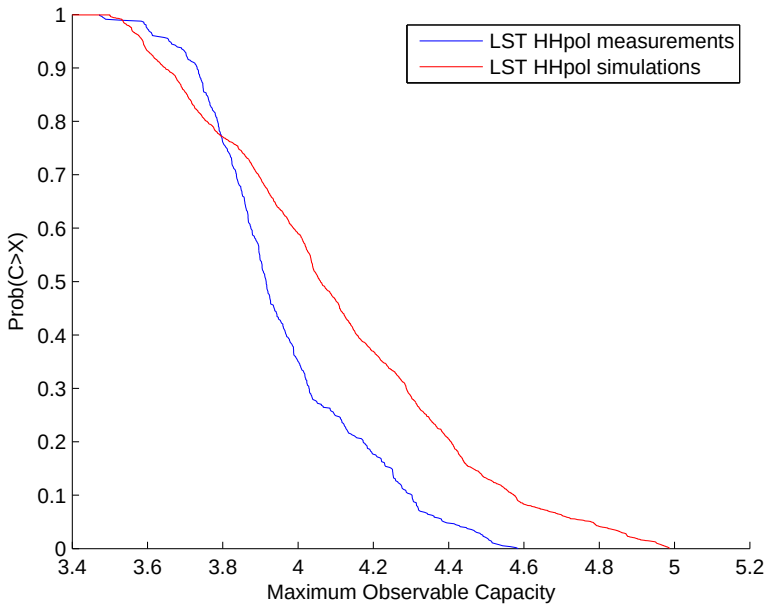

(b) ECDF

Figure 7.22: MIMO measurements and simulations comparison. LST, HH polarisation.

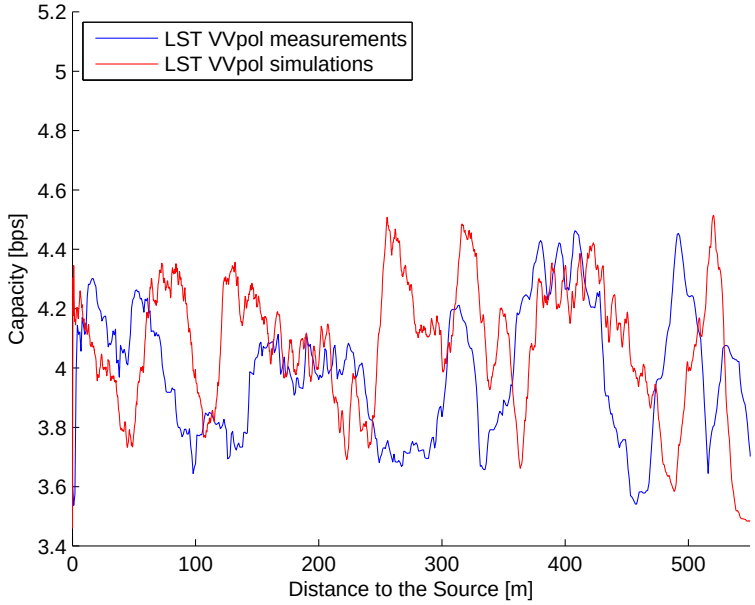

(a) Capacity

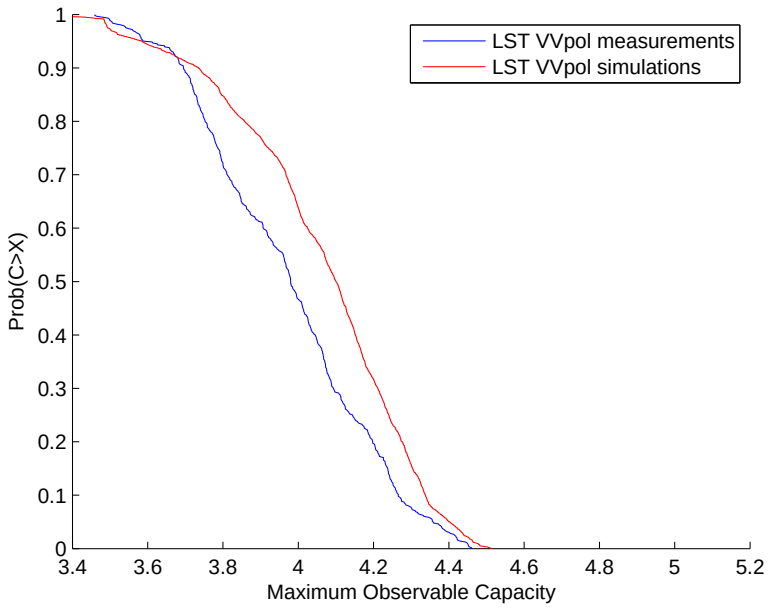

(b) ECDF

Figure 7.23: MIMO measurements and simulations comparison. LST, VV polarisation.

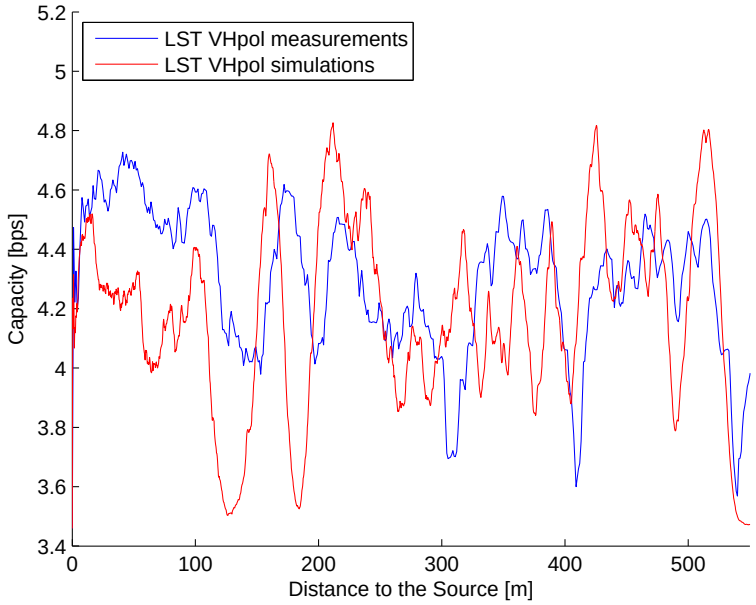

(a) Capacity

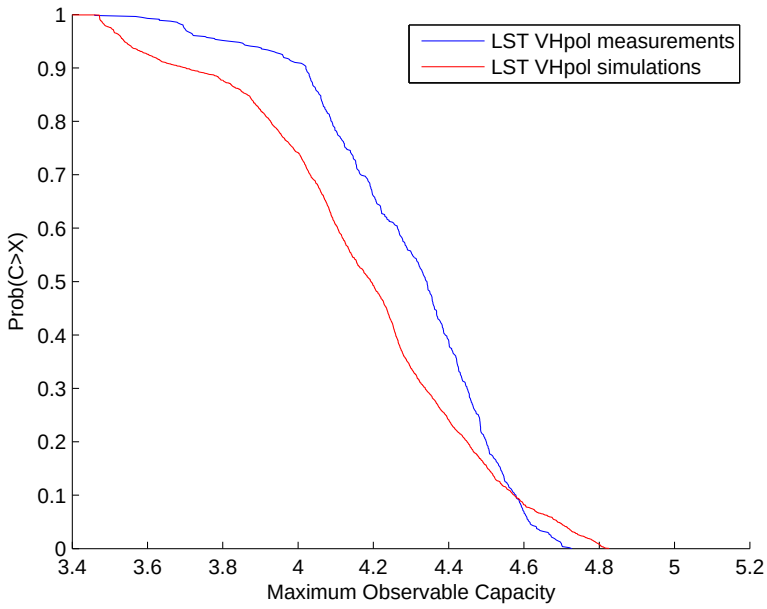

(b) ECDF

Figure 7.24: MIMO measurements and simulations comparison. LST, VH polarisation.

Chapter 8

Conclusions

Since I started this thesis, four years ago, I have seen how common people technology needs have grown at a rate that was hard to figure out then. Even myself, who only used to check the email once or twice per day and use the cellphone only for classic - voice call and text message for instance - communication purposes, routinely use the mentioned communications services as well as look for the hottest video and audio hits, or the latest posts in widespread social networking services and blogs during our spare time. Given that wireless technologies have given us all these possibilities, the society has embraced them and expects them to be available anytime, anywhere. Personal opinions are now tweeted while waiting for the next train.

On the other hand, during the same time span, we have assisted to several accidents involving railway transport services. Railways have historically been a hostile environment that has offered significant resistance to the introduction of the latest technology trends. And it is understandable, as a service whose first and foremost principle has always been security and regularity. As a consequence, only heavily-tested technologies have been employed in railway communications, which has resulted in an increasing communications gap for transport service users. It was not long ago that we could not be reached if someone called while going from one place to another through the metro. Today, this is considered unacceptable. And even if mobile communications services have slowly been introduced at these environments, the quality of such services at certain spots is clearly insufficient.

As the entity responsible for key transport infrastructures in Catalunya, Ifercat, aware of the fact that the majority of railway accidents are attributed to human mistakes, faced up the challenge of introducing wireless technologies at the backbone of L9 control systems. The design of this metro line is based on the Automatic Train Control system employing wireless technologies. At the same time, even if no personnel is on board, surveillance and user security relies on a wideband video transmitting system. This thesis was engineered by Ifercat in collaboration with the Signal Theory and Communications department of UPC to assess the viability of such services, which this thesis has been devoted to.

Even if time frames of L9 services and this research project have not always matched, contributions of the thesis can have a significant impact on the assessment of today and tomorrow communications services deployment in railway scenarios, and that has been one of the guiding forces through the last four years.

The physical layer of the problem has occupied the core of the time spent during the research. L9 poses a complex structure to be analysed, and for this reason the spectral technique was first chosen: it allows an integral treatment of the studied scenario. A simulator based on this method has been implemented and tested, although there are some aspects that can be improved.

The most delicate point of this part of the thesis has been the application of boundary conditions, that have a significant impact on the simulator predictions. As it has been shown throughout the thesis, use of the well-known reflection coefficients for parallel and perpendicular polarisations has not yielded accurate enough results. At the beginning, a scalar version of the spectral simulator was developed and compared to published results with success. That version applied the boundary conditions roughly, as only the change of media was taken into account, neglecting the impact of the incidence angle and field orientation. Once the polarimetric simulator was under way, the problem of discriminating between horizontal and parallel polarisation arose. It is not just a matter of propagating each polarisation with the corresponding attenuation, but also of taking into account the cross-polarisation effects that occur at the tunnel boundaries as a consequence of the incidence of several plane waves at curved surfaces. It was clear then that the scalar approach no longer worked, so it was natural to add the reflection coefficients to complete the physical modelling of the problem. Mixed results are obtained: when compared to modal theory published results, it is clear that the accuracy provided by this implementation is lower than the accuracy provided by other techniques, such as those employing ray-tracing. On the other hand, when compared to published measurements, it can be argued that the spectral simulator allows to understand what is happening inside the tunnel with reasonable precision.

The reason that lies after the inaccurate predictions of the spectral technique is the fact that polarimetric boundary conditions are applied in ray-tracing-like approach. While equivalent, rays, as defined in geometrical optics, and plane waves differ in one aspect that is critical when facing the application of boundary conditions: rays have a clearly defined path, composed by an origin point and an end point, that allows to easily obtain the incidence angle at a certain point of the boundary surface. It is then straightforward computing the reflected ray as a function of the physical properties of the boundary, including some random roughness that may modify the reflected ray angle of propagation. However, spectral techniques deal with plane waves, that are composed by a set of points in space propagating with the same phase. Hence, it is not possible to assign a unique impinging point of the surface where the plane wave reaches the boundary. It jumps out then that, the way the spectral simulator is implemented, as described in Chapter 3, we are introducing an error in the application of the boundary conditions, as only a fraction of the plane wave is being modified accordingly. Conversely: each point in the spatial domain is composed by a weighted sum of plane waves propagating in every directions of space, so changing the value of the field points at the boundary also modifies inadequately the characteristics of many plane waves points that may not be impinging tangentially or orthogonally at the boundary.

Since the Nyquist requirements were fulfilled, usually working with discrete meshes of $\lambda/4$ or finer, the other source of error is tunnel modelling. It is relatively easy to obtain and introduce a geometrical description of a tunnel cross-section as well as its transversal dimensions. The path followed by measurements, though,

is harder to model. But what probably are the major points are the electrical properties of the tunnel walls and their roughness, because of the difficulties their measurement presents. Wall electrical properties are modified by humidity at the moment the measurements are taken. After several campaigns at L2 and L9 tunnels of Barcelona Metro, one realises that even when no river is close, water filters through the tunnel structural joints in significant amounts. This was demonstrated during simulations, were different complex permittivities were applied in order to tune the predictions to the measurement results.

Once it was clear that boundary conditions were a limiting factor, the following step was trying to solve the problem. Leontovich boundary conditions seemed to be suited for their application in the spectral problem, but early results were not encouraging. They did not improve the accuracy, nor did they provide better physical explanations to the problems that curved surfaces presented when working with the spectral technique. Nevertheless, they opened the door to work with the parabolic equation and, more precisely, the Alternating Direction Implicit (ADI) method. As described in Chapters 5 and 6, a simulator based on this approach has also been implemented successfully, as it has been proven when compared against canonical and measured published results.

The combination of both techniques, spectral and parabolic, comes naturally due to the own characteristics of each method and, as it has been shown, they complement each other well. Precision, in terms of attenuation, is improved respect to the mono-spectral prediction results, as is the simulation time. The use of the parabolic-based simulator has helped to overcome the annoyance of having to wait for several hours for the results of spectral predictions. The time reduction reaches frames of three to four hours for a complete $600m$ tunnel analysis at $5.8GHz$. Once that the fundamental limits of parabolic convergence are fulfilled, sources of error are limited to initial field and tunnel modelling.

ADI initial field carries the errors introduced by the incorrect application of boundary conditions in the stretch analysed with the spectral technique. For that reason, the length of this stretch is minimised. The trade-off is the loss of flexibility, as PE-ADI can model only straight, rectangular, smooth tunnels. As is been shown in Chapter 7, the amount of *noise* introduced on the path loss curve if an early switch between techniques is performed could mask the tunnel behaviour, but the outcome resembled anyway, so the trade-off is solved by ensuring that most of the energy propagating through the tunnel is contained inside the parabolic margin. The implementation chosen for ADI method ensures less than a 1% error for propagation contained inside that margin, which exceedingly satisfies the needs of radio network planning. But a reason of the success attained by the ADI method predictions, even if the initial field presents some errors, is the fact that tunnels behave as oversized lossy waveguides. Repeated application of boundary conditions forces the inner fields to converge to the correct solution, although more distance may be necessary to reach it as shown in Chapter 6.

Path loss curves measured at L9 have been predicted successfully with the simulator, although the reached accuracy is lower than that obtained by ray-tracing programs such as [20] and, in some cases, by other ADI implementations [54]. This can be attributed to tunnel modelling, as several issues have been highlighted by the comparison with L9 measurements. Sun approach [37], used throughout this work, is limited to the attenuation value of the dominating modes, as MIMO curve predictions for the upper straight tunnel do

not resemble much with measurements. The fact that nor arched cross-sections, nor curved paths have been possible to simulate with the current version of the algorithm have limited the success of the predictions provided. Nevertheless, results for the quasi-rectangular lower straight tunnel show that there is plenty of good results and promise on the use of the mixed spectral-parabolic approach. The combined simulator has been tested at several bands and compared against published data with good results, and experimentally has verified with some accuracy limitations the experimental campaign developed at L9 tunnels.

For the EM simulator to improve, it is essential to solve the polarimetric boundary condition application issue. Although several solutions have been tried, none of them yielded better results than the one that was chosen for the final implementation of the simulator. Different approximations to the incidence angle were used while dealing with the geometrical optics approach but, although the system showed sensibility to the value of the incidence angle, results were not good enough. Also, polarimetric masks - whose value changed depending on the polarisation and angle respect to the axis - did not sustain good results consistently. Perhaps a fast and efficient computation of local incidence angle, taking advantage of the Fourier transforms performed to advance through the tunnel in combination with wavelets, could work reasonably well in optical terms. But given that the geometrical optics approach seems to not work well with wavefronts, maybe some kind of modified Leontovich boundary conditions could work, as they seemed not to perform very well close to the source where the incidence is not grazing. Nevermind, it is, in my opinion, the most urgent issue to solve, and the one that may boost a vast improvement on the prediction accuracy provided by this simulator.

Another pending issue is the possibility of including arbitrary tunnel cross-sections, curved paths and wall roughness [50],[57] into the parabolic simulator. As currently designed, the fact that only straight rectangular tunnels can be analysed with the parabolic technique is a weakness that can be overcome in a reasonable period and improve the accuracy of this method that, as the MIMO analysis has shown, still has its flaws. Solving this issue would provide us with two tools flexible enough to face complex scenarios that could be compared against each other to gauge the predictions. That does not exclude the possibility of combining them, depending on the presence of obstacles inside the tunnel to put an example.

As already mentioned before, the excessively large execution time issue when long tunnels were simulated with the spectral technique at large frequencies was solved by the use of the mixed approach. But there is still more progress to be done in this area. For instance, some tests were made with the spectral propagation loop written with a C function using a FFT implementation that differs to the one employed in Matlab. The speed was notably higher and time frames were reduced down to 50%. On the other hand, the chosen ADI implementation is based on simple programming using loops, not taking advantage of Matlab strengths. The reason is that it allowed for a better comprehension and eased the translation from the physical phenomena described by equations to pure linear code. But the literature has offered some matrix implementations [53],[55] that seem to better match with Matlab strengths.

Finally, a few words on the use of MIMO communications systems in tunnel environments. As it has been shown, this kind of systems enhance the throughput between a static base station and a mobile receiver. The frequency at which this study has been performed, $5.8GHz$, is large enough to allow the use of several array elements, as the wavelength is on the order of $5cm$. Though there is not a lot of available space in the

tunnel, nor in the train, horizontal linear arrays with 4 or more elements seem to be feasible. After all, we are talking of a $1m$ wide antenna for a 4-element, 6λ-spaced array, and the train has $3m$ wide approximately. the use of high directivity antennas should offer some advantages as well. Overall, the increase in terms of capacity has not been very impressive but, as Alonso [71] concludes in its L9 study, a different transmitting array location would provide significant improvements, and it could lead to an excellent performance of the video surveillance system and to the introduction of the latest mobile communications services inside tunnels as well.

Longer measurement campaigns should be carried out to confirm the statements above. As Dudley [16] and Molina-García-Pardo [66] have shown in their studies, the source placement plays a pivotal role on the propagation outcome. So far, campaigns at L9 tunnels have taken place with the transmitter and receiver placed close to the tunnel centre. It would be really interesting the results of measurements with transmitting antennas placed in a more practical location, close to the tunnel walls and ceiling and receiving antennas mounted on top of a train carriage, or at least at the same height. Due to the small time frame available, several repetitions of the same path could hardly be performed. Taking into account the frequency and the distance range at which measurements were made, it would help enormously to a more complete EM characterisation of the environment. Wideband analysis was deemed unnecessary, at least up to date, as the angle of arrival was difficult to measure and is logically expected to be narrowed to the longitudinal tunnel axis at large distances from the source, due to attenuation suffered by other components at the tunnel walls. In the same line of thought, delay spread must not be very large.

The foregoing notwithstanding, L9 Metro service is, at the time this lines are being written, successfully working at some stretches. For most of the time, the difficulties found during the development of the thesis prevented their direct application on the radio planning for the already open stretches, although these stretches were used to tune the simulator behaviour thanks to the measurement campaigns that were carried out. There is, however, a part of the path that has not been finished yet, so there is still the opportunity of using this thesis as a helping tool on the wireless radio planning for the remainder of the tunnel stretches.

Bibliography

[1] R. F. Harrington, *Time-Harmonic Electromagnetic Fields*. John Wiley & Sons, 1961.

[2] C. A. Balanis, *Advanced Engineering Electromagnetics*. John Wiley & Sons, 1989.

[3] N. N. Bojarski, "K-Space Formulation of the Electromagnetic Scattering Problem," Air Force Avionics Laboratory, Wright-Paterson AFB, Tech. Rep. AFAL-TR-71-75, 1971.

[4] ——, "K-Space Formulation of the Electromagnetic Scattering Problem," Air Force Avionics Laboratory, Wright-Paterson AFB, Tech. Rep. AFAL-TR-72-271, 1972.

[5] J. Romeu, "Formulación Espectral de la Radiación. Aplicación al Caso Cilíndrico," Ph.D. dissertation, Departament de Teoria del Senyal i Comunicacions, UPC, 1991.

[6] R. Kastner and R. Mittra, "A Spectral-Iteration Technique for Analyzing Scattering from Arbitrary Bodies, Part I: Cylindrical Scatterers with E-wave Incidence," *Antennas and Propagation, IEEE Transactions on*, vol. 31, no. 3, pp. 499–506, May 1983.

[7] A. Anderson and G. Cook, "Incremental Propagation Procedure for Calculating Scattered Fields from Arbitrary Conductors," in *European Microwave Conference, 1985. 15th*, 1985, pp. 213–218.

[8] G. Cook, A. Anderson, and A. Turnbull, "Spectral Incremental Propagation (SIP) Procedure for Fast Calculation of Scattered Fields from Conducting Bodies," in *Microwaves, Antennas and Propagation, IEE Proceedings*, vol. 136, no. 1, Feb 1989, pp. 34–38.

[9] A. Broquetas, J. Romeu, C. Espinós, L. Jofre, and M. Ferrando, "Análisis de la difracción de cuerpos metálicos mediante el método incremental," in *IV Simposium Nacional del Comité Español de la URSI*, Septiembre 1989, pp. 625–628.

[10] A. Lozano, "Algoritmo Iterativo de Propagación Espectral para el Cálculo de RCS en Cavidades Conductoras," Master Thesis, ETSETB, UPC, 1992.

[11] J. Rius, A. Lozano, L. Jofre, and A. Cardama, "Spectral Propagation Algorithm for RCS of Perfectly Conducting Cavities," Jul 1992, pp. 945–948 vol.2.

[12] ——, "Spectral Iterative Algorithm for RCS Computation in Electrically Large or Intermediate Perfectly Conducting Cavities," *Antennas and Propagation, IEEE Transactions on*, vol. 42, no. 6, pp. 790–797, 1994.

[13] A. Cardama, L. Jofre, J. Rius, J. Romeu, and S. Blanch, *Antenas*, UPC, Ed. UPC, 1998.

[14] D. Dudley and S. Mahmoud, "Linear Source in a Circular Tunnel," *Antennas and Propagation, IEEE Transactions on*, vol. 54, no. 7, pp. 2034 – 2047, july 2006.

[15] S. F. Mahmoud, "Modal Propagation Of High Frequency Electromagnetic Waves In Straight And Curved Tunnels Within The Earth," *Journal of Electromagnetic Waves and Applications*, vol. 19, no. 12, pp. 1611–1627, 2005.

[16] D. Dudley, M. Lienard, S. Mahmoud, and P. Degauque, "Wireless Propagation in Tunnels," *Antennas and Propagation Magazine, IEEE*, vol. 49, no. 2, pp. 11–26, 2007.

[17] M. Choi, D. Kim, H. Jo, J. Yook, and H. Park, "Path-Loss Characteristics in Subway Tunnels at 2.65GHz," *Microwave and Optical Technology Letters*, vol. 48, no. 2, February 2006.

[18] T.-S. Wang and C.-F. Yang, "Simulations and Measurements of Wave Propagations in Curved Road Tunnels for Signals From GSM Base Stations," *Antennas and Propagation, IEEE Transactions on*, vol. 54, no. 9, pp. 2577–2584, 2006.

[19] J. Wait, "Electromagnetic Whispering Gallery Modes in a Dielectric Rod," *Radio Science*, vol. 2, no. 9, pp. 1005–1007, September 1967.

[20] D. Didascalou, J. Maurer, and W. Wiesbeck, "Subway Tunnel Guided Electromagnetic Wave Propagation at Mobile Communications Frequencies," *Antennas and Propagation, IEEE Transactions on*, vol. 49, no. 11, pp. 1590–1596, 2001.

[21] J. Glaser, "Attenuation and Guidance of Modes on Hollow Dielectric Waveguides (Correspondence)," *Microwave Theory and Techniques, IEEE Transactions on*, vol. 17, no. 3, pp. 173 – 174, mar 1969.

[22] A. Emslie, R. Lagace, and P. Strong, "Theory of the propagation of UHF radio waves in coal mine tunnels," *Antennas and Propagation, IEEE Transactions on*, vol. 23, no. 2, pp. 192–205, Mar 1975.

[23] Y. Zhang, "Novel Model for Propagation Loss Prediction in Tunnels," *Vehicular Technology, IEEE Transactions on*, vol. 52, no. 5, pp. 1308–1314, 2003.

[24] J. Molina-Garcia-Pardo, M. Lienard, A. Nasr, and P. Degauque, "On the Possibility of Interpreting Field Variations and Polarization in Arched Tunnels Using a Model for Propagation in Rectangular or Circular Tunnels," *Antennas and Propagation, IEEE Transactions on*, vol. 56, no. 4, pp. 1206–1211, April 2008.

[25] G. Roqueta, B. Monsalve, S. Blanch, J. Romeu, and L. Jofre, "Microwave Dielectric Properties Inspection of Fiber-Reinforced Civil Structures," in *Antennas and Propagation Society International Symposium, 2008. AP-S 2008. IEEE*, 5-11 July 2008, pp. 1–4.

[26] S. Loredo, L. Valle, and R. Torres, "Accuracy Analysis of GO/UTD Radio-Channel Modeling in Indoor Scenarios at 1.8 and 2.5 GHz," *Antennas and Propagation Magazine, IEEE*, vol. 43, no. 5, pp. 37–51, Oct 2001.

[27] S. Loredo, A. Rodriguez-Alonso, and R. P. Torres, "Indoor MIMO Channel Modeling by Rigorous GO/UTD-Based Ray Tracing," *Vehicular Technology, IEEE Transactions on*, vol. 57, no. 2, pp. 680–692, March 2008.

[28] S.-H. Chen, S.-H. Chen, and S.-K. Jeng, "SBR image approach for radio wave propagation in tunnels with and without traffic," *Vehicular Technology, IEEE Transactions on*, vol. 45, no. 3, pp. 570–578, 1996.

[29] Y. Zhang, Y. Hwang, and R. Kouyoumjian, "Ray-Optical Prediction of Radio-Wave Propagation Characteristics in Tunnel EnvironmentsPart 2: Analysis and Measurements," *Antennas and Propagation, IEEE Transactions on*, vol. 46, no. 9, pp. 1337–1345, September 1998.

[30] S. Mahmoud and J. Wait, "Geometrical Optical Approach for Electromagnetic Wave Propagation in Rectangular Mine Tunnels," *Radio Science*, vol. 9, no. 12, pp. 1147–1158, December 1974.

[31] A. E. Karbowiak, "Theory of Imperfect Waveguides: The Effect of Wall Impedance," in *Proc. Inst. Elec. Eng.*, vol. 102, part B, 1955, pp. 698–709.

[32] S. Mahmoud and J. Wait, "Theory of Wave Propagation along a Thin Wire inside a Rectangular Waveguide," *Radio Science*, vol. 9, no. 3, pp. 417–420, 1974.

[33] J. Wait and D. Hill, "Guided Electromagnetic Waves along an Axial Conductor in a Circular Tunnel," *Antennas and Propagation, IEEE Transactions on*, vol. 22, no. 4, pp. 627 – 630, jul 1974.

[34] K. D. Laakmann and W. H. Steier, ""waveguides: Characteristic modes of hollow rectangular dielectric waveguides"," *Applied Optics*, vol. 15, Issue 5, pp. 1334–1340, 1976.

[35] D. Dudley, "Wireless Propagation in Circular Tunnels," *Antennas and Propagation, IEEE Transactions on*, vol. 53, no. 1, pp. 435–441, 2005.

[36] D. Didascalou, D. Didascalou, J. Maurer, and W. Wiesbeck, "Natural wave propagation in subway tunnels at mobile communications frequencies," in *Vehicular Technology Conference Proceedings, 2000. VTC 2000-Spring Tokyo. 2000 IEEE 51st*, J. Maurer, Ed., vol. 3, 2000, pp. 2009–2013 vol.3.

[37] J. Sun and L. Cheng, "Equivalent Analysis Method of Electromagnetic Waves Propagation in Arched Tunnel," *Applied Mathematics and Computation*, vol. 178, no. 2, pp. 332–337, 2006.

[38] C. Holloway, D. Hill, R. Dalke, and G. Hufford, "Radio Wave Ppropagation Characteristics in Lossy Circular Waveguides such as Tunnels, Mine Shafts, and Boreholes," *Antennas and Propagation, IEEE Transactions on*, vol. 48, no. 9, pp. 1354 –1366, sep 2000.

[39] D. Dudley and H.-Y. Pao, "System Identification for Wireless Propagation Channels in Tunnels," *Antennas and Propagation, IEEE Transactions on*, vol. 53, no. 8, pp. 2400 – 2405, aug. 2005.

[40] D. Didascalou, M. Dottling, T. Zwick, and W. Wiesbeck, "A Novel Ray-Optical Approach to Model Wave Propagation in Curved Tunnels," in *Vehicular Technology Conference, 1999. VTC 1999 - Fall. IEEE VTS 50th*, vol. 4, 1999, pp. 2313 –2317 vol.4.

[41] S. Mahmoud and J. Wait, "Guided Electromagnetic Waves in a Curved Rectangular Mine Tunnel," *Radio Science*, vol. 9, pp. 567–572, December 1974.

[42] Y. Zhang and Y. Hwang, "Characterization of uhf radio propagation channels in tunnel environments for microcellular and personal communications," *Vehicular Technology, IEEE Transactions on*, vol. 47, no. 1, pp. 283 –296, feb 1998.

[43] J. Lamminmaki and J. Lempiainen, "Radio Propagation Characteristics in Curved Tunnels," *Microwaves, Antennas and Propagation, IEE Proceedings* -, vol. 145, no. 4, pp. 327 –331, aug 1998.

[44] M. Lienard, P. Degauque, and P. Laly, "Long-Range Radar Sensor for Application in Railway Tunnels," *Vehicular Technology, IEEE Transactions on*, vol. 53, no. 3, pp. 705–715, 2004.

[45] ——, "Communication and Distance Measurement in Subway Tunnels using Natural Propagation," in *Devices, Circuits and Systems, 2004. Proceedings of the Fifth IEEE International Caracas Conference on*, vol. 1, 3-5 Nov. 2004, pp. 240–243.

[46] A. Oppenheim and R. Schafer, *Discrete-Time Signal Processing.* Prentice Hall, 1989.

[47] J. C. Strikwerda, *Finite Difference Schemes and Partial Differential Equations*, 2nd ed. SIAM, 2004.

[48] K. W. Morton and D. F. Mayers, *Numerical Solution of Partial Differential Equations.* Cambridge University Press, 2005.

[49] A. Popov, V. Vinogradov, N. Zhu, and F. Landstorfer, "3d parabolic equation model of em wave propagation in tunnels," *Electronics Letters*, vol. 35, no. 11, pp. 880 – 882, May 1999.

[50] A. Popov and N. Y. Zhu, "Modeling Radio Wave Propagation in Tunnels with a Vectorial Parabolic Equation," *Antennas and Propagation, IEEE Transactions on*, vol. 48, no. 9, pp. 1403–1412, Sep 2000.

[51] ——, "Modeling radio wave propagation in tunnels with a vectorial parabolic equation," *Antennas and Propagation, IEEE Transactions on*, vol. 48, no. 9, pp. 1403 –1412, Sep. 2000.

[52] M. Levy, *Parabolic Equation Methods for Electromagnetic Wave Propagation.* IEE Press, London, UK, 2000.

[53] C. Zelley and C. Constantinou, "A Three-Dimensional Parabolic Equation applied to VHF/UHF Propagation over Irregular Terrain," *Antennas and Propagation, IEEE Transactions on*, vol. 47, no. 10, pp. 1586–1596, Oct 1999.

[54] R. Martelly and R. Janaswamy, "An ADI-PE Approach for Modeling Radio Transmission Loss in Tunnels," *Antennas and Propagation, IEEE Transactions on*, vol. 57, no. 6, pp. 1759–1770, June 2009.

[55] R. Dai, Weizhong; Nassar, "Compact adi method for solving parabolic differential equations," *Numerical Methods for Partial Differential Equations*, vol. 18, no. 2, pp. 129–142, 2001.

[56] Z. F. Tian and Y. B. Ge, "A fourth-order compact adi method for solving two-dimensional unsteady convection-diffusion problems," *J. Comput. Appl. Math.*, vol. 198, no. 1, pp. 268–286, 2007.

[57] R. Martelly and R. Janaswamy, "Modeling radio transmission loss in curved, branched and rough-walled tunnels with the adi-pe method," *Antennas and Propagation, IEEE Transactions on*, vol. 58, no. 6, pp. 2037 –2045, june 2010.

[58] J. Alonso, S. Capdevila, B. Izquierdo, and J. Romeu, "Propagation Measurements and Simulations in Tunnel Environment at 5.8GHz," in *Antennas and Propagation Society International Symposium, 2008. AP-S 2008. IEEE*, 5-11 July 2008, pp. 1–4.

[59] J. Alonso, B. Izquierdo, S. Capdevila, and J. Romeu, "Preliminar Propagation and MIMO Experiments in Train Tunnels at 5.8GHz," in *Antennas and Propagation Society International Symposium, 2009. APSURSI 2009. IEEE*, 1-5 June 2009, pp. 1–4.

[60] J. Alonso, B. Izquierdo, and J. Romeu, "MIMO Channel Measurement Campaign in Subway Tunnels," in *Antennas and Propagation, 2010. EuCAP 2010. 4th European Conference on*, April 2010.

[61] W. C. Lee, *Mobile Communications Engineering*. McGraw-Hill Professional, 1982.

[62] G. Foschini and M. Gans, "On limits of wireless communications in a fading environment when using multiple antennas," *Wireless Personal Communications*, vol. 6, pp. 331–335, 1998.

[63] E. Telatar, "Capacity of multi-antenna gaussian channels," *European Transactions on Telecommunications*, vol. 10, no. 6, pp. 585–596, 1999.

[64] M. Lienard, P. Degauque, J. Baudet, and D. Degardin, "Investigation on MIMO Channels in Subway Tunnels," *Selected Areas in Communications, IEEE Journal on*, vol. 21, no. 3, pp. 332–339, 2003.

[65] J. Molina-Garcia-Pardo, M. Lienard, D. Degauque, P.and Dudley, and L. Juan-Llacer, "Interpretation of mimo channel characteristics in rectangular tunnels from modal theory," *Vehicular Technology, IEEE Transactions on*, vol. 57, no. 3, pp. 1974–1979, May 2008.

[66] J. Molina-Garcia-Pardo, M. Lienard, C. Degauque, P.and Garca-Pardo, and L. Juan-Llcer, "Mimo channel capacity with polarization diversity in arched tunnels," *Antennas and Wireless Propagation Letters, IEEE*, vol. 8, pp. 1186–1189, 2009.

[67] J. Alonso Valdesueiro, B. Izquierdo, and J. Romeu, "On 2x2 mimo observable capacity in subway tunnels at c -band: An experimental approach," *Antennas and Wireless Propagation Letters, IEEE*, vol. PP, no. 99, pp. 1 –1, 2010.

[68] M. Jensen and J. Wallace, "A review of antennas and propagation for mimo wireless communications," *Antennas and Propagation, IEEE Transactions on*, vol. 52, no. 11, pp. 2810–2824, 2004.

[69] S. Verdu, "Fify years of shannon theory," *Information Theory, IEEE Transactions on*, vol. 44, no. 6, pp. 2057–2078, 1998.

[70] F. De Flaviis, L. Jofre, J. Romeu, and A. Grau, *Multiantennas Systems for MIMO Communications*, C. A. Balanis, Ed. Morgan & Claypool, 2008.

[71] J. Alonso Valdesueiro, "Multi-element arrays in subway environments," Ph.D. dissertation, AntennaLab - Universitat Politecnica de Catalunya. Departament de Teoria del Senyal i Comunicacions, 2011.